42nd AIAA Thermophysics Conference
27 - 30 June 2011, Honolulu, Hawaii

AIAA 2011-3143

Shock Wave Impingement on Boundary Layers at Hypersonic Speeds: Computational Analysis and Uncertainty

James L. Brown, Ph.D. *
NASA Ames Research Center, Moffett Field, CA, 94035, USA

I. Abstract

The current status of uncertainty in computational fluid dynamic simulations of impinging hypersonic shock-wave/turbulent boundary-layer interactions is considered for conditions pertinent to the development of scramjet air-breathing propulsion concepts. The computational methods examined are those of NASA's DPLR Real-Gas Reynolds-Averaged Navier-Stokes finite-volume code using structured grids and MPI Linux Cluster parallel computer technology, along with several commonly used turbulence models. The available body of experiments is examined for those suitable to base such an evaluation of computational methods. Turbulence model implementation details are evaluated for applicability to these hypersonic flows. The errors and uncertainty, inherent to the RANS methods and turbulence models used, are numerically evaluated with respect to physics quantities of interest not only to computational fluid dynamic practitioners and developers, but also to the designer making use of modern CFD methods to innovate and develop hypersonic capable hardware such as prototype scramjet engines. Reported are statistical based means, variances, and confidence limits of uncertainty measures constructed for these physics quantities of interest so as to reveal the certitude with which computations of impinging shock-wave/boundary-layer interaction flows at hypersonic turbulent conditions can be used and evaluated with the intent of improvement.

II. Introduction

The development of scramjet air-breathing propulsion technology concepts for hypersonic vehicles is anticipated, e.g., Billig,[1] to rely heavily on the ability to accurately compute the flow about the fore-body and engine inlet regions of proposed vehicle designs. The unknowns and inexactness of turbulence models are the primary limiting factors. Flight vehicle tests (X-43, X51a) have flown which establish scramjet proof-of-concept, but considerable research and development in support of the scramjet concept remains. For the desired range of hypersonic flight conditions, stable compressive deceleration of the free-stream flow into the scramjet engine inlet can not be expected to occur as an isentropic process. On the other hand, a design choice making use of a single shock at the engine inlet would entail a strong shock that would lead to excessive total pressure loss with attendant engine inefficiency. So, in place of the conventional jet engine compressor stage related to current transonic and supersonic flow conditions, the first or compression phase of the hypersonic scramjet engine is accomplished non-isentropically on the external fore-body leading to the engine inlet and internal to the engine inlet by a series of oblique shocks generated, by design, with compression corner and impinging shock-wave/boundary layer interactions. By use of a series of such oblique shock-wave/turbulent-boundary-layer interactions (SWTBLI), with each interaction of strength just short of boundary-layer separation, pressure recovery of the compression phase can be accomplished more efficiently in a compact design, while minimizing the accumulative total pressure loss of the incoming air feeding the engine. Off-design operation will inevitably lead to the occurrence of fully separated SWTBLI. Innovation, optimization and off-design analysis of specific engine and engine inlet designs, thus will depend on accu-

*Research Scientist, Aerothermodynamics Branch, MS 230-2, AIAA Member.

rate prediction of compression-corner and impinging shock-wave/boundary-layer interactions at hypersonic turbulent conditions.

A solid foundation for improvements in prediction capability of shock-wave/boundary-layer interactions is best based on first understanding of the source and level of uncertainties and of residual errors in our current capability to compute existing SWTBLI experiments vetted for accuracy and relevance to the scramjet air-breathing mission. As a consequence, NASA's Fundamental Aeronautics Program has tasked its Hypersonics Uncertainty working group[2] to address hypersonic 2D and axisymmetric compression corner[3] and impinging shock cases to that end. As part of that effort, the purpose of the present paper, then, is to compute selected hypersonic impinging SWTBLI experiments with DPLR (e.g., Wright[4]) one of NASA's production real-gas Navier-Stokes codes, and with well-known turbulence models, in particular the SST,[6] $K-\omega$,[10] and Spalart-Allmaras[11] turbulence models. For the Spalart-Allmaras model, the compressibility modifications of Catris and Aupoix[12] are incorporated, whereas for the SST and $K-\omega$ models, the free-shear-layer compressibility corrections of Sarkar, of Zeeman and of Wilcox (all three are described in Wilcox[10]) as modified by Brown[13] are evaluated for use with hypersonic boundary layers. We then evaluate the uncertainties and sources of error in these computations relative to these selected experiments, reporting the current best practices and uncertainty levels in accomplishing these computations. Such information should prove useful to the scramjet engine designer, and also in pursuing future improvements in our predictive capability, and in providing guidance in design of future experiments.

III. Discussion

In this section, we first discuss the topology of impinging hypersonic shock-wave/turbulent boundary-layer interactions so as to identify the physics features of interest. We then identify correlations which will prove useful in analyzing uncertainty in both the experiments and computational simulations. The nomenclature of uncertainty will be described and measures of uncertainty to be used for this study will be given. Next described will be the computational approach including the RANS code used and the turbulence models and variations thereof. In the final subsection of the Discussion section, we describe the process by which the experiments to be simulated were selected and give an overview of those selected experiments.

III.A. Impinging Shock-Wave/Boundary-Layer Topology

The flow topology associated with a generic impinging SWTBLI experiment is depicted in Figure 1. Flow is "*NASA-standard*" in being from left to right in the figure. A zero-pressure gradient boundary layer develops on the flat test surface, either a 2D flat plate or an axisymmetric cylinder, at the bottom of the figure. Depending on the experimental setup, a leading edge shock (typically an oblique weak shock or Mach wave) may either pass above the shock generator, or impact on the shock generator. A shock generator, either a flat 2D plate surface inclined at angle α or an axisymmetric cowl with an included half-angle, α, generates the impinging shock at angle Θ from its leading edge. The shock angle Θ may be found by means of inviscid relations[14] depending on the turning angle α, the rate of growth of the boundary layer on the generator, the Mach number and gas properties. The impinging shock, of angle Θ, will reduce the Mach number from M_1 to M_2, with total pressure loss from Pt_1 to Pt_2. The impinging shock will intersect the incoming flat plate boundary layer at a location roughly (Zg-δ)/Tan Θ, where Zg is the height of the shock generator leading edge above the flat plate, δ is the boundary layer thickness at the impingement location, and Θ is the angle of the generated impinging shock. A reflected shock will occur emanating from within the boundary layer in the vicinity of the impingement. The shock generator will be of finite length, L_g. At the tail end of the shock generator, an expansion fan occurs which moderates the reflected shock downstream of the impingement point. The overall increase in wall pressure in the vicinity of the impingement location will be the consequence of a two-oblique-shock inviscid problem accounting for both the impinging and reflected shocks. Because of the subsonic flow at the inner portion of the boundary layer, a portion of this shock-generated pressure increase will be seen upstream of the impingement point. When the shock is of sufficient strength, a separation bubble will form upstream of the impingement with a lambda shock forming due to the upstream influence of the overall pressure rise. As streamlines just above the separation bubble will turn back towards the flat plate to close the separation bubble at the reattachment position, an expansion wave above the separation bubble will also form. Should separation occur, the lambda shock angle will be dictated by the property of the oncoming turbulent boundary layer's ability to resist separation due to a

given pressure rise. As a consequence, the wall pressure behavior in the vicinity of a shock-separated bubble is more a property of the boundary layer than the nature of the particular shock causing the separation, leading to the free interaction concept introduced by Chapman,[15] and expanded on by Erdos and Pallone,[17] and others.

What is not obvious from this description of shock separation flow topology is that the λ-shock that forms upon separation is highly unsteady, having time scales comparable to that of the boundary layer itself. Experimental studies on a fully separated Mach 3 cylinder flare,[18] making use of high-speed Schlieren film correlated with a row of high-speed Kulite pressure cells, and also 2D-Laser Doppler Velocimeter measurements ensemble-averaged using the same set of Kulite pressure cells, demonstrated that the λ-shock oscillates rapidly, more or less at a fixed angle, but rapidly and randomly sweeping back and forth in X throughout the region of mean separation. The position of the leading edge of the λ-shock as seen in the high-speed Schlieren film correlates with the wall pressure fluctuations, and the 2D-LDV when ensemble averaged with the fluctuating wall-pressure measurements proved to be bi-modal in state. As a consequence, it is possible to establish[19] that the bi-modal property of the separation bubble can lead to artificially high Reynolds stress tensor values as the 2D-LDV measurements indicated that the differences between the different means, (e.g., $(\hat{u}_2 - \hat{u}_1) \cdot (\hat{v}_2 - \hat{v}_1)$) of the multiple states of the λ-shock contributes to the measured turbulent Reynolds stress, $< u'v' >$. This is an effect of enhanced apparent Reynolds stresses that will not be normally included in RANS turbulence modeling. Further, the shape of the wall pressure distribution in the region of the separation bubble will likely be the consequence of a constant pressure inviscid region contained within the λ-shock region, but also subject to the bi-modal probability density function of the shock leading edge position. Shock unsteadiness is not examined in this paper, but should be recognized as an implicit source of uncertainty present in the computational approach of Reynolds-Averaged Navier-Stokes with conventional turbulence models currently available.

III.B. Turbulent Correlations and Oblique Shock Relations

III.B.1. Oblique Shock Relations

Oblique shock impingement involves two oblique shocks, the 1st being the impingement shock to turn the flow to agree with the shock generator, the 2nd being the reflexion shock to turn the flow back aligned with the test surface. For a flat surface initially aligned with the free stream, two turnings of the shock generator angle δ occur, but with each there is a decrease in Mach number, increase in pressure, density, and temperature, loss of total Pressure, and associated increase in entropy. Simple perfect gas inviscid relations, if suitable, can be used as a check on both experimental and computational results. These relations are available in many textbooks but also from the familiar NACA 1135 report now available online. One problem encountered with these relations is that the formulations are given as a function of the shock angle, θ, e.g., $\delta(M_1, \theta)$, $P_2/P_1 = f(M_1, \theta)$, etc., for which it would seem to require iteration since what is known here is the turning angle, δ. However, the lesser-known direct algorithm for $\theta = f(M_1, \delta)$ was given by Thompson,[20] also see Mascitti[21] and Wolf.[22] This direct algorithm is used for the inviscid problem for evaluating total pressure errors as described in a later section as well as for comparison of the peak pressure levels for the Schulein experiment , also described in a later section.

III.B.2. Turbulent Skin Friction Correlations

Transition to turbulence is best determined from the actual experiment, or, if not otherwise known, from correlation, based typically on Re_θ from *laminar* simulations. Transition can contribute as a source of uncertainty to both simulation and experiment, particularly for hypersonics, e.g., Reda.[23] As the location of transition is known, or can be deduced, in the hypersonic experimental cases considered here, the experimental transition location will be used for the simulations.

The most widely accepted, e.g. Hopkins and Inouye,[24] skin friction relation for a turbulent compressible flat plate boundary layer is found by means of the incompressible adiabatic wall Kármán-Schoenherr correlation,[25] given as a function of $Re\theta$, but with the VanDriest-II compressibility transformation[26,27] applied so as to account for both compressibility and heat transfer.

$$1/(C_f F_c) = 17.08 \log_{10}^2(Re_\theta F_\theta) + 25.11 \log_{10}(Re_\theta F_\theta) + 6.012 \tag{1}$$

A second form for accepted flat plate skin friction relations is the Van Driest-II transformed correlation of White:[28]

$$(C_f F_c) = 0.455/\ln^2(0.06 Re_x F_x) \tag{2}$$

Note that C_f is the *local* skin friction at the compressible conditions, Re_θ makes use of the local density-wieghted form of momentum thickness, θ, and Re_x makes use of the local edge condition and the local distance from the leading edge of the flat plate.

The Van Driest II compressibility transformation process F_c, F_x, and F_θ terms appearing in the above correlations:

$$\begin{aligned} F_c &= [(T_{aw}/T_e) - 1]/(\arcsin\alpha + \arcsin\beta)^2, && (3)\\ F_\theta &= \mu_e/\mu_w,\ F_x = F_\theta/F_c, && (4)\\ \alpha &= (T_{aw} + T_w - 2T_e)/(\Gamma T_e) && (5)\\ \beta &= (T_{aw} - T_w)/(\Gamma T_e), \quad \text{and} && (6)\\ (\Gamma T_e) &= [(T_{aw} + T_w)^2 - 4(T_e T_w)]^{1/2} && (7) \end{aligned}$$

T_{aw} is obtained using a turbulent recovery factor of 0.89.

The VanDriest II transformation process is required to transform the skin-friction results from what are *incompressible* correlations to *compressible* cases. Where the flow is nearly incompressible, and adiabatic, the VanDriest II transformation goes indeterminant (0/0), but, of course, is not then needed.

Hopkins and Inouye concluded, in comparing various correlation treatments with extensive data sets, that the VanDriest II transformation process yields the best performance for compressible skin friction correlation with or without heat transfer for zero-pressure gradient boundary layers relative to competing theories of the time, to within $\approx 10\%$ for $T_w/T_{aw} > 0.3$. However, for cold-wall compressible boundary layers with $T_w/T_{aw} < 0.3$ the VanDriest II formulation tended to overpredict skin friction by as much as 20%, whereas the formulation of Spalding and Chi gave better agreement with existing data, also see Goyne, et al.[29] If heat transfer is desired, then a Reynolds analogy factor near unity (Coakley[31] recommends $\approx 1.17 \pm 15\%$) is used, where $Ra_F \equiv 2C_h/C_f$.

Naturally, for air (or nitrogen or helium) at low temperature, which can be most relevant to hypersonic wind tunnel results, the viscosity formulation of Keyes should be used in evaluating F_c rather than the viscosity relation of Sutherland, as hypersonic wind tunnel freestream conditions can approach liquification.

III.B.3. Free-Interaction Theory and Related Correlations

Whether empirically observed trends, as embodied in free-interaction theory based correlations, are correctly incorporated into current CFD methodology is, or should be a concern. As a consequence, this section reviews free-interaction theory and the trend behaviour of separated shock-wave turbulence boundary layer interactions that is reflected in the empirical correlations related to that theory. Simple comparison of CFD simulations with the few sparse hypersonic turbulent experiments in existence is unlikely to reveal whether existing turbulence modeling provides the proper trend response to changes in Reynolds number, shock strength, cold-wall heating, and other effects that a system optimization process will require be examined.

Chapman, Kuehn, and Larson,[15] introduced the concept of *free-interaction theory* , when they observed that certain characteristics of shock separated flows, within the separation bubble region were independent of the strength, or even of the particular geometric mode of the primary shock inducing separation, regardless of whether the shock/boundary layer interaction type was that of a compression corner, impinging shock or forward facing step. For SWBLI flows, once separation is induced, a λ-shock forms ahead of the primary shock system. This λ-shock is associated with the separation bubble that forms upstream of the primary shock system, and it is the edge Mach number and the oblique shock angle of the λ-shock that generates the pressure rise that proves just able to separate the upstream boundary layer. Once the separation process is initiated, the upstream boundary layer is unable to support substantial further pressure rise and the size of the separation bubble under the λ-shock system will grow to adjust itself, until the displacement surface of the separation bubble will generate that pressure rise that will just be sustained for the extent of the entire separation bubble. For a given initial boundary layer, it is the separation bubble size and extent that proves most sensitive to increasing primary shock strength rather than the λ-shock angle or the pressure within the

separation bubble. Chapman found that the pressure rise which the boundary layer can resist will scale with the upstream boundary layer skin friction coefficient, Mach number, and whether the upstream boundary layer is laminar or turbulent. For shock wave induced separation of a turbulent boundary layer, Chapman found from considerable data of different SWBLI types and in the range of M_0 between 1.0 and 4.2, that, to within about 10%:

$$(P_s - P_0)/P_0 = f(M_0)\sqrt{C_f} \tag{8}$$

Note that this gives only the separation bubble plateau pressure, P_s and not the wall pressure variation with X, and the value for $f(M_0)$ will depend on whether the initial boundary layer is laminar or turbulent. Chapman gives this relation in terms of a plotted figure of normalized separation bubble pressure vs Mach number of the interaction.

Erdos and Pallone[17] further extended the free interaction theory, providing a semi-empirical solution based on integral boundary layer methods then current, in conjunction with linearized inviscid theory and laminar and turbulent boundary layer shape function correlations adjusted so as to analyze through the region of shock separation. They made use of the experimental SWBLI data of the time, with emphasis on the cylinder-flare data taken by Kuehn. The result of their theory was a means of estimating the spatial extent of separation, ℓ_{sep}, and a normalized form of the pressure spatial variation, $P_w(x)$, through the free-interaction region, according to:

$$(\ell_{sep}/\delta_0) = K(P_f - P_s)/P_0 \tag{9}$$

$$(P_w - P_0)/q_0 = Re^{-1/2n}\zeta^{1/2} f_3((x - x_0)/\ell_{sep}) g(M_0, T_{w,0}/T_{e,0}) \tag{10}$$

$$g(M_0, T_{w,0}/T_{e,0}) = \sqrt{2C_{f,0}Re^{1/n}/(M_0^2 - 1)} \tag{11}$$

Where, P_w is the wall pressure through the free interaction region, P_0 and $C_{f,0}$ are the wall pressure and skin friction of the boundary layer just upstream of separation, q_0 and M_0 are the dynamic pressure and Mach number of the freestream just upstream of separation, Re is the Reynolds number based on distance from the leading edge, x_0, $\zeta = C_{p,exact}/C_{p,linear}$ is a correction for the linearized inviscid theory. For turbulent flows, the exponent n equals 5, and the constant $K = 4.15$. For laminar flows, the exponent n equals 2, and the constant $K = 105$ reflecting the greater growth sensitivity coefficient to overall primary shock pressure rise of a laminar vs turbulent separated boundary layer.

The g function is designed to adjust their nominally adiabatic wall theory to account for Mach number and wall cooling effects. The function f_3 is a "universal-normalized" pressure distribution describing the pressure variation with distance through the free interaction and separation bubble and is usually given graphically. For a separating turbulent boundary layer, where the normalized pressure function takes on the accepted value of $f_3 = 4.22$ separation is indicated, then the f_3 function continues to rise with x till it reaches $f_3 = 6$ for the separation "plateau" pressure throughout most of free interaction region.

The growth of the separation bubble, as given by the separation length, ℓ, is seen to be linear with increase of P_f or "final" pressure of the primary shock system over P_s which is the separation bubble plateau pressure, as might be intuitively expected.

Erdos and Pallone conducted comparisons of their developed semi-empirical theory with both supersonic and hypersonic data up to Mach 12 to good effect. It is useful to understand that the integral boundary layer/linearized inviscid theory they used, though neither rigorous nor 'modern', provides a sufficiently solid physics basis for the *form* of their semi-empirical correlation. Erdos and Pallone describes limitations in development of their analysis that might limit applicability of their resulting correlation.

Erdos and Pallone do not provide a means of estimating the heat transfer behaviour through the free interaction region, but other physics based discussions indicate that with onset of shock-separation, for the separation bubble region, the wall heating tends to initially decrease below upstream boundary layer values, even though the pressure rises, but then rises as reattachment is approached, and then follows the pressure-wall-heating correlation described below. However, no trend of wall heating variation in the separation region is clearly established in the various datasets to date, and so no free interaction theory for wall heating seems to have gained favor.

Delery and Marvin[32] in their discussion of free-interaction theory correlations, also point out the interesting analysis of Reshotko and Tucker.[33] Reshotko and Tucker present physics-based arguments recognizing that the form of their shock-separation theory can be supplemented with the boundary layer shape factor

at separation and reattachment, being that for an inflexional profile. They concluded that for incipient separation the ratio of M_2/M_1 would be about 0.702 (Delery and Marvin give a slightly higher value of 0.762), seemingly regardless of interaction Mach number. We point out here, that using the M_2/M_1 value in the oblique shock relations of NACA 1135, will give an asymptotic value (as function of M_1) of $P_2/P_1 \approx 3+\sqrt{11}$, close to the value of separation bubble value of 6 appearing in free interaction theory.

Whether based on free-interaction theory or simply on empirical observation, certain trends can be determined. Generally speaking as the Mach number increases, the turbulent boundary layer becomes more resistant to separation and it takes a larger induced pressure rise to initiate separation; and, as the Reynolds number increases (C_f decreases) then the turbulent boundary layer becomes less resistant to separation, leading to a lower induced pressure rise to initiate separation. Kuehn[16] based on extensive experimental data in the range of Mach 1.5-5, albeit mostly of axisymmetric flare, further states that the effect of heat transfer to the wall consistently reduces slightly the extent of separation; for axisymmetric cases a thin boundary layer relative to the cylinder diameter tends to promote separation; and, as might be expected, velocity profiles that were not fully developed as to turbulence were more prone to separation than fully developed boundary layers. The effect of bluntness of the flat plate or nose (entropy layer effect) on separation tended to be accounted for by using local properties, e.g. δ_0^* or C_f and M_e of the boundary layer just upstream of the interaction.

Whether such empirically observed trends are indeed correctly incorporated into current CFD methodology is, or should be a concern and is worthy of future analysis. There does seem to be a need for a comprehensive comparison of these and other semi-empirical correlations with a modern updated list of hypersonic experiments.

The physics based correlations stemming from free-interaction theory, as described in this subsection, provide a basis for behaviour trends that will not be revealed by comparisons of CFD simulations with the few hypersonics experiment that exist. Also, as the free-interaction work was mainly accomplished based on supersonic experiments, there does seem to be a need for a comprehensive comparison of these and other semi-empirical correlations with a modern updated list of hypersonic experiments. What may be reasonably inferred from the CFD RANS hypersonic shock-separated flow simulation results that follow in the present study is that *the understanding reflected in the extensive experimental correlations related to free interaction theory has not been infused into standard available turbulence models.* It is this deficiency in existing turbulence models that may be a core reason for the high level of statistical variance and uncertainty that is exhibited by CFD simulations of hypersonic SWTBLI flows.

III.B.4. SWTBLI Pressure-Heating Correlations

An interesting and useful correlation of heating variation with pressure for SWTBL interactions was found by Back and Cuffel,[34] and demonstrated by others, e.g. Holden,[35] mainly that throughout the attached region of a SWTBLI interaction-but not within a separation bubble if it exists- the pressure and heating scale together approximately as:

$$Q_{P85} \equiv Q_0 \cdot (P/P_0)^{0.85}, \quad \text{for turbulent 2D SWTBLI} \tag{12}$$

As with the upstream free-interaction relations, the pressure-heating correlation appears to correlate a great deal of experimental data regardless of whether the interaction itself is of the compression corner or impinging shock type. With the difficulty that current RANS methods have in predicting wall heating in the vicinity of reattachment of shock-separated flows, it may be more accurate to make use of the pressure rise past reattachment from the CFD simulations and then use this $Q \approx P^{0.85}$ correlation to provide attached SWTBLI heating predictions. The 'QP85' correlation is not accurate within the separation bubble itself.

Coleman and Stollery[36] derive a different relation between heat transfer and pressure through a SWTBLI, however, they do point out that their relation agrees well with the 0.85 power correlation of Back and Cuffel in the limit of large pressure ratio, hence we will predominantly use the correlation of Back and Cuffel.

III.C. Uncertainty

III.C.1. Uncertainty Nomenclature and Definitions

As the purpose of the current paper is to determine the capabilities of present-day RANS-based computational analysis of hypersonic shock-wave/turbulent boundary-layer interactions in terms of *Uncertainty* and *Error*,

a brief review of the precise meaning of these and related terms seems called for to ensure that the present work is consistent with accepted AIAA guidelines and published definitions,[37] see Coleman, et al.,[38] Roache[39] and Oberkampf, et al.,[40–42] for a more comprehensive discussion. We first extract the following definitions from the AIAA Guide:[37]

> *Verification:* The process of determining that a model implementation **accurately represents** the developer's **conceptual description of the model** and the solution to the model.
>
> *Validation:* The process of determining the degree to which a model is an **accurate representation of the real world** from the perspective of the intended uses of the model.
>
> *Uncertainty:* A potential deficiency in any phase or activity of the modeling process that **is due** to **lack of knowledge**.
>
> *Error:* A recognizable deficiency in any phase or activity of the modeling process that **is not due** to a **lack of knowledge**.

It should be recognized that the current paper, in no way, intends to conduct a thorough verification and validation process, as that is beyond the scope of our present charter. Rather, we are making use of a NASA production code, *as is*-or slightly modified so as to better examine errors and uncertainties, and proceeding to identify and quantify those errors and uncertainties present in the existing CFD analysis process specific to hypersonic impinging SWTBL interactions.

Computational simulation results and experimental measurements, and any so derived variables, will likely be inexact and exhibit statistical behaviour as a consequence of deficiencies in the accuracy of modeling or measuring. *Uncertainty* and *Error* are broad categories normally associated with this loss of accuracy in modeling and simulation. Although similar in that both lead to loss of accuracy, they are not the same, largely in that errors are knowable and correctable (often being mathematically deficient in origin), whereas uncertainty is due to a genuine lack of knowledge (being deficient in origin as to the conceptual construction of the modeling of the physics).

Errors include inappropriate selection of models for the particular case, including but not limited to selection of a turbulence model known to be incapable of handling separation, incorrect compressible corrections to turbulence model, too low numerical order, flux selection, inadequate grid resolution, etc.

Uncertainties include the unknown and inexactness of the current turbulence models as applied to hypersonic SWTBLI, incomplete specification or reporting by the experimentor of geometry or flow conditions, unknown location of transition, etc. Errors tend to be correctable, but perhaps tolerated for reasons of practicality. To avoid error in application of a turbulence model, we include proper choice in the details of turbulence modeling implementation options such as selection of proper mathematical expression of the turbulent production, compressibility corrections, wall boundary conditions, and adherence to established correlations applicable to the boundary layer and shock wave interaction. As a consequence, in later sections, we examine the sensitivity of several of our turbulent solutions to these turbulence model implementation choices. An example of acceptable error, is the use of a coarse grid for preliminary simulations.

To apply these concepts to a particular problem area, we need to be able to numerically evaluate measures of uncertainty and error in terms of readily understood statistical measures, such as bias, variance, and confidence intervals, which have clear definition and pragmatic meaning.

III.C.2. Uncertainty Measures

It is natural part of the verification and validation process of computational fluid dynamic methods then to compare CFD simulation results with directly related experimental measurements. However, neither of these parameters, regardless of the source, will, in general, represent the "true value" that in any absolute sense determines the precise accuracy of either the CFD simulation or of the experiment. The results of both the CFD simulation and the experimental measurement will themselves involve imprecision and thereby contain bias and variance. As a consequence, in forming the "Difference" or, as the case considered here, the "Discrepancy" parameter, where $\mathcal{D} \equiv \sum(\chi_{CFD} - \chi_{Expt})/n$, what is actually formed is a new statistical variable which is the difference of two statistical variables, where what is desired is to "compare two quantities or populations" to examine if one variable is an unbiased estimator of the second variable, a well-known statistical problem.[43] This new variable will have, in general, a non-zero mean or bias as well as a variance that will depend on the statistical properties of the original variables. For such a "Discrepancy" parameter, other statistical quantities such as the 95% confidence interval may be found by established standard statistical

procedures,[44,45] assuming sufficient sample size is available. The variance and confidence interval of the "Discrepancy" variable will, of course include the effects of bias and variance due to uncertainty and error in both the computation and experimental formulation. However, at a minimum, the "Discrepancy" variable will have as a lower bound for its variance and confidence interval magnitude, the variance and confidence interval magnitude of the experimental measurements. Thus, to evaluate CFD results by comparison with an experiment, it is important to both choose the best available experiments and to know or estimate the magnitude of the experimental measurement bias and variance.

A practitioner of the CFD arts is likely to ask, "How accurate are my simulations?" Whereas a designer making use of CFD results might well ask, "What margins do I apply to the CFD results that I need to apply in my design?" These are not abstract questions, but address pragmatic concerns regarding particular physical effects, such as heating or pressure levels or extent of separation. To help answer these questions for hypersonic shock-wave/turbulent boundary-layer applications, we construct Uncertainty Measures, based on statistical analysis concepts and intended to account for the primary features of shock-wave/boundary-layer interactions likely to be of interest to both the CFD practitioner and the CFD-user/designer. To do this we accumulate, for several physics parameters of likely interest, a numerical evaluation of the "Discrepancy" between experiment and the CFD simulation of that experiment. Then, for a collection of similar experiments of the same class (e.g., attached hypersonic impinging SWTBLI, or fully separated hypersonic impinging SWTBLI), and for the similar physical effect (such as extent of separation, or peak pressure), we combine the numerical evaluations for each physical effect and each experiment to arrive at measures of Uncertainty in terms of confidence interval of the accumulated Discrepancy parameter.

In the present work, we make use of several vetted experiments of the same general type or statistical class, each of which first develop a nominal 2D or axisymmetric upstream hypersonic turbulent boundary layer with known properties, and then subjects that boundary layer to a 2D or axisymmetric impinging shock. The design of these experiments is such that the strength of the impinging shock may or may not be sufficient so as to cause the boundary layer to separate, then reattach. The relevant physics of such hypersonic shock-wave/turbulent boundary-layer interactions include effects of interest to both the CFD practitioner and the designer making use of CFD arts, that include:

1. How well does the computation estimate either the wall shear stress or wall heat transfer of the boundary layer just upstream of the interaction.
2. If separated, the extent of separation region, L_s, relative to the boundary layer thickness, δ_0, just upstream of the interaction;
3. If separated, the wall pressure in the separation bubble plateau region, P_b relative to the mean pressure of the upstream boundary layer;
4. If separated, the wall heat transfer in the separation bubble plateau region, Q_b relative to wall heat transfer of the upstream boundary layer;
5. The peak wall pressure in the post impingement region (post re-attachment if separated),P_p, relative to the mean pressure of the upstream boundary layer, P_0;
6. The peak wall heat transfer in the post impingement region (post re-attachment if separated), Q_p, relative to the wall heat transfer for the upstream boundary layer, Q_0.

Corresponding to each of the shock-wave/boundary-layer physics effects listed above, and numerically evaluated for each selected experiment, we can then define, for each simulation relative to the particular experiment, and for each physical effect (p), the Δ_p parameter:

$$\Delta_{Q_0} \equiv (Q_{0,CFD} - Q_{0,Expt})/Q_{0,Expt}, \quad \text{Upstream Boundary Layer Uncertainty} \tag{13}$$

$$\Delta_{L_s} \equiv (L_{s,CFD} - L_{s,Expt})/L_{s,Expt}, \quad \text{separation extent} \tag{14}$$

$$\Delta_{P_b} \equiv (P_{b,CFD} - P_{b,Expt})/P_{b,Expt}, \quad \text{separation bubble pressure} \tag{15}$$

$$\Delta_{Q_b} \equiv (Q_{b,CFD} - Q_{b,Expt})/Q_{b,Expt}, \quad \text{separation bubble heat transfer} \tag{16}$$

$$\Delta_{P_p} \equiv (P_p/P_0)_{CFD} - (P_p/P_0)_{Expt})/(P_p/P_0)_{Expt} \tag{17}$$

$$\Delta_{Q_p} \equiv (Q_p/Q_0)_{CFD} - (Q_p/Q_0)_{Expt})/(Q_p/Q_0)_{Expt} \tag{18}$$

Those terms which involve separation need only be included if either the simulation or the experiment indicates separation.

Each of these Δ parameters corresponds to a single physical effect and will be evaluated for each turbulence model simulation for each experimental case and accumulated in a Table specific to each case examined.

We then combine these, for each physical effect, and for each class of SWTBLI , using standard textbook statistical procedures to form a single-physics-effect, multi-experiment 'Discrepancy' Measure having a sample mean and variance.

$$\hat{\mathcal{D}}_p \equiv (\sum_{1,n_{Expt}} \Delta_{p,i})/n_{Expt} \tag{19}$$

$$\mathcal{D}'^2_p \equiv (\sum_{1,n_{Expt}} \Delta^2_{p,i})/(n_{Expt}-1) \tag{20}$$

The sum is over all experiments that include the physics effect listed above. Such a measure (mean, variance) can be evaluated for each of the listed physics effects, $\mathcal{D}_{Q0}, \mathcal{D}_{LSep}, ..., \mathcal{D}_{Qp}$. Confidence limits, which include both bias and variance effect, can then be established for each of the above measures by conventional statistical approaches.[43–45]

The measure described in this section may well contain both error contributions and uncertainty contributions, as such effects are difficult to separate, but as it is anticipated that residual error will be low compared to modeling uncertainties it is realistic to interpret the 'Discrepency' measure as defined as primarily sample Uncertainty Measures for CFD modeling of these SWTBLI. With Uncertainty Measures as constructed in this section for each of the SWTBLI related physical effects of interest, it should enable the CFD-based designer to evaluate "how accurate" the computational simulation is likely to be or to help the CFD practitioner to better focus on those aspects of the simulation of flow physics that need most improvement as based on sound statistical procedures.

III.D. Computational Methods and Physics Models

III.D.1. DPLR RANS

The DPLR (Data-Parallel Line Relaxation) code, one of several NASA hypersonic aerothermodynamics production codes, (other NASA codes include Laura and Vulcan), provides the basis for the computations in the present paper. It is a three-dimensional (3D) implicit finite-volume, structured-block real-gas Navier-Stokes code that incorporates non-equilibrium finite-rate atmospheric gas chemistry, modified Steger-Warming flux-split with upwind Jacobians and higher-order spatial differencing. An extensive set of gas chemistry options are available, including options for single- and multiple-temperatures, various gas-diffusion modeling for mixtures of reacting gases, but also that of perfect gases of various composition. Several turbulence models with compressibility modification appropriate to hypersonic flows are available as options, including the Baldwin-Lomax, the SST, the Wilcox K-Omega and the Spalart-Allmaras turbulence models. The location of transition to turbulence can be specified. A parallel-processor MPI, line-relaxation algorithm is used consistent with efficient computations on large Linux clusters. DPLR has found extensive use in NASA's Shuttle operations support, and CEV and MSL Mission and Program work. Emphasis in development of DPLR has been on atmospheric entry at hypersonic speeds from space. Wall Boundary condition options, thus, include radiative equilibrium viscous wall, including the effect of catalytic walls, as well as the more conventional adiabatic and constant temperature viscous wall boundary condition. More detail can be found in the DPLR users manual.[46]

III.D.2. Turbulence Models

The turbulence models selected for use in this study are all of eddy-viscosity type and in common use but with adaptations for hypersonic heating flow applications. They include the Baldwin-Lomax algebraic model, the Spalart-Allmaras one-equation model, and both the Menter SST/$K-\omega$ and the Wilcox-2006 $K-\omega$ two-equation models. The Baldwin-Lomax model is widely used, and published with little need to repeat here, with but one adaptation made for hypersonic flows, that of using the compressible formulation, $y^+ \equiv \rho u_{\tau_w} d/\mu_w$, in the Van-Driest damping term, where ρ is the *local* density, d is the wall-normal distance to the closest wall, and all other terms are for the nearest wall location. A common experience in hypersonic heating applications is that the Baldwin-Lomax is perhaps the best formulation to use where "acreage heating" is the primary concern, and the flow remains attached. With proper specification of transition,

turbulent Prandtl($Pr_t \approx 0.9$) and turbulent Schmidt numbers(as needed for gaseous mixtures, $Sc_t \approx 0.7$), and for smooth wall conditions, RANS simulations using the Baldwin-Lomax model are often found to be within 10% of measurements. However, for those instances where a strong shock interaction with the turbulent boundary layer occurs and/or the boundary layer may be likely to separate, the other PDE-based models gain greater acceptance and are of primary interest for this study.

The mathematical modeling of turbulence physics is often viewed as one of the largest, if not the largest, source of uncertainty in Reynold-Averaged Navier-Stokes codes. The eddy-viscosity models employed in this study all have a long track record in scientific community and industrial applications. However, these models typically are developed past their original sources to account for the experiences peculiar to any particular application area, in particular that of hypersonics applications. To avoid ambiguity, and even though each of these models are given in other publications, we specify the equations and details of the standard forms of the Spalart-Allmaras, SST and $K-\omega$ turbulence models are given in Appendix A. However, in the subsection that follows we describe implementation of these models into the DPLR RANS code used, along with the variations that we intend to explore.

III.D.3. Turbulence Model Implementation, Corrections and Variations

The standard partial differential equation turbulence models (SST, $K-\omega$, and Spalart-Allmaras), are all implemented on the same subroutine templates of the original implementation for the SST model in DPLR v 3.04. The PDE model implementation makes use of a point-Jacobi algorithm, but with sub-iterations requiring jacobians of the form $\partial F_{i+1/2}/\partial U_{i\pm1}$, etc., and with accelerated time advancement depending on the model. The spatial differencing for the turbulence PDE implementation is 2nd-order as evaluated within the cell by the volume Integral method of Gauss-Ostrogradsky (or Divergence Theorem), except for the convective terms which are evaluated at the cell boundary by 1st order. The interpolation required in this process accounts for unevenly spaced grids. Note that Spalart originally recommended 1st order treatment of the convective terms for the Spalart-Allmaras model. Also, note that in applying the Gauss-Ostrogradsky formulation, that the cell volume used should be also so derived. The numerical procedures used has proven to be uniformly robust for even the strongest shocks or with flows that approach near-vacuum, and the turbulent solutions often converge faster than the related laminar solutions.

The turbulence models considered are all fairly standard eddy-viscosity models, but some adaptations for hypersonic applications have proven necessary. We avoid the formal wall-function approach partly since confidence in such approaches may be limited due to the correlations used stem from incompressible relations, and due to the rather large near-wall spacing which can be used naturally for hypersonic flight conditions. Various implementation options do occur, including that of spatial accuracy, time-advancement, flux treatments, turbulence production term variations, 'free-viscous-shear' compressibility correction choices, numerous wall-layer and wall boundary condition treatments and the modifications of Catris and Aupoix to account for log-law region compressibility. Typically, in implementing a model, only a small sub-set of possible options are included for use in any particular code, and then a particular 'standard' approach is chosen from this option set for most applications. Included in this option set may very well be choices which are outright turbulence model 'errors' which could be prevented, and from the various options actually incorporated in a variety of RANS codes, variation in turbulence model results for simulations of the same case on the same grid can result, contributing to loss of confidence in the turbulence model .

In Appendix B, we describe the wide range of SST model implementation options in greater detail, and then conduct a sensitivity study as applied to an idealized Mach 10, Cold-Wall Flat Plate, emphasizing wall heating results. We summarize these results here for use in the main body of the paper, but reference should be made to Appendix B for details.

From the study of Appendix B, it is concluded that the vast majority of SST model implementation choices examined, properly accomplished, are neutral in their effect on the flat plate wall heating results relative to the DPLR-'standard' form employed for the primary simulations for this current paper. The primary conclusions of Appendix B study are somewhat negative in regard to the 'standard' wall boundary condition choices for SST (and similar $K-\omega$) model as they mostly lead to considerable grid sensitivity of wall heating results for grid initial spacing of $y_1^+ > 0.3$. Likewise, the inclusion of free-shear compressibility corrections -in their standard form- in the SST (and related $K-\omega$) model have a negative effect on wall heating results, with significant erroneous reduction in wall heating at Mach 10. In contrast, the form of the turbulent production term, whether of 'vorticity'-based, or 'strain'-based have little effect, for the Mach 10 flat plate examined. Further, the viscous diffusion modification of Catris and Aupoix suggested as needed

to enhance log-law compressible boundary layer behaviour are seen as not needed.

One (of two) important positive discoveries, however, is that one of the wall boundary condition treatment options considered (e.g., that of WallBC1.6 of Appendix B) appears to virtually eliminate the y_1^+ grid sensitivity on wall heating otherwise experienced. We shall see in a later section applying that same option to a fully separated impinging SWTBLI, that further benefits arise from use of this simple-to-incorporate wall boundary condition treatment.

A second important positive discovery regarding SST (and $K-\omega$) implementation choices is that a simple modification to the free-shear compressibility corrections eliminates entirely their negative impact on hypersonic wall boundary layer heating and thereby facilitates their more general use. These details of these modifications are given in Appendix B, but will be applied to the the shock separated cases of the main body of this paper, where they will be found to have some limited potential in improving the extent of separation for the hypersonic impinging SWTBLI cases considered relative to the 'standard' case of not using free-shear compressibility corrections for wall bounded flows. These easily modified free-shear layer compressibility corrections found worthwhile to examine further are the modified-Sarkar, modified-Zeeman, and modified-Wilcox forms (identified as CompC.4, CompC.5, and CompC.6 respectively).

The default form of DPLR version 4.02.1, will provide solutions, however, for the remainder of the main body of this current paper unless otherwise mentioned.

III.E. Experimental Case Selection Process

An early task in the course of this study was to identify the primary experiments of impinging hypersonic shock-wave/turbulent boundary layer type which would be simulated as the basis for the computational uncertainty analysis. To entertain evaluation of statistical quantities, we desired a minimum of three such experiments but were hopeful of more. Of particular value in identifying vetted experiments conducted up to the early 1990s was the sequence of three reviews and experimental tabulations as reported by Settles and Dodson.[50] Settles and Dodson were commissioned by NASA to identify and review (aided by a panel of notable experimentors), 2D, axisymmetric and 3D supersonic and hypersonic shock-wave/boundary layer experiments of several types, including compression corner, impinging shock and fin generated shock-wave/turbulent boundary-layer experiments. Additionally, a search for further experimental hypersonic impinging SWTBLI work reported since the Settles and Dodson review was conducted which was based in part upon the published reviews of Roy and Blottner,[51] Delerey and Marvin,[32] Knight, et al.,[52] as well as extensive search of AIAA and other papers and publications for both experiments and simulations of experiments, recent PhD dissertations and reports from Foreign national agencies, and of Bradshaw's online turbulence bibliography database.[53]

Specific factors used in considering impinging SWTBLI experiments for potential use in this study were that they be:

1. Hypersonic conditions ($M > 5$ with a preference for those of High-enthalpy Real-Gas, but also Perfect Gas conditions).
2. Well-defined geometry as to surface where the test boundary layer develops and as to the shock generator.
3. Well-defined and (steady) free-stream (P_T, T_0).
4. Well-defined upstream 2D or axisymmetric turbulent boundary layer with known transition, and which exhibited agreement with accepted correlations (e.g., Kármán-Schoenherr[28]), preferably not tunnel wall experiment, but with experiment generated either on flat plate or cylinder. Cold-wall boundary condition with accurately known wall temperature, T_w.
5. Attached, Incipient Separation, and Fully Separated cases, with: a. Post-Reattachment wall heating expected to conform to $(Q/Q0) \approx (P/P0)^{0.85}$ correlations, and; b. Separated regions, examined for λ-shock, and free interaction correlations.
6. Instrumentation: a. Familiarity and generally accepted instrumentation quality; b. Redundancy-direct and indirect; c. Wall Pressure (most reliable); e. Wall Heating (not adiabatic wall), and; e. Wall Shear Stress, if available.
7. Flowfield Measurements, with a. Pitot and Temperature Probe surveys, log-law of wall region, and; b. Flow Visualization, surface and flowfield

8. Other reported experiments at same facility or by same experimental group, including: a. Reputation of Facility based on other experiments, and; b. Reputation of Researchers based on other experiments.
9. Other previous reported simulations of experiment.
10. Is experiment available as tabulated DataSet (or at least determinable from published plots)?
11. Reasonable Experimental Accuracy Assessments by Experimentors.

Many of the impinging SWTBLI experiments available in the literature proved to be supersonic, mainly adiabatic wall, with some conducted on tunnel or nozzle walls, making them of tertiary interest. Supersonic experiments (Mach 3 and below) prevail largely since such facilities have been more common and less expensive to operate (without heating of the stagnation temperature above room-temperature, liquification effects can occur for free-stream air above Mach 4).

Of the hypersonic experiments identified, only three were found to be suitable as use in a "Primary" role for the purposes of this study. Regrettably, no turbulent hypersonic experiments which reported or were likely to have Real-Gas effects were identified, although one laminar experiment was located. The inability to locate a turbulent hypersonic case with real-gas effects, is believed to be related to the contradictory operating requirements for the required High-Enthalpy, High-Reynolds number facility, other than potentially a ballistic range or flight case. As a consequence, the consideration of real-gas effects for hypersonic impinging SWTBLI flows are studied herein by construction of a 'nominal-trajectory' flight case for the purposes of sensitivity study.

III.E.1. Schulein Mach 5 Experiment Overview

Schulein[54,55] conducted a Mach 5, impinging SWTBLI experiment, which upon review proved to be well-executed, with excellent instrumentation, and having extensive thorough documentation. It was conducted in the DLR Göttingen Ludwieg Tube facility, having a useful test time of 0.3 seconds for the test conditions. The nominal free stream conditions were $P_T = 2.12$MPa, $T_0 = 410$K, $T_w = 300$K, $ReU = 37 \cdot 10^7$/meter, $U_\infty = 830$ mps, and $H_{0,\infty} = 0.41$MJ/kg, with air as the working medium. The instrumentation included *Pressure Systems, Inc.* 32-port modules similar to that used extensively by NASA for the measurement of pressures. The skin friction measurements were obtained by independent redundant approaches: a. the proven oil-film technique,[56–62] similar to that used at NASA for supersonic and hypersonic flows; and, b. that of the well-established indirect log-law-wall deduction of wall skin friction from probe measurements. The wall heating was also measured by redundant techniques: a. Calibrated infrared camera, and b. semi-infinite wall gauges. An additional redundancy in the wall heating measurement can be indirectly deduced from the pressure measurements from the $(Q/Q_0) \approx (P/P_0)^{0.85}$ correlation. The experimental uncertainties are determined to be $\approx 2\%$ for pressures, $\approx 10\%$ for skin friction, and $\approx 20\%$ for heat transfer. Probe surveys were obtained, as well as high-quality schlieren flow visualization for all cases. For the total enthalpy given, no dissociation would be anticipated, nor would there be 'real-gas' effects. The upstream boundary layer was developed on a 2D flat plate of distance $x_0 = 0.350$ m before the interaction, and as will be seen conforms to proven turbulent correlations. Four flow cases can be considered:

1. G0 - a 2D nominal zero-pressure-gradient flat-plate boundary layer;
2. G6 - an attached impinging SWTBLI case with 6 deg nominal shock generator angle;
3. G10 - an incipient impinging SWTBLI case with 10 deg nominal shock generator angle, and;
4. G14 - a separated impinging SWTBLI case with 14 deg nominal shock generator angle.

The shock generator is relatively 'long' with respect to the boundary layer thickness, $L_{gen}/\delta_0 \approx 1000$ giving spatial separation for the various topological features of the impinging SWTBLI flowfield.

The source document[54] describing the experiment is extensive and well-organized, with all the information tabulated that might be needed to accomplish the simulations. Further publication in the open literature describe the experiment procedure in depth.[55] A number of prior computations for this experiment have been reported[63,64] allowing for comparison of the present work with independent simulations.

III.E.2. Murray Mach 9 Experiment Overview

The Mach 8.9 experiment of Murray[65,66] was conducted in the Imperial College Nitrogen gun tunnel previously used in the classic hypersonic compression corner studies of Elfstrom[68] and of Coleman and Stollery.[36] It has a steady test time of approximately 5 millisecond. More recently, Hillier has provided a series of

studies[66,67] culminating, with Hillier as advisor, in the most recent work, that of the Murray PhD dissertation. The experiment was conducted on a hollow axisymmetric cylinder, of diameter=75mm, as the test surface placed in the gun tunnel nozzle. The shock generator for the attached case is an axisymmetric cowl of 4.7 deg internal angle, whereas that of the fully-separated case has a 10 deg internal angle. The geometry of the shock generator cowls is given by means of figures in the dissertation. The instrumentation is limited to providing only wall pressure, wall heating and schlieren flow visualization. Wall heating instrumentation was that of thin-film resistance temperature gauges, making use of the time history of the gauge, and solving the one-dimensional heat transfer equation. As the data was not available in tabulated form, the data from the figures of the Murray PhD dissertation was extracted by means of the digitization program g3data.[69] The nominal test conditions cited are $P_T = 60$MPa, $T_0 = 1150$K, and $M = 8.9$, giving $U_\infty = 1445$mps. The unit Reynolds number for these conditions are given as $ReU = 47.4 \cdot 10^6$/m. The total enthalpy, $H_{0,\infty} = 1.1$MJ/Kg of the experiment, particularly with Nitrogen as working gas, is insufficient to precipitate dissociation and related real-gas effects. Additional cases involving an offset in the cowl from the cylinder provided 3D cases which are not considered for the purposes of the current paper.

Measurements of the cylinder wall pressure upstream of the shock impingement is indicative of an axial gradient in Mach number for this facility, which made it initially difficult to match in the present simulations all of the nominal test conditions and the measured upstream boundary layer wall pressure. A search for reports related to operation of this gun tunnel resulted in the publication by Mallinson, et al.,[70] which describes the gun tunnel nozzle as providing a conical flow rather than a uniform free stream. Mallinson provides the flow angularity variation of the nozzle. Such an initial profile was analytically expressed and numerically generated as an input for the present simulations which reasonably replicated the upstream pressure distribution on the cylinder while conforming to the stated nominal free stream conditions. All simulations conducted in this study for the Murray cases make use of this approach. The boundary layer results provided by Mallinson supplement the experiment, indicating transition location. A wall temperature of $T_w = 300$K was assumed for all simulations of the present study.

The shock generator is 'short' relative to the upstream boundary layer thickness at $L_g/\delta_0 \approx 100$, meaning that flow topology features, as originate from the shock generator leading edge and also originate from the shock generator trailing edge, might be seen to merge in the region of shock impingement.

Murray provides experimental error analysis estimates of $\pm 2.3\%$ for pressure measurements, and $+8.7\%$ to -2.2% for heat transfer measurements. Such estimates for pressure are well in line with other facilities, whereas these estimates for heat transfer are considered 'tight' by this author, who normally expects $\approx 10\%$ for heat transfer measurements, but the experimentors estimates are quite possible what with the modern techniques, and the extensive experience, reputation and support available for this facility.

III.E.3. Kussoy and Horstman Mach 8 Experiment Overview

The Mach 8.18 experiment of Kussoy and Horstman[73] was conducted on a 2D flat plate in the NASA Ames Research Center '3-1/2 ft' Hypersonic facility, now mothballed. It was a high-pressure, gas-heated pebble-bed blow-down facility, having long run time (minutes), and saw extensive use in the development of the Apollo and Shuttle programs as well as basic hypersonic flow research. It had a reputation of being capable of matching flight transition. It also enjoyed a considerable range of experience in its support and research staff with hypersonic instrumentation and operation.

The nominal test conditions given are $P_T = 60$atm, $T_0 = 1166$K, giving $H_{0,\infty} = 1.17$MJ/Kg, and $ReU = 5 \cdot 10^6$/meter. The working gas is air. Tunnel test time is given at 20 seconds, with a useful test time of 3 minutes under these conditions. The flat plate test surface was water-cooled. Wall temperature is given as $T_w = 300$K nominal, and the wall temperature rose only 5 degK during a 3-minute run, with cooling turned off while heat transfer was measured. Variation in total temperature during a 3 minute run is given at ≈ 50K. Run-to-Run variations in pressure and Mach number were found to be less than 0.5%, however.

The test surface was a sharp flat plate, 76 cm wide, 220 cm long. The plate is pitched at -2 deg angle of attack as is good practice to increase the test Reynolds number, and provide a uniform two-dimensional flow over the plate. The shock generator could be inclined at angles from $5 - 15$ deg allowing for determination of incipient separation. The location of the shock generator leading edge relative to the leading edge of the flat plate varied so that the shock generated would impinge on the flat plate at the location of densest gauge placement (1 cm spacing), but is given for each case. The primary case herein considered is that of the 10 deg wedge with fully-separated flow.

The pressure cells used were a high-accuracy Barocell for P_T and *Pressure Systems, Inc* strain gauge

modules similar to that of Schulein. Pressure calibrations of all instruments were traceable to National standards by means of a dead-weight test-stand used extensively in these facilities. The experimentor states estimates of experimental uncertainty for surface pressure as being $\pm 10\%$ or ± 80 N/m whichever was higher. However this seems by this author based on experimentors experience and related facility reports to be an overly conservative.

The heat transfer rates were measured by two means: a transient thin-skin method; and, a thermopile method. The transient thin-skin method made use of chromel-constantan thermocouples spot welded to the test bed, and relied on a $10 - 50$ degK temperature rise (with cooling disconnected) during a 20-second heat-transfer run. The thermopile method made use of Schmidt-Boelter gauges, measuring a temperature difference across a known substrate. Surface heat transfer uncertainty was corrected, by a simple procedure described, for run variations in total temperature of up to 50 degK or about 0.5%. However, overall uncertainty in Heat Transfer included uncorrected lateral conduction effects and is cited to be $\pm 10\%$, which seems to this author to be realistic.

Skin friction and boundary layer properties were obtained by means of pitot and static pressure probe surveys. Total temperature probe surveys were also conducted. Cobra probes gave flow direction. Skin friction was deduced based upon log-law-of-wall relation with measurements transformed by VanDriest-II relation,[27] and is given for the upstream boundary layer as $Cf = 0.00098$, with $\delta_0 = 3.7$cm, $\delta_0^* = 1.59$cm, $\theta_0 = 0.094$cm. Further useful upstream boundary layer properties are $\tau_{w,0} = 19.6 N/m^2$, and $Q_0 = 10400 W/m^2$. Useful upstream freestream properties are $P_\infty = 430 N/m^2$, $\rho_\infty = 0.0187 kg/m^2$, $T_w = 300$K, $T_\infty = 81$K, $U_\infty = 1446$m/sec. Although oil-film interferometry had been applied in this tunnel at similar conditions, regrettably that instrument was not applied.

For the flow field quantities, the estimated uncertainties were estimated to be $\pm 2\%$ for the total temperature, $\pm 10\%$ for the static pressure, $\pm 6\%$ for the static temperature, $\pm 12\%$ for the density, $\pm 3\%$ for the velocity, $\pm 3\%$ for yaw angle, and $\pm 5\%$ for the pitot pressure. The uncertainty in Y was $\pm 0.02 cm$. No uncertainty estimates for boundary layer properties are provided by the experimentor, but $\pm 5 - 10\%$ seems appropriate to this author.

One uncertainty unreported comes about since the shock generator is moved over a limited range of X-positions, about $\pm 3\%$ in position between runs, so as to sweep the nominal shock impingement location over the array of fixed pressure taps and fixed heat transfer measurement locations so as to improve resolution of these measurements. As the X-variation in upstream boundary layer properties is weak, no accounting is made for this positional uncertainty.

III.E.4. 'Nominal-Trajectory' High-Enthalpy, Turbulent cases

No experiments were found of the impinging shock-wave/turbulent boundary-layer interaction that were of sufficiently high-enthalpy condition so as to exhibit real-gas/dissociation effects. However, there are *laminar compression-corner* SWBLI cases, of which the experiment by Mallinson, Gai, and Mudford[70] showed real-gas effects. The experiment was conducted for 3 conditions at a range of Mach and Total enthalpy ($M = 9.0, 7.5,$ and 7.4, and $H_0 = 2.85, 13.7,$ and 19.1MJ/Kg respectively, so as to examine real-gas effects on separation. Total pressure was held constant in the range of $P_T \approx 22.6 - 21.6$MPa. A range of ramp angles varied the strength of the interaction to vary from attached through fully separated. By examining the measured behaviour relative to correlations to account for known compression corner dependencies, observations as to the influence of *total enthalpy*, $H_{0,\infty}$, were deduced. The effect of increase in total enthalpy, appears to have led to dissociation effects within the separation bubble, where the observation was that the dissociation resulted in a decrease in the extent of separation, and a more diffuse heat transfer rise upon reattachment.

As a physical basis for the observed real-gas effect, a decrease in gas temperature due to either dissociation within the separation bubble or due to variable specific heat may lead to a decrease in realized pressure rise, decreasing the extent of separation, an effect that well could also occur in turbulent impinging shock cases.

To examine by means of a 'sensitivity' study and to provide a basis for 'Ground-to-Flight' traceability, as to the potential effects of real-gas dissociation or of air as a calorically imperfect gas on *turbulent impinging* SWTBLI cases, we constructed 'nominal-trajectory' high-enthalpy, turbulent cases possibly relevant to scramjet engine performance. To set the conditions, we made use of the published trajectory of Billig[1] for typical scramjet conditions, choosing as test cases two conditions: one of which is similar to that of Kussoy[72] at Mach 7, with $\rho_\infty = 4.401 \cdot 10^{-2}\ Kg/m^3$, $T_\infty = 220.94$k, $H_{0,\infty} = 2.4$MJ/Kg, $T_w = 500$K, and other for a higher altitude Mach 14 case, where $\rho_\infty = 9.811 \cdot 10^{-3}\ Kg/m^3$, $T_\infty = 246.93$K, $H_{0,\infty} = 9.97$, and $T_w = 400$K. Both Mach numbers had an attached case with a shock generator angle of 5.5 deg, and a separated case with

a shock generator angle of 10 deg. Only the Mach 14, with the 10 deg shock generator exhibited real-gas effects and is the only one presented in this paper. The upstream boundary layer development length was chosen so as to ensure turbulent flow, with transition based on a Re_θ correlation derived from the three experiments. Cases were run with Air as a Perfect Gas, and with Air using the Park 5-species chemistry model.[74] Naturally no experimental results are directly available for comparison with simulations, but the purpose of such simulations are to examine the 'sensitivity' of the numerical simulation of the physics of separation to real-gas effects, and the various correlation discussed above may be used with reservations as the correlations are being used outside the range for which they were formed.

IV. Results

In this section, we first examine the upstream boundary layer development for the Schulein and for the Murray experimental hypersonic cases in comparison with CFD results for the several turbulence models used in this study. Note that we conduct in Appendix B, a brief study of sensitivity of a Mach 10, Cold-Wall turbulent boundary layer to implementation details of the SST Turbulence model and incorporate those options shown in Appendix B to have positive results into the main body of this work so as to further examine their impact on these cases as well . Then, a grid sensitivity study for an inviscid form of the Schulein shock-wave experiment will be conducted to document an inviscid source of error that must be dealt with to properly conduct these types of simulations. Then, the Schulein shock-wave/turbulent boundary-layer interaction will be examined in detail for the attached, incipient separation, and fully separated cases. Subsequently, the Murray SWTBLI cases and the Kussoy SWTLBI cases will be examined. Uncertainty estimates of the RANS CFD solutions for these cases will be considered, making use of both the experiment and applicable correlations.

IV.A. Flat-Plate Cases

In each of the shock-wave/turbulent boundary layer interaction cases selected for this study, the upstream hypersonic boundary layer is well-behaved, either 2D or axisymmetric, fully turbulent and is documented, albeit to varying degrees. As the behaviour of the boundary layer in response to the SWTBLI depends on the state of the upstream boundary layer, it is of benefit to briefly examine the upstream boundary layer development for each of the selected experiments to ensure proper specification of flow conditions and as to establishment by the computation of the boundary layer immediately upstream of the SWTBLI. As a consequence, prior to examining the SWTBLI regions proper, we first examine the nominal zero-pressure-gradient boundary layer development upstream of the interaction region for each of the experiments, and compare with RANS solutions for the various models. Due to the limited upstream boundary layer data of Kussoy, the upstream boundary layer for that case will be deferred and examined in the same subsection as the rest of the Kussoy SWTBLI.

IV.A.1. Schulein $M_\infty = 5$, 2D Flat Plate Boundary Layer

Schulein[54] provides considerable documentation of the upstream boundary layer development, including wall pressure, surface heating, and probe surveys. Figures 2-5 provide wall property behaviour upstream of the interaction for wall pressure, wall heating and wall shear stress as determined experimentally, from boundary layer correlations and from the current RANS solutions using several turbulence models.

The RANS solutions are obtained using DPLR V4021 in its *standard*, unmodified form, for the Baldwin-Lomax, Spalart-Allmaras, SST, and Wilcox-2006 $K-\omega$ turbulence models. For the SST and $K-\omega$ models, the *standard*, unmodified version of DPLR is equivalent to the choice of Vorticity-based production, no compressibility correction, 1st-order convective terms, and the iWallBC1=1, iOmegaAn=2 model implementation options. The grid used is 528x3x128 in 3 blocks. Initial cell of the surface is placed so the $y_1^+ \approx 0.05$ and $ReCell = 0.25$. Transition is set according to the experiment to occur at $X_{tr} \approx 0.1$m, for which laminar simulations give $Re_\theta \approx 500$.

Figure 3 is a plot of wall shear stress against distance from the flat plate leading edge, showing experiment results, VanDriestII transformed correlation of White, and the RANS simulation results for the several turbulence models. Figure 4 is a similar plot but of wall shear stress against Re_θ so as to compare with the VanDriest-II transformed correlation of Kármán-Schoenherr. Note that for the ReX correlation, common practice is to employ a shift in virtual origin to account for transition. Such a shift is not allowed for the Re_θ

correlation, since Re_θ already accounts for the initial laminar portion of the boundary layer development. The Spalart-Allmaras model agrees with the correlations and experimental data for the wall shear stress, with the remaining models, including the Baldwin-Lomax model, appear about 10% low.

In figure 5, the Baldwin-Lomax, SST, and $K-\omega$ turbulence models are seen to agree amongst themselves and the experimental measurements as to heating within experimental scatter, but with the Spalart-Allmaras model giving 10% overprediction in heating. This is in contrast to the wall-shear stress comparison, where the relative performance of the turbulence models is reversed.

Figure 6 shows profiles of normalized turbulence variables, K and ω, for SST solutions for the Schulein flat plate. For the near-wall sublayer region, sufficient terms in both the K and ω equation become negligible and the PDE's become nonlinear ODE's which can be solved analytically. These solutions are known, e.g. Wilcox[10] with $\omega_{sublayer} = 6\mu/\beta_\omega \rho y^2$, whereas $K_{sublayer}$ having the form ay^n. Plots of normalized K^+ and $1/\omega^+$ can then be used as part of a *verification* of the turbulence equation solution procedure for at least the sublayer region since these are known analytic solutions against which the CFD profiles can be compared. It should be pointed out that what are shown in Figure 6 are not single profiles, but are actually **all** of the turbulent profiles for this particular case. Also, we point out that other plots, not shown, containing **all** the normalized profiles for locations fully turbulent also agree equally with each other for all cases contained in this paper.

IV.A.2. Murray $M_\infty = 8.9$, Axisymmetric Cylinder Boundary Layer

Murray reports nominal test conditions of $M = 8.9$, $T_0 = 1150K$, and $P_T = 60MPa$, but mentions a negative streamwise pressure gradient throughout the test region. The test surface of Murray is actually a hollow cylinder of 75 cm diameter with its axis aligned along the nozzle centerline, and with 2 cowls of differing internal angles and diameters to generate the impinging shocks. Note that N2 is the working gas for this facility. In our first trial attempt to compute the cases of Murray we made the simplification of constant freestream conditions at the nominal test conditions as reported by Murray and found that it was indeed necessary to account for the streamwise pressure gradient of this facility. Fortunately, the report by Mallinson, et al.[71] provides the required calibration details for the Imperial College Gun Tunnel nozzle operating conditions. Mallinson describes the facility as having a conical nozzle design which yields a diverging set of streamlines, but which can fairly easily be incorporated into the initial inlet conditions as a specified inlet boundary condition profile (rather than uniform freestream) for the CFD setup that we finally settled on for use in the CFD results for this current paper.

To generate this inlet condition for our CFD simulations, we derived the conditions at the cylinder leading edge to be $\rho_\infty = 0.1510289\ Kg/m^3$, $T_\infty = 68.28$K, and *total* freestream velocity of $U_\infty = 1499.07$m/sec. To account for the conical diverging streamlines of the tunnel nozzle, the flow angle was then calculated from a fit of the curve given by Mallinson,[71] with flowfield divergence angle of $\alpha = 5\,\mathrm{deg}/\mathrm{meter} \cdot R$, where α is the off-centerline conical divergence, and $R = \sqrt{y^2 + z^2}$ is the distance off-centerline at the X-station of the leading edge of the cylinder. The (u, v, w) components for the computational inlet boundary corresponding to the cylinder leading edge were then computed accordingly.

From experimental data of Mallinson, transition to turbulence occurs on the test cylinder at $0.09 - 0.15$ meters from the cylinder leading edge, start to finish. The Re_θ at transition from laminar calculations is from $750 - 940$.

The computations were based on a 3D grid for this axisymmetric flow of 256x9x256, with the 1st point off the wall located at $y^+ = 0.1$. Only the quarter-plane was calculated. Computations for the test cylinder were accomplished using both the Baldwin-Lomax and the SST two-equation turbulence model, with specified transition location, and with the further two options of a simple uniform freestream at the inlet boundary condition of the cylinder leading edge, or of a pointwise boundary condition at the cylinder leading edge that represents the diverging nozzle as described above.

Figures 7 and 8 compare the current computations for the cylinder test surface of Murray compared to the data of Mallinson, et al., for wall pressure and for wall heating, respectively. Figure 9 provides supplemental information from the computations for wall shear stress (not measured in the experiment). The wall pressures in Figure 7 show better agreement with experiment for those Baldwin-Lomax and SST computations using the pointwise diverging nozzle boundary condition for the inlet boundary face rather than using the simple uniform nominal freestream. The effect of the diverging nozzle flow, of course, is a streamwise drop in cylinder pressure associated with a streamwise increase in boundary layer edge Mach number. Mallinson also describes comparisons they made of computations for the flow over the cylinder using

a nominal uniform freesteam with another computation with input conditions *calibrated* so that their final computed results almost precisely agree with the measured cylinder pressures. For our present paper, our purposes are different than that of Mallinson in that it is not calibration but rather evaluation of uncertainty, so we take the approach of making best use of information that is available in reports, etc. to accomplish setup of the CFD without actually fine-tuning to the measured pressure data itself.

With the use of a simple uniform freestream, Mallinson computed $3\% - 5\%$ difference in his calculated cylinder wall pressure and that actually measured, somewhat better than the current computations for uniform freestream, which range from -10% at the cylinder leading edge to $+2\%$ at $X = 0.6$m. For the current computations with the diverging nozzle boundary condition, there exists improved comparison with calculated wall pressures, but still with differences amounting from -2% at the cylinder leading edge to $+2\%$ at $X = 0.6$m. There is little difference in computed pressure due to turbulence model.

Figure 8 shows the wall heating comparisons. The Baldwin-Lomax result using the diverging nozzle boundary condition gives the best agreement with measured heat flux, starting 7% low just after transition, and 4% high at $X = 0.6$m. In contrast, the SST wall heating result using the diverging nozzle boundary condition starts 11% low just after transition, and becomes 12% high at $X = 0.6$m. Use of the 'erroneous' uniform freestream condition would have resulted in as much as an additional 5% error in wall heating. Murray accomplished RANS solutions using an axisymmetric solver with 970x260 cells and the one-equation version of Menter's turbulence model showing results for wall heating along the Mallinson Cylinder which are quite similar to the present SST turbulence model for the Diverging Nozzle condition.

Wall shear stress was not measured for this experiment, whether for the cylinder alone, or for the shock impingement cases, but Figure 9 provides the present CFD results for wall shear stress for the two turbulence models, and for the types of nozzle conditions, uniform freestream and diverging nozzle. Just as with the wall heating, the wall shear stress for the SST is higher by about 8%. Because there exists a streamwise favorable pressure gradient, the correlation results from VanDriest II-White are not plotted.

Although we could follow the approach of Mallinson in *calibrating* for the tunnel nozzle streamline divergence, we believe that our approach of making best use of readily available information as to tunnel conditions from reports, but without actual use of the data itself is an approach more representative to our current effort in our evaluation of likely computational uncertainties and their sources. As a consequence, based on our lack of knowledge as to initial boundary layer conditions we estimate a contribution of $\Delta_{Q_0} \approx 10\%$ to the overall computational uncertainty for the Murray SWTBLI cases.

IV.A.3. Kussoy and Horstmann $M_\infty = 8$, 2D Flat Plate Boundary Layer

Kussoy provided measurements for only a single boundary layer profile location just upstream of the shock-wave/boundary-layer interaction, with the intent that simulations would match this profile, starting the grid at the upstream measurement location with a specified inlet profile. However, that is not the approach for this uncertainty study, in that it has been our intent to approach the simulations in a manner similar to that of a designer where the geometry and flow conditions are known, but to not make direct use of the data prior to the simulations. As a consequence, we compute the flow over the entire geometry, starting with the leading edge of the flat plate, and then compare with the upstream boundary layer measurements. These simulations make use of a 4-block grid, having 96x3x128 cells each, and with $y_1^+ = 0.2$. Transition could not be determined from the experiment and so was set to occur in the CFD simulations at $X_{tr} = 0.4$ meters from the leading edge to give a Re_θ intermediate to that observed for the Schulein and for the Murray cases.

Figure 10 compares the measured velocity and temperature profiles for the upstream boundary layer with respective profiles as obtained with the Spalart-Allmaras and with the SST turbulence model. There appears reasonable agreement of the CFD results with experiment in the outermost portion of these profiles, where both models appear to be within $5 - 7\%$. The Spalart-Allmaras profiles (at 5% in velocity, 15% in temperature) appear to agree better with experiment than does the SST profiles (at 12% in velocity, and 15% in temperature) for the log-law region. The CFD simulations for these models appear to be within 5% of the stated experimental heat transfer for the upstream boundary layer. The documentation for this experiment provide skin friction (at $\tau_w = 19.2 N/m^2$) for this measured profile. The CFD results for wall shear stress are $17.5 N/m^2$ or 10% low for the SST model and $18.77 N/m^2$ or 5% low for the Spalart-Allmaras model. Based on our examination of the measured profile, the best information describing the upstream boundary layer are the profiles in velocity and temperature themselves and the cited $P_w = 430$ Pa, and $Q_{w,0} = 10.4 W/cm^2$. Using these two metrics, the CFD results describe the initial upstream boundary layer to within $\approx 10\%$ uncertainty.

IV.B. Inviscid Impinging Shock Case

Although the primary focus for this paper is on the uncertainty in hypersonic SWTBLI CFD simulations due to deficiencies in turbulence modeling for such flows, there remains a possible source of error associated with inviscid-related terms that warrants examination. This present work is being done in part to support development of scramjet technology. The function of inlet design for such an engine is to feed the combustor with air that has been compressed by a sequence of SWTBL interactions, possibly just short of separation, which yet retain as high a total pressure as possible. As will be discussed, for 2D designs at least, it appears that this is best done by accomplishing a sequence of SWTBLI's, with Mach ratios across each shock of $(M_2/M_1)^2 \approx 1/2$ or less. But to accomplish accurate analysis of each of as many as 5-7 interactions total, the inviscid prediction of the oblique shock problem must be highly accurate. To determine the magnitude of errors associated with the inviscid part of this problem, we construct an *inviscid* counterpart to Schulein's 14 deg experimental case, and track total pressure variations along selected streamlines, and compare with simple calculations based on oblique shock relations found in many textbooks, or the NACA 1135 tables,[14] as supplemented by the direct solution approach[20–22]

Figure 11 shows Mach color contours for DPLR simulations of the Schulein 14 deg experiment, but with DPLR being run in the *inviscid* mode only. There are no viscous terms, whether turbulent nor laminar, for this simulation. Naturally there is no actual data, as this is an analysis only. Also in Figure 11 are streamlines originating at the inlet. Note the streamline going down the center-most portion of the computational domain is shown as a *bold dash-dot* line in contrast to the other streamlines. Figures 12, 13, and 14 are plots showing the total pressure variations along each of these streamlines, again with the results for the centermost streamline being shown as a *bold dash-dot* line. Figure 12 is for a coarse grid of 528x3x128 cells, Figure 13 is for a medium grid of 1056x3x256 cells, whereas Figure 14 is for a fine grid of 2112x3x512 cells. Also shown in the total pressure vs. X plots is the analytical value $P_{T,2}/P_{T,1} \approx 0.73175$ for the single initial oblique shock generated by the 14 deg inclined shock generator. Note that, as the test problem is inviscid, there is no boundary layer formed on the generator, and thus, the ideal streamline deflection will also be 14 deg, leading to the simple analytical oblique shock problem. The coarse grid leads to as much as 4% error in $P_{T,2}/P_{T,1}$, the medium grid leads to as much as 1% error in $P_{T,2}/P_{T,1}$, whereas the fine grid leads to 0.6% error in $P_{T,2}/P_{T,1}$. The error is always biased low with too much total pressure loss and related entropy increase. Should a coarse grid be used to simulate a scramjet inlet with as much as 6 oblique shocks, this suggests that the accumulated error might be as high as $0.96^6 \approx 0.78$ or a 22% error in the primary physical quantity of interest. Clearly this would be unacceptable, so a means of reducing this error source to a more tolerable level needs to be found, both for design application, but also for the remaining simulations of this paper. One such approach is to alter the present inviscid flux treatment (modified Steger-Warming) appearing in DPLR so as to improve the behaviour with non-grid-aligned shocks, or a grid adaption scheme to internal shocks would be required, or the medium-to-fine grids would need to be used.

In the viscous solutions for the Schulein 14 deg case to follow, the primary results presented are computed on the 'medium' grid. However, to ensure grid convergence for that case, limited results using the 'fine' grid are compared.

Note that DPLR is used in NASA's program work normally for reentry vehicles with strong bow shocks but fitted grids, and without internal embedded shocks. Further, in the current calculations the use of high-density grids is allowable, since these are essentially 2D solutions, whereas for complex 3D engine inlet analysis, adaption to internal shocks and/or the use of high-density grids may not be practicable in a design optimization environment.

IV.C. Experimental SWTBLI Cases

IV.C.1. Schulein Mach 5, 2D SWTBLI Cases

The Mach 5 experiment of Schulein provides attached, incipient separation and fully separated SWTBLI cases. Note that in addition to the wall pressure and wall heating measurements, Schulein used redundant measurement techniques to determine experimental wall shear stress for these several cases. Also, we have the capability of using the pressure measurements, along with the $Q - P^{0.85}$ correlation, as a redundancy check on the direct measurements of wall heating. Due to the high quality of instrumentation and the redundancy of the experimental techniques, and the clear and unambiguous documentation of the experiment, the use of the Schulein experimental results for evaluation of current computational techniques for impinging SWTBLI predictive methods and for guiding future computational advances cannot be overstated.

These cases are computed using DPLR Navier-Stokes codes with several turbulence models and variations thereof. We consider each of these cases in order, describing comparisons of CFD with experiment, discuss relevant flow physics and evaluate the numerical values for the Uncertainty metrics of these flow cases in this subsection.

Schulein 6 deg *Attached Case:*

First considered is the attached, 6 deg Shock generator case of Schulein. For this case, simulations using DPLR and the SST, $K-\omega$ and Spalart-Allmaras models were obtained for a 528x3x128 cell grid, with $y_1^+ \approx 0.05$, and $Re_{Cell} \approx 0.25$. Note this is a weaker shock system than the 14 deg inviscid problem presented earlier, and results indicate the grid resolution used is adequate to resolve this case. Figures 15, 16 and 17 depict the wall-pressure, wall-heating and wall shear-stress variations with x through the interaction region for both the measurements and the CFD results for this case. The wall pressure profiles of figure 15 indicate an high-quality of agreement between the CFD results for all models as to the pressure levels achieved through the interaction, and as to the location of the shock impingement. This agreement is reflected in the numerical evaluations for the 'Peak Pressure Discrepancy' measure, Δ_{PPeak} as defined above, reported in Table 1 for this case. For all the turbulence models used for this case, the pressures were within 2% of experiment.

As a check on the levels obtained for the pressure plateau shown in figure 15, we accomplish an inviscid shock analysis, where first the pressure rise $(P_2/P_1)_{Inv}$ and the Mach number, $M_{2,Inv}$, decrease through the impinging shock generated in turning the flow to align with the 6 deg shock generator is evaluated, followed by the reflexion shock turning the flow back by the same 6 deg so as to realign with the test surface leading to a further pressure rise $(P_3/P_2)_{Inv}$. This double-shock inviscid problem leads for a Mach 5 initial freestream encountering a 6 deg shock generator gives the result for the overall pressure rise of $(P_3/P_1)_{Inv} = 3.762$, along with an initial pressure of $P_\infty = 4330Pa$ gives a plateau pressure of $P_{Peak,Inv} = 16,290Pa$. This inviscid analysis proves about 2% lower than the experiment and the viscous turbulent solutions presented in Figure 15. Note that the boundary layer forming on the shock generator causes the apparent angle of the shock generator to be slight larger than the nominal 6 deg, sufficient so as to lead to a slightly higher impinging shock angle and higher resultant plateau pressure. This simple check lends added credibility to both the experiment and to the computed results for pressure.

Clearly the pressure level of the extended pressure plateau region is the consequence of the impinging shock followed by the reflexion shock, but what leads to the termination of the pressure plateau? That appears to be the consequence of the expansion fan emanating from the trailing edge of the shock generator weakening the reflexion shock, eventually lowering the pressure and terminating the pressure plateau region. The thin boundary layer thickness for the Schulein experiment establishes the extended distance over which the interaction presents itself, and the long length of the shock generator relative to the boundary layer thickness, $L_{gen}/\delta \approx 1000$, enables the extended region of the constant pressure plateau. These arguments, as will be seen, seem to justify the suitability of applying the inviscid double-shock analysis to this case, and also apply to the remaining Schulein cases, but not to the Murray cases nor to the Kussoy and Horstman cases which have a much shorter shock generator relative to their boundary layer thickness.

Figure 16 provides wall-heating comparisons of experimental measurement and wall-heating as derived from the wall pressure measurements using the $Q \approx P^{0.85}$ correlation. Also in figure 16 are the DPLR wall-heating results for the three turbulence models. In contrast to the wall pressure results, the discrepancy between the simulations and the experimental results for wall-heating are in the range of $25-35\%$, with these results reported also in Table 1. The disagreement between the wall heating measurements and the $Q \approx P^{0.85}$ correlation gives indication that the wall heating measurements may have been low for this case, with much better agreement between the CFD results and the wall heating correlation results. The reasons for this are not clear. It is anticipated that through the shock interaction, the boundary layer will be compressed, leading to an increase in pressure, density as well as affecting the temperature profile. Furthermore there will be a significant reduction in boundary layer thickness, all of which lead to the observed increase in wall heat transfer. Once the rapid compression process of the interaction is passed, the boundary layer would be anticipated to again return to its gradual growth in thickness, with an attendant decrease in heating. However, the levels of heating should still be anticipated to be approximated by the $Q \approx P^{0.85}$ correlation within the immediate vicinity of the shock interaction. Note that the SST heating results appears to be approaching asymptotically the heating results obtained using the $Q \approx P^{0.85}$ correlation. Regardless, the actual wall heating measurements are that which were used for evaluating the Uncertainty measures,Δ_p ,

reported in Table 1.

Wall-shear stress results of Figure 17 compare the CFD results with shear stress measurements as determined from log-law analysis of pitot probe surveys. The oil film measurements shown are actually 'flat-plate' measurements, but shown truncated at the location of the interaction to avoid confusion as wall shear-stress measurements using the oil-film method for the attached interaction itself were not reported. Upstream of the interaction, the Spalart-Allmaras wall-shear stress agrees best with these measurements, whereas the SST and $K-\omega$ model are about 10% low. This contrasts with the upstream wall-heating comparisons where the SST and $K-\omega$ results give slightly better agreement with experiment than does the Spalart-Allmaras model. It would seem not possible to match the upstream boundary layer measurements in all regards with the current state of development of these models. As a consequence we report in Table 1 that there is an numerical value of 10% for the upstream boundary layer 'Discrepancy' metric, Δ_{Q0}. This is repeated for the remaining cases as well. Also clear in the Figure 17 CFD results is that although wall shear stress approaches zero for those X-stations closest to shock impingement, the flow remains attached, as does the experiment.

Also in Figure 17, after reattachment there exists a plateau in the wall shear stress levels, whether for CFD or the measurements corresponding to the plateau region for pressure and heating. In this post-interaction region, the Spalart-Allmaras and the $K-\omega$ model results are within 3%, whereas the SST wall shear stress results are about 12% lower than measured.

The Discrepancy metrics representing the numerical values for the normalized differences between CFD simulations and experiment are accumulated in Tables 1-6 for each of the experimental cases considered in this paper. All Tables are located in the separate 'Tables' section towards the end of the paper, just before the 'Figures' section.

Schulein 10 deg *Incipient Separation Case:*

Next considered is the incipient separation, 10 deg Shock generator Schulein case. Figures 18, 19, and 20 give the wall pressure, wall heat transfer (both of the wall heating and of the $Q \approx P^{0.85}$ wall-heating correlation), and wall-shear stress experiment vs. computational comparisons, respectively. Again the three turbulence models (SST, $K-\omega$ and Spalart-Allmaras are used for the computations. Table 2 presents the numerical evaluations of the Uncertainty 'Discrepancy' between CFD and experiment for this incipient separation case.

In Figure 18, the spacing of the pressure measurements precludes any clear indication of what small amount of separation might exist. However, the SST computed results for this case shows indication of the largest CFD simulation bubble, with the $K-\omega$ computed results giving about 1/2 the spatial extent of separation, and the Spalart-Allmaras model computed results indicating little or no separation. The level of agreement as to pressure of the CFD simulations compared to experiment are comparable to that of the fully attached case. The peak pressure plateau level, whether by experimental measurement or by CFD computations of any of the three models agrees within 1% of the pressure plateau level, $P_3/P_1 = 7.63$ or $P3 = 32850$ Pa, as evaluated by means of the inviscid two-shock analysis described earlier.

Similar to the attached case, Figure 19 indicates the experimental heat transfer measurements appear low relative to the $Q - P^{0.85}$ correlation($\approx 10\%$). Although the $Q - P^{0.85}$ correlation provides a nearly constant heating level for the constant pressure region past reattachment, the experimentally measured wall heating having achieved its maximum value just past reattachment experiences a slight decline with progression along the peak pressure plateau region, as was seen for the 6 deg case, likely due to the boundary layer, having undergone significant compression and thinning, returning to its natural growth process for the nearly zero pressure gradient region past reattachment.

Also shown in Figure 19, the SST, $K-\omega$ and Spalart-Allmaras computed heat transfer each exhibit a significant overshoot well above the experimental heat transfer at a location past reattachment and at the start of the experimental peak plateau region. In contrast through the separation bubble region, the turbulence models indicate a drop in wall heating whereas the experiment indicates a slight rise. The overshoot in heating as predicted by these models just past reattachment and the inability to predict any rise in heat transfer for the separation bubble represent the major contributions to uncertainty for the prediction of these impinging SWTBLI cases, as reflected in the numerical values entered in Table 2 describing the Uncertainty 'Discrepency' evaluations for this case.

Wall-shear stress measurements were accomplished for this case, using two methods, as obtained using the oil-film method and also by analysis of the log-law region of a velocity profile obtained by means of pitot probe survey. The agreement between the two experimental methods for wall-shear stress, as seen in Figure

20, is excellent, being within ±5% for the upstream boundary layer, and ±10% for the attached flow past reattachment. The turbulence models agree with the upstream measurements within ±10%, whereas past reattachment, the SST model appears 10% low, and the $K-\omega$ and Spalart-Allmaras being well within the experimental scatter. The SST model agrees quite well with experiment as to the extent of separation as indicated by the oil film measurements and as to the actual values of the wall shear stress. The $K-\omega$ model separation bubble indicated from computed wall shear stress is slightly smaller than both that of the SST model and the experimental wall shear stress. The Spalart-Allmaras model wall shear stress results for this case does exhibit a drop in wall shear stress due to the shock impingement but does not indicate any degree of separation.

Schulein 14 deg *Full Separation Case:*

Schulein provides extensive documentation as to a fully separated case, making use of a 14 deg Shock generator. Unless indicated otherwise, 'medium' grids with 256 cells between the flat plate and the shock generator were used for all of the computational results. The 'medium' grid had initial spacing off the wall chosen so as to provide $y_1^+ \approx 0.05$ and a Cell Reynolds number of 0.25.

Figures 21-24 depict contour plots for the SST simulations for this case. Flow is from left to right per "*NASA-standard*" in these figures. Figure 21 depicts the entire computational domain along with U-velocity color contours and Mach number line contours. The test surface is the lower boundary along the bottom of the figure, the shock generator, of length in the x-direction of ≈ 0.3m, is that portion of the upper boundary canted at 14 deg to horizontal. A boundary layer develops on both the lower flat plate test surface and also on the canted shock generator. Transition is specified at X=0.1 meters from the leading edge, where $Re_\theta = 600$. A weak leading edge shock is generated at the leading edge of the test surface which is seen in Schlieren photos available in the source document for this flow. A further weak Mach wave emanates from the transition of the boundary layer. For computational purposes, a symmetry plane boundary condition is applied for the upper boundary past the shock generator trailing edge.

Figure 22 is an expanded view of Figure 21 concentrating on the shock impingement region at about $x =$ 0.34 meters. Figures 23 and 24 provide pressure color contours and temperature color contours respectively. Flow topology features are seen to be widely separated with the impinging shock as generated at the shock generator leading edge, the reflexion shocks and the shock generator trailing edge expansion wave creating distinctly defined inviscid regions of nearly constant Mach number, velocity, pressure and temperature. The separation bubble with its signature λ-shock is clearly identifiable. The reversed flow is marked in dark blue in Figures 21 and 22. The boundary layer marked by white contour lines is seen to be lifted above the separation bubble, then turns back to the surface to close the separation bubble at the reattachment location. Also seen in Figures 23 and 24 are the clearly identified regions of elevated pressure and temperature in the inviscid flow just above the boundary layer for the pressure plateau region past reattachment. The inviscid flow immediately adjacent to the boundary layer for a distance past reattachment is defined by the reflection shock traveling upwards from reattachment and the expansion wave traveling down from the generator trailing edge. The distance in X between these two flow features allows the pressure plateau region to develop with an extended region of constant pressure before being terminated by the shock generator trailing edge expansion wave. As the extent of the interaction is affected by the initial boundary layer thickness, and the extent of the pressure plateau region is affected by the distance between the impinging shock generated by the shock generator leading edge and the trailing edge expansion wave generated by the shock generator trailing edge, then a reasonable non-dimensional quantity to consider is the ratio of the shock generator length to the boundary layer thickness, L_{gen}/δ_0 which for the Schulein experiment is about 1000.

Figure 25 compares the experimental measurements of the wall pressure distribution with the present computed results for the SST, $K-\omega$ and Spalart-Allmaras turbulence models. Figure 26 similarly compares the wall heating measurements with the computed results, whereas Figure 27 accomplishes this for the comparison of wall heating as obtained by means of the $Q-P^{0.85}$ correlation. Figure 28 presents the wall shear stress comparisons. Table 3 then accumulates the numerical evaluations of the Uncertainty 'Discrepancy' of the several turbulence models for each respective physical quantity of interest, (e.g., $\Delta_{LSep} \equiv (L_{Sep,SST} - L_{Sep,Expt})/L_{Sep,Expt}$, etc), for this case as might be evaluated from the data forming these figures.

In Figure 25, observed is the excellent agreement between all turbulent model results with experiment as to the pressure levels past reattachment and along the peak pressure plateau leading to and including the drop-off where the pressure plateau is terminated by the shock generator trailing edge expansion fan. Within

the separation bubble region, however, generally the turbulence models tend to underpredict the bubble pressure relative to the experimental measurements by about 1/2 or 50%. The extent of the separation bubble pressure region is best predicted by the $K-\omega$ model with a slight underprediction, whereas the SST model appears to underpredict the extent of separation by 1/4, whereas the Spalart-Allmaras model underpredicts the extent of separation by 1/2. The peak pressure plateau level, whether by experimental measurement or by CFD computations of any of the three models agrees within 1% of the pressure plateau level, $P_3/P_1 = 13.62$ or $P3 = 58675$ Pa, as evaluated by means of the inviscid two-shock analysis described earlier. Further note that the positioning in x as to the location of the pressure rise, an indication of the shock impingement location, agrees quite well between all of the turbulence models and the experiment. As there is no adjustment in x to force this agreement of shock impingement location(nor are there any such shifts in x for any of the solutions presented in this paper), this type of agreement increases credibility of our understanding of the documentation describing the experiment and of the overall solution process.

Figure 26 presents the wall-heating results for this fully-separated case. Whereas the $K-\omega$ heat transfer results are slightly low at the beginning of the interaction, it is the SST model heat transfer results that exhibits a severe spike or overshoot past the reattachment location-just prior to the region of the experimental pressure and heating peak plateau. The SST model heat transfer peaks at about 50% above the experimental peak value, but does decline towards the plateau level. The Spalart-Allmaras model does not actually exhibit an spiked overshoot in wall heating, but levels off about 25% above the experimental level. In contrast, the $K-\omega$ model heating has a slight overshoot followed by a decline to the approximate level of the experimental heating. A further deficiency in all of the turbulent model results for wall heating is that they all show little or no increase in wall heating through-out the separation bubble region, whereas the experiment shows about a factor of two rise above the wall heating of the initial boundary layer. The wall heating decrease for the turbulence model results of Figure 26 in the separation bubble region is incongruent with the observation of raised temperatures within the separation bubble as seen in the temperature contours of Figure 24, and is a likely region for needed improvement with these models.

CFD solutions provided by Peter Gnoffo and Van Norman[3] using the recent implementation of the SST model into the Laura real-gas Navier-Stokes code, were conducted on this same grid and are quite similar to the present results, also showing the heating overshoot past reattachment. Furthermore, results published by Steelant[64] and others exhibit similar heating overshoot behaviour shown in Figure 26. This similar behaviour from different codes suggests that the overshoot seen in Figure 26 is a feature of the models and not the implementation.

Figure 27 depicts the $Q-P^{0.85}$ correlation which is suggestive of better agreement in this mode of heat transfer prediction. The initial agreement of the measured wall heat transfer with the $Q-P^{0.85}$ correlation is encouraging as to the accuracy of the experiment. As with the 6 deg and the 10 deg cases, whereas the correlation suggests constant wall heating, the gradual decline in measured wall heating observed for the pressure plateau region is thought to be physically correct as it is associated with the out-of-equilibrium reattached boundary layer returning to its' natural growth response upon encountering a zero-pressure gradient environment, leading to associated gradual thickness growth and gradual decline in wall heating.

Although the $Q-P^{0.85}$ correlation provides a nearly constant heating level for the constant pressure region past reattachment, the experimentally measured wall heating having achieved its maximum value just past reattachment experiences a slight decline with progression along the peak pressure plateau region, as was seen for the 6 deg case, likely due to the boundary layer, having undergone significant compression and thinning, returning to its natural growth process for the nearly zero pressure gradient region past reattachment.

Figure 28 provides a comparison of wall shear stress experimentally obtained by two methods, that derived by oil-film technique and that derived by analysis of log-law region of pitot probe surveys, with the CFD turbulence model results. The wall-shear stress method as obtained from pitot tube survey is only applied in regions where the flow is attached, whereas the oil film method can be applied even through separation. There is disagreement between the two experimental approaches on the pressure plateau region, it is believed (by this author-who is familiar with both approaches) that the oil film may be exhibiting waves in the oil film as a consequence of the high shear stress for the viscosity of oil used for this region leading to instabilities in the oil film as seen by the scatter in the oil-film results there. Thus greater credence is given to the pitot-survey derived wall shear stress results for the peak pressure plateau region, with both techniques of equal value elsewhere. Although the Spalart-Allmaras model seem to better predict, by a slight degree, the initial boundary layer, the SST model wall shear stress results agree best with experimental results both

within the separation bubble and the peak pressure plateau region. The relative extent of the separation bubble of the several models relative to experiment as indicated by wall shear stress in this figure are as discussed for the wall pressure results of Figure 25.

The following figures present the results of a SST implementation study conducted for this fully separated case. The purpose of this study is to examine the influence that turbulence model implementation choices might have on the solutions. This is a continuation stage of the study initially done for the Mach 10 boundary layer problem in a previous section. Those implementation choices found to be unfavorable for the Mach 10 boundary layer are not further examined here as the implementation study is a process of elimination.

Figures 29, 30 and 31 explore the effect of several of the free-shear compressibility correction options on the Schulein 14 deg wall pressure, wall heating and wall shear stress results, respectively. The several free-shear compressibility correction options (CompC.1, CompC.2 and CompC.3) that had an unfavorable effect in the Mach 10 boundary layer study describe above, they will not be considered further. However, results for SST computations using the CompC.4, CompC.5 and CompC.6 options for the fully separated Schulein case are presented. The $1-F_1$ modified Sarkar correction (CompC.4 option) and the $1-F_1$ modified Zeeman correction (CompC.5 option) do provide a slight increase in extent of the separation bubble, but still underpredict. The $1-F_1$ modified Wilcox correction, however, now provides results with an overprediction of the extent of separation. It seems that some intermediate effect might be desired. None of these corrections lead to better agreement as to the underprediction of the separation bubble pressure, nor as to the lack of increase in wall heating for the separation region. The modified Sarkar and modified Zeeman do exhibit a slight decrease in the undesireable overshoot in post-reattachment wall heat transfer, whereas the modified Wilcox form provides about a more significant 10% decrease in this wall heating overshoot. Regardless the wall heating overshoot for the SST model for all the options considered still exists and warrants further work.

Next we examine further the wall boundary condition treatments, particularly the WallBC1.6 treatment. In the previous section for the Mach 10 boundary layer, the typical wall boundary condition treatment for the SST model exhibited sensitivity to the initial y_1^+ spacing, with acceptable results for $y_1^+ < 0.3$. However, wall boundary condition treatments that imposed the composite wall-sublayer/log-layer analytical expression for ω for up those cells closest to the wall up to a value of $y_1^+ \approx 6$ led to a relatively insensitive response to the initial grid spacing. In Figures 32 and 33 are the pressure and wall-heat transfer distributions for the wall boundary condition treatment study as applied to the Schulein 14 deg full separation case. Only the standard DPLR, the WallBC1=1, 5 and 6 options are considered. In Figure 32, there is but little effect amongst these various boundary condition treatments on the SST pressure distribution results throughout the entire interaction region, nor is there a perceptible effect for the upstream boundary layer. There is no change in separation bubble extent or the fact that the SST bubble pressure is underpredicted. In Figure 33, however, both wall boundary condition WallBC1.1 and WallBC1.6 are seen to reduce the undesireable overshoot in wall heating to about 1/2 of the standard SST turbulence model wall boundary condition treatment. It appears sufficient to set the ω value for initial cell off the wall to achieve this favorable result. As WallBC1.6 also leads to grid insensitivity of the Mach 10 solutions, this treatment deserves further exploration, and will be actively pursued with other flows to ensure the generality of this approach. None of the optional WallBC1 options however appear to favorably affect the severe underprediction of the separation bubble wall heating (nor the underprediction of the pressure in the separation bubble, nor the underprediction of the extent of separation).

Figure 34 demonstrates that for the SST model, the DPLR-'standard' Vorticity turbulent production form and the 'exact' strain based form of turbulent production lead to similar results in wall heating and extent of separation for this Schulein full separation case. The change in turbulent production form seems to have little effect.

Finally, Figure 35 gives both the high-density 'Seq1' and the medium-density 'Seq2' grid SST wall heating results indicating that the results of this section were nearly grid-converged.

IV.C.2. Kussoy and Horstman Mach 8.18 2D SWTBLI 10 deg *Full Separation Case*

In the 2D shock impingement experiment of Kussoy and Horstman, several wedge angles were used. For this paper we concentrate on the full separation 10 deg wedge case. For these computations a 5-block grid (4 blocks with 96x3x128 cells and 1 block of 129x3x32) was used, with initial grid spacing of $y_1^+ = 0.15$.

Figures 36 and 37 depict comparisons of wall-pressure and wall-heating variation through the interaction region for the measurements of the Mach 8.18 Kussoy and Horstman impinging SWTBLI experiment and for the several Navier-Stokes computations of the present work with the three turbulence models of SST, $K-\omega$

and of Spalart-Allmaras as implemented in the DPLR Navier-Stokes code. Additional model implementation options for compressibility correction, wall boundary condition treatment and turbulent production are also presented. The agreement between the experiment and computation as to wall pressure is excellent being within 10%, about the level of experimental uncertainty. The Spalart-Allmaras model agrees to within experimental uncertainty for wall-heating as well, although this may be due to fact that the Spalart-Allmaras model does not predict any extent of separation. The SST model (and the implementation variants shown) overpredicts peak heating by 30%, whereas the $K-\omega$ model overpredicts peak heating at 20%. Disagreement occurs as to the extent of separation, with both the SST and K-ω models underpredicting relative to the experiment. The Spalart-Allmaras model indicates that no separation occurs, whereas the experiment indicates a moderate sized separation bubble. No rise in heat transfer was detected within the separation bubble region for either the computation or the experiment. Further, the pressure level within the separation bubble differs in comparing the experiment and the SST and $K-\omega$ model results.

Also seen in Figures 36 and 37 are results for a select number of implementation options for the SST model. The change in TKE production term to the stress-based (ProdK.1) version makes little impact on the results relative to the 'standard'-DPLR approach. However, the use of the free-shear compressibility correction with the $(1-F_1)$ modified version of Wilcox (CCompC.6) increases the extent of separation so as to better agree with experiment. Regardless, no improvement in wall heating for the separation region is seen by either of these implementation options.

Table 4 captures the Uncertainty 'Discrepancy' metrics for this Kussoy full-separation case. All Tables are located in the separate 'Tables' section towards the end of the paper, just before the 'Figures' section.

IV.C.3. Murray Mach 8.9 Axisymmetric SWTBLI Cases

Murray 4.7 deg *Cowl1 Attached Case:*

Figure 38, and 39 depict the comparison of experiment with DPLR computational results for wall-pressure and wall-heating for the attached case of the nominal Mach 8.9, impinging SWTBLI experiment of Murray. Additionally, Figure 40 and 41 depict the wall-heating $Q-P^{0.85}$ correlation and wall-shear computational results for this same case. The shock generator for the attached case is an axisymmetric cowl of 4.7 deg internal angle. The computational grids made use of 5blocks with 256 cells between the axisymmetric cylinder and the shock generator. A quarter-plane grid was used for this axisymmetric flow with cells placed every 10 deg. A total of 2,580470 cells resulted. The initial grid spacing off the cylinder surface was at $y_1^+ \approx 0.01$. General agreement between computation and experiment are excellent as to pressure distribution indicating the geometry is understood and those measure taken to account for the diverging nozzle flow appear to have been successful. There is a slight overprediction of peak pressure, however it appears to be within the experimental scatter of $\pm 10\%$. There is no extended pressure plateau, likely the result of early termination of any constant pressure region in the inviscid flow above the boundary layer for this region due to the shortness of the shock generator cowl and the generation of an expansion wave at the trailing edge of the cowl leading to early termination of the interaction.

The wall shear stress results for the three turbulence models for this case are presented in Figure 41, although no shear stress measurements were conducted for this experiment. The SST and $K-\omega$ models do indicate a small amount of separation(about 3 mm), but as no indication of separation was observed in the experiment those uncertainty metrics are not carried along. The Spalart-Allmaras model does not indicate separation.

Table 5 captures the Uncertainty 'Discrepancy' metrics for this Murray attached case.

Murray 10 deg *Full Separation Case:*

Discussed in this subsection are the experimental and computational results for the fully-separated nominal Mach 8.9 impinging SWTBLI experimental case of Murray. The shock generator for the separated case is an axisymmetric cowl (Murray's Cowl2) having a 10 deg internal angle. The DPLR simulations are conducted on a 5-block grid having 512 cells across from the test cylinder to the shock generator, and 1696 cells along the length of the test cylinder. As the test surface was a cylinder and solutions were made using DPLR3D, cells were placed every 10 deg around the cylinder to describe the quarter-plane. A total of 109 processors were used for each of the solutions.

Figure 42 and 43 depict the experimental wall-pressure and heating measurement for the fully-separated case of the nominal Mach 8.9, impinging SWTBLI experiment of Murray. The wall pressure and heating DPLR computational results for the several turbulence models for this case are also shown in these figures.

For this fully-separated case of Murray, there is a slight overprediction (10%) in peak wall pressure past reattachment, and the peak heat transfer is overpredicted by approximately 25%. Overprediction of the extent of separation is given by the SST and K-Omega models, whereas Spalart-Allmaras underpredicts. As for the Kussoy and the Schulein experiments, the wall pressure in the separation bubble is too low as given by the computations. Further, although the experiment indicates a heating rise within the separation bubble, none of the turbulence models for the computations so indicate.

In Murray's PhD, he presents 1-eq turbulence model CFD computations for this case in his Fig 5.29 for which the pressure predictions are quite similar to the present, but with a much quite severe overprediction ($\approx$ 100%) of wall heating (in his Fig 5.31). Also, Murray's computations show no rise in wall heating for the separation bubble region, similar to the present computations, but in contrast to the experimental measurements.

A factor in the good to excellent agreement between the present computations and the experimental results of Kussoy and the experimental case results of Murray is that for these two experimental setups, the boundary layer develops over a long run length relative to the shock generator length, leading to a thick boundary layer relative to the spacing between the impinging shock generated at the leading edge of the shock generator and the expansion fan emanating from the trailing edge of the shock generator. As a consequence, past reattachment, the expansion fan is seen by the boundary layer leading to a reduction in overall pressure rise, mitigating the effects of the impinging shock on the boundary layer. The shock generator length to boundary layer thickness ratio for both these flows is approximately L/δ 110. Basically for a thick boundary-layer/short generator experimental impinging SWTBLI setup, the flow topology is such as to closely space the expansion fan and impinging shock. The strong pressure rise, which would otherwise be seen for such a shock generator is reduced in its intensity, well below the idealized two-shock inviscid analysis found useful for the Schulein cases, which mitigates the pressure rise past reattachment and the associated heating overshoot effects past reattachment. In contrast, the hypersonic Mach 5 impinging SWTBLI of Schulein has a thin boundary layer and a short boundary layer run length and short generator, giving a L/δ 1000. As a consequence the pressure rise through reattachment continues to reach a higher pressure and associated heating ratio, with an attendant degradation in the ability to compute heat transfer for these cases.

The two studies by Kussoy and Horstman, and that of Murray are similar to each other in that the initial boundary layer developed over a long run length leading to a thick initial boundary layer relative to the length of the shock generator with L/$\delta_0 \approx 100$, whereas for the study of Schulein the initial run length is short leading to a thin initial boundary layer relative to the length of the shock generator with a characteristic L/$\delta_0 \approx 1000$. It was found in the course of this study that the capability to accurately compute a hypersonic impinging shock is thereby affected, with quite good overall accuracy for the thick boundary layer, short generator experiments of Kussoy, et al., and of Murray, whereas the thin boundary layer, long generator experiment of Schulein is computed with greater uncertainty. In order to understand the sensitivity of the computational uncertainty to such a simple geometric parameter, we need to consider the complex flow topology of the impinging SWTBLI.

A further point with regard to the pressure plots for both Kussoy and Murray experiments is that the excellent agreement as to pressure between CFD and experiment is that is an indication that the geometry definition as given by the documentation is correctly modeled by the grids uses and the inviscid portion of the flow, which establishes the pressure field, has been correctly simulated. As noted before, it was necessary to include the information regarding the conical nozzle flow for Murray's case that was contained in the paper by Mallinson, et al. Without this additional information, e.g., an assumption of constant uniform flow for the Murray case, then the shock impingement location and the overall pressure rise will be incorrect. As this is a paper describing Uncertainty analysis of these flows, it is appropriate to point out the importance of correctly documenting the experiment and for the computor to thoroughly understand that experimental setup.

Figure 44 and 45 provide results for the $Q \approx P^{0.85}$ correlation for this case and for wall shear stress results from our CFD simulations. Observed in Figure 44 is that the correlation provides wall heat transfer comparable to the CFD results having a slightly higher level than the direct measurements. From Figure 45, the wall shear stress results facilitate identification of the extent of separation, yielding additional information useful for our process of accumulating uncertainty statistics.

Table 6 captures the Uncertainty 'Discrepancy' numerical evaluations for the full separation Murray case. All Tables are located in the separate 'Tables' section towards the end of the paper, just before the 'Figures'

section.

IV.D. Uncertainty Analysis

The statistical analysis process based on the 'Discrepancy' parameters as defined earlier and numerically tabulated for each of the cases considered (in Tables 1-6 at the end of this subsection) are presented with results summarized in Tables 7-9. What is clear from even the most cursory examination of these summary tables, is that there is both a large bias and large variance in the CFD simulations relative to experimental results for hypersonic impinging shock wave turbulent boundary layer interactions.

In a discussion on Uncertainty earlier in this paper, we introduced, for example, the Peak Pressure Discrepancy parameter, (e.g. $\Delta_{Qp} \equiv ((Q_P/Q_0)_{CFD} - (Q_P/Q_0)_{Exp})/((Q_P/Q_0)_{Exp})$), as the difference between CFD results and experimental for the given physical parameter of interest, (e.g., Peak Pressure), and for the particular experiment and CFD computation with a particular turbulence model, SST, $K-\omega$ and Spalart-Allmaras. A similar variable was defined for the other physical parameters of interest. Naturally, these Discrepancy parameters may contain error from both CFD and experiment, but it is understood that effort has been made to reduce systemic errors, and that it is Uncertainty in the form of turbulence model deficiencies that overwhelmingly predominate for these types of hypersonic SWTBLI cases.

In Tables 1 through 6, the numerical evaluations were accumulated for each experimental case for each of these 'Discrepancy' parameters for each of the several physical parameter of interest and for each turbulence model.

Using these numerical values as the raw data for a standard statistical analysis, the Uncertainty Discrepancy tables 7 through 9 were constructed, which lead to parameter means, variances and confidence intervals using Student's t-distribution and standard statistical techniques.[43] Table 7 gives the statistics for only the Peak pressure Discrepancy for all the cases, whether attached or separated. Table 8 gives the statistics specifically for the Peak pressure and Peak wall heat transfer, where only the attached cases are included in the evaluations. Table 9 gives the statistics with only the separated cases included, for the Discrepancy between CFD and experiment for the Peak pressure and wall heating, as well as for the separation bubble pressure and wall heating and the extent of separation. In all the Uncertainty tables, parameter means, variances and both the 90% and 95% confidence intervals are given.

The statistical results of these tables provide an objective measure that confirms what can be easily observed in the various plots for each of the cases considered comparing CFD and experiment. But these tables can also have a pragmatic significance in aiding a designer in setting design margins, as well. For example, using the SST model for separated cases, Table 9 indicates that the CFD results for peak heat transfer tend to be 33.5% high, but with a variance of 10.2%, which with design margins based on a 95% confidence level, then the expectation is that CFD results might overpredict peak heat transfer by as little as 17.2% or overpredict by as much as 49.8%. These results would well affect how much thermal protection mass should be used to protect surfaces. However, by Table 8, the same SST turbulence model might underpredict the peak heating by -27% or overpredict by 72.2% provided the boundary layer remains attached. Needless to say, to know what table to use would require knowledge of the extent of separation, which itself is subject to uncertainty, since according to Table 9, the SST turbulence model tends to underpredict the extent of separation by as much as -41.6% or as an overprediction of 25.9%.

Similar results can be taken from these tables for the several models, and for the other physical parameters of interest. Note that an underprediction of either peak pressure or separation bubble pressure might very well have aerodynamic significance in affecting control surface effectiveness or establishing the substructure strength needed to support external surface panels.

Overprediction of peak heating may be seen as a measure of conservativism, but the difficulty with methods that overpredict heat transfer is that if it is not known to what degree the CFD results are accurate, it may very well be best design practice to add mass in the form of extra thermal protection that a more accurate calculation would indicate was not needed.

Note that bias in a prediction can be *calibrated* and analysis results thereby corrected. But in this case the statistics arrived at for these standard turbulence models suggest that they exhibit not just bias, but considerable variance in their estimates. Bias can be calibrated out of an analysis procedure, but inconsistency of a model cannot. An attempt at calibration correction where the models are not just inaccurate, but also inconsistent, would have to be considered unreliable.

From an examination of Tables 7-9, it can be seen that at the present state of art for these turbulence models, simulations can be expected to have 95% confidence intervals with at least one bound reaching

as high as 50%. The SST and $K-\omega$ models exhibit similar statistics, with wall heating being the most problematic. Peak pressures are reasonably predicted with statistics for the SST and $K-\omega$ models signifying $\approx 10\%$ confidence interval limits. The separation pressures and wall heating are significantly underpredicted for all models, suggesting considerable work needs to be done to improve predictive capability in this area. The Spalart-Allmaras exhibits a consistent tendency to resist separation, with $\approx -100\%$ separation bubble length 'Discrepancy' statistics for the separation cases where the Spalart-Allmaras model is used.

We know, or believe that we know, from free-interaction theory and from physics-based correlations, albeit mostly obtained at lower Mach number, what the effect of trends in Mach number, Reynolds number, shock strength and levels of wall cooling should be. Good experimental design, and computational validation, should include perturbations off standard conditions so as to provide the opportunity of 'trend analysis' with variation of these separate effects around baseline conditions More complete knowledge of detailed trend behaviour, both of the simulation physics model behaviour and of the measured experiments, can provide both the modeler and the system design optimization process with the additional information that can lead to better models and better designs.

That the λ-shock separated regions are known to be highly unsteady is a factor that would be implicitly incorporated into empirical correlations, but is not factored into present-day quasi-steady simulations using RANS eddy-viscosity models, such as those used for this paper. The added uncertainty contributed by shock separated unsteadiness could well be a significant contributor to the large confidence intervals for the separation bubble statistics arrived at in this section. However, even were the correct unsteady shock-separation physics to be accurately incorporated into fully-validated DES methods, the use of such time-resolved techniques for routine production design or system optimization purposes will likely prove prohibitively expensive for some time to come.

In physical modeling of turbulence a goal should be that of consistent accuracy, that is the absence of both bias and variance. Both the presence of bias and variance are indicative to a model developer that a model is not just inaccurate but that trends based on that model may well be misleading. Likely sources of large variance seen are a lack of the turbulence models to follow trends such as the known effects of Reynolds number, Mach number and wall cooling on SWTBLI. These trends were discussed in an earlier section in connection with free-interaction theory and associated correlations. However, the simple approach taken of computing single experiments and then assessing results can be misleading in that such an approach hides the effect of these known trends on the physics of SWTBLI. Furthermore, the present approach of accumulating and evaluating statistics on the 'Discrepancy' between computations and experiment for a limited number of cases only reveals that there are hidden physics effects not appropriately accounted for in present modeling. A more sophisticated design of experiments where trends about several baseline mean conditions are explored might be more revealing of such model deficiencies, giving the model developer and design optimizer more information to meet their goals. To that end, both Schulein and Kussoy provide further cases, although with less information, and examination of those cases are worth further examination.

Clearly there is a motive to improve the turbulence models used for aerospace purposes where inaccurate analysis regarding pressure and heating lead can lead to excessive system mass, whether for thermal protection or structural support, or loss of reliable aerodynamic response, both of which can significantly degrade the potential design. The statistics presented in these tables should provide some focus on which specific areas of improvement are most needed.

IV.E. 'Nominal-Trajectory' Flight Case: Real Gas sensitivity study

To investigate the issue of what additional effects might arise in extrapolation of existing ground tests to 'Flight Cases' for scramjet application, typical flight conditions were derived from the published trajectory of Billig.[1] These conditions are given in Table 10, and compared to the test conditions of the several experimental ground tests considered in this paper. The geometric configuration is similar to that of Kussoy, but scaled up in size to account for a lengthy run in advance of the interaction. A relative flow angle of -4.5 deg of the freestream with respect to the flat test surface is assumed to account for a possible lifting cruise configuration of a scramjet powered vehicle.

The chosen Flight conditions were at Mach 7 and 14, and included both an attached (5.5 deg shock generator) and a separated case (10 deg shock generator) representing the impinging shock generated by the top surface of an inlet duct impinging on the bottom test surface of that same inlet duct. DPLR simulations were conducted using air modeled as both a perfect gas and a calorically imperfect/dissociating real gas using the Park 5-species air model. The conditions at Mach 7 are close to that of Kussoy, and we do not

pursue those further in this paper, particularly as no oxygen dissociation was observed. However, the Mach 14 separated results exhibits real-gas effects, in spite of but little dissociation of O_2, probably due to the temperatures exceeding $\approx$ 2219K where variable specific heat capacity effects for O_2 begin to be encountered.

Figures 46 and 47 provide the wall pressure and wall heat transfer distribution (X is the distance from the shock generator leading edge, and does not include the run length of the test surface preceding the shock generator). Perfect gas and real-gas simulation results for both the SST and $K-\omega$ models are given in Figures 46 and 47. SST results with frozen chemistry and variable Cp are also shown. Obviously there is no data to validate these simulations, so the purpose of these simulations is exploratory and as a limited sensitivity study. What is observed in these figures is that the $K-\omega$ model gives a larger separation extent than does the SST model, and that the real-gas simulations for both models leads to a reduction in separation extent and to an increase in peak pressure. The effect of variable Cp-frozen chemistry is to decrease separation but increase post-reattachment heating. As with the ground test experimental cases, neither of these models predict an increase in wall heat transfer for the separation bubble. The real-gas simulations results, for both of these models, also show an increase of almost 20% in peak heating past reattachment. This amount of increase in wall heating is significant.

To understand better the nature of this real-gas effect, Figures 48 and 49 depict Mach color contours with pressure line contours in white, and streamlines in red. These plots are based on the SST simulations with perfect gas and 5-species chemistry modeling of air, respectively. In both plots, the shock impinges about $X = 0.4$ meters and the inviscid regions appear quite similar. A significantly larger separation bubble (seen as the dark blue color contour region) occurs for the perfect gas simulation. Figures 50 and 51 depict similar Temperature color contours, again for the perfect gas and 5-species chemistry modeling of air, respectively. The greatest increase in flowfield temperature for each simulation occurs within the boundary layer, reaching 4438K in the vicinity of shock impingement, but only after reattachment. Figure 52 then provides color contours of the mass fraction of atomic oxygen, indicating the dissociation of molecular oxygen, O_2, into its element form. Most surprising is how little oxygen has actually undergone dissociation, with less than 0.2% mass fraction of atomic oxygen present, leading to the $\approx$ 20% increase in peak heat transfer. Further, only a quite small fraction of this atomic oxygen appears within the separation bubble, even though there is a substantial reduction in extent of separation indicated as a consequence of real-gas effects. The real-gas effect appears to be both that of air being calorically imperfect and of oxygen dissociation.

What is troubling about these 'Flight Case' results is that the severity of this simulated real-gas effect relies on the modeling of the turbulent physics in the vicinity of separation and reattachment, which are regions where these models have been demonstrated to exhibit the greatest deficiency in their performance. Further, the lack of experiments (although, see Mallinson, et al.[70] for a *laminar* high-enthalpy compression corner case) to validate these observations, even qualitatively, in that region of the flow where the physics modeling is the most uncertain, compounds the substantial uncertainty the developer of scramjet technology must account for in the design of experimental flights and when relying on CFD based analysis procedures to explore optimized designs.

V. Summary

Navier-Stokes simulations using three turbulence models, that of the SST, the $K-\omega$ and the Spalart-Allmaras were obtained for three experiments, consisting of 6 attached and separated cases total, of the hypersonic impinging shock-wave turbulent boundary-layer interactions chosen to be most relevant to NASA's future missions, including the support of development of scramjet technology. Determination of computational uncertainty for these cases was then evaluated based on definition of a uncertainty based measure indicating the difference or discrepancy between the computed results and the experiments for as many as 5 primary physical parameters that might prove of interest to either a designer or model developer, e.g.:

1.Extent of Separation (computation vs experiment),
2.Post-attachment pressure rise (computation vs experiment),
3.Post-attachment heating rise (computation vs experiment),
and if the case is separated, then also:
4.Separation bubble pressure level (computation vs experiment), and
5.Separation bubble wall heat transfer (computation vs experiment).

Statistics for these uncertainty measures were collected for each experimental case and evaluated for bias, variance and both 90% and 95% confidence intervals, with the results reported for the attached cases and for the separated cases separately.

Significant levels of bias and variance were seen in the simulations for these cases emphasizing a high level of uncertainty in the turbulence modeling for hypersonic shock-wave turbulent boundary layer interactions. Discussed was the possibility of *calibrating* the CFD analysis procedure for bias effects so as to provide a useful analytic technique for design, however, the large variance present in the uncertainty measures implies that the bias is highly inconsistent precluding reliable calibration.

Both the SST and $K-\omega$ performed similarly, but demonstrated confidence limit bounds that reach 50%. The SST model and the $K-\omega$ models tend to exhibit an overshoot in wall heating past reattachment for separated cases, with a modest tendency to underpredict the extent of separation. The separation bubble pressure and wall heat transfer levels for separated regions were underpredicted by $\approx 25-40\%$. The Spalart-Allmaras model proved to systematically resist separation.

Where the turbulent boundary layer was thin relative to a lengthy shock generator length ($L_g/\delta_0 \approx 1000$ the wall heating overshoot proved most severe, whereas a boundary layer thick relative to a short shock generator length ($L_g/\delta_0 \approx 100$ appeared to enable the shock generator trailing edge expansion fan to mitigate the severity of the interaction in the vicinity of reattachment and led to more accurate simulations.

An implementation sensitivity study (in Appendix B) provides a basis for positive outlook, however, as two approaches examined, that of an improved wall boundary condition treatment and a modified compressibility correction appear to provide improvement in the simulation of separated flows.

None of the experiments considered exhibited real-gas or dissociation effect likely to occur in flight, as there appears that no such experiments exist for both high-enthalpy and turbulent conditions likely to be encountered in flight. Simulations of an 'nominal-trajectory flight case' provided a basis for sensitivity studies of real-gas effects under potential flight conditions. Such effects were found to occur in the simulations, leading to an increase in peak heating of 20% and reduction in the extent of separation. This in spite of less than 1% dissociation of molecular oxygen into atomic oxygen for the conditions simulated. However, the CFD results for this case are uncertain in that no experimental validation exists for such effects and the effect originate in the separation region where the turbulent physics models used exhibit their greatest deficiency for the ground based experiments examined.

The high level of uncertainty observed in these simulations is believed to be free of significant error and is primarily due to turbulence model deficiencies. The impact this may have on scramjet development suggests a compelling need for high-enthalpy, real-gas experiments for impinging SWTBLI so as to complete the assessment of the sensitivity of the current methods to flows where dissociation occurs (within the boundary layer at or near the impingement location) and to reduce the current high levels of turbulence modeling uncertainty through modeling improvements.

Acknowledgments

This research was sponsered by NASA's Fundamental Aeronautics Program - Hypersonics (FAH) project. The interest, leadership and support of Dr. Deepak Bose (Associate Project Investigator, Hypersonics) is gratefully acknowledged. Technical discussions on turbulent physics and uncertainty with Joe G. Marvin and Dr. Nagi N. Mansour were most helpful. The professional skills and kind efforts of the NASA-Ames library staff, particularly that of Kathy Ponce, and Dan Pappas are much appreciated.

Appendix A. Turbulence Model equations

Spalart-Allmaras 1-eq model

The Spalart-Allmaras 1-equation turbulence model solves for an eddy-viscosity-like variable, $\hat{\nu}$, from which the eddy viscosity is then algebraically determined. Unlike the $k-\omega$ models, the standard form of the Spalart-Allmaras model does not adequately replicate the compressible log-law-of-wall region, so modifications by Catris and Aupoix must be applied. The Catris and Aupoix modified form of the Spalart-Allmaras model is given by:

$$\begin{aligned}(\partial\rho\hat{\nu}/\partial t) + (\partial\rho u_j\hat{\nu}/\partial x_j) = \quad & c_{b1}S_{sa}\rho\hat{\nu} - c_{w1}f_w\rho(\hat{\nu}/d)^2 + \sigma^{-1}\partial/\partial x_j[(\mu+\rho\hat{\nu})(\partial\hat{\nu}/\partial x_j)] \\ & +(c_{b2}\sigma^{-1})\rho(\partial\hat{\nu}/\partial x_i)(\partial\hat{\nu}/\partial x_i)\end{aligned} \tag{21}$$

with the eddy viscosity then obtained by:

$$\mu_t = \rho\hat{\nu} f_{\nu 1} \tag{22}$$

Where

$$\begin{aligned} f_{\nu 1} &= \hat{\nu}^3/(\hat{\nu}^3 + \nu c_{\nu 1}) \\ \hat{S} &= \Omega + \hat{\nu} f_{\nu 2}/(\kappa d)^2 \\ f_{\nu 2} &= 1 - \hat{\nu}/(\nu + f_{\nu 1}\hat{\nu}) \\ f_w &= g[(1 + c_{w3}^6)/(g^6 + c_{w3}^6)]^{1/6} \\ g &= r + c_{w2}(r^6 - r); \\ r &= \min(\hat{\nu}/(\hat{S}(\kappa d)^2)), 10) \\ c_{w1} &= (c_{b1}/\kappa)^2 + (1 + c_{b1})/\sigma \end{aligned} \tag{23}$$

$$\begin{aligned} c_{b1} = 0.1355; \quad c_{b2} = 0.622; \\ c_{w2} = 0.3; \quad c_{w3} = 2; \\ c_{\nu 1}; \quad \sigma = 2/3 \end{aligned} \tag{24}$$

Boundary conditions are:

$$\hat{\nu} = 0 \text{ at wall, } \hat{\nu} = 3\nu_\infty \text{ at } \infty \tag{25}$$

Menter SST/$K-\omega$ 2-equation Turbulence Model

The Shear-Stress Transport model was introduced by Menter,[5–7] incorporating concepts of Coakley and combining desirable compressible boundary layer properties of the Wilcox 1988 model with the desirable free shear layer behavior of Launder's $K-\epsilon$ model. The blending of the Wilcox 1988 $K-\omega$ model for inner boundary layer region with a $K-\omega$ transformed form of the $K-\epsilon$ equations for the outer boundary layer and free shear layer regions introduces two sets of constants along with introduction of a blending function, F_1. Also, the transformation of the high-Reynolds form of the $K-\epsilon$ equation set into the 'outer' $K-\omega$ form, led to the introduction of the extra 'cross-diffusion', $(\partial k/\partial x_j)(\partial\omega/\partial x_j)$, transport term in the ω equation and which is valid only for the 'outer' boundary layer and free shear viscous regions. In addition, two complete sets of constants were required to account for the two different regions, with interpolation using the blending function, F_1, to provide smooth variation between the two regions. F_1 is designed so as to be ≈ 1 close to the wall of a wall-bounded viscous layer, through the log-layer of the boundary layer, then reducing to ≈ 0 in the free-stream and for free-shear viscous shear flows. The resulting 'standard' form for the SST equation set is:

$$(\partial\rho K/\partial t) + (\partial\rho u_j K/\partial x_j) = \hat{P}_K - \beta^*\rho\omega K + \partial/\partial x_j[(\mu + \sigma^*\mu_t)(\partial K/\partial x_j)] \tag{26}$$

$$\begin{aligned} (\partial\rho\omega/\partial t) + (\partial\rho u_j\omega/\partial x_j) &= P_\omega - \beta\rho\omega^2 + \partial/\partial x_j[(\mu + \sigma_\omega\mu_t)(\partial\omega/\partial x_j)] \\ &\quad +2(1 - F_1)(\rho\sigma_{\omega 2}/\omega)[(\partial K/\partial x_j)(\rho\omega/\partial x_j)] \end{aligned} \tag{27}$$

With the production terms given by:

$$P_K = \tau_{ij}\partial u_i/\partial x_j = \mu_t\hat{S}^2 - (2/3)\rho K(\partial u_i/\partial x_j)\delta_{ij} \tag{28}$$

$$P_\omega = \gamma\rho P_K/\mu_t \tag{29}$$

With the traceless strain tensor "magnitude", $\hat{S}$, obtained by:

$$\hat{S}^2 = 2\hat{S}_{ij}\hat{S}_{ij}; \tag{30}$$

$$\hat{S}_{ij} = (\partial u_i/\partial x_j + \partial u_j/\partial x_i)/2 - (\partial u_l/\partial x_l)\delta ij/3 \tag{31}$$

A production limiter is applied to P_K, for the TKE equation only, such that $\hat{P}_K \leftarrow \min(P_K, 10\beta^*\rho\omega K)$.

The constitutive relation relies on an eddy viscosity defined by:

$$\mu_t = \rho K / \max(\omega, F_2 S/a_1) \tag{32}$$

Where, $\beta^* = 0.09, \kappa = 0.41, a_1 = 0.31$, and the constants for γ, β_ω, σ_ω, and σ^* used in the equations are formed by interpolation between the two sets of constants by:

$$\Phi = F_1 \Phi_1 + (1 - F_1)\Phi_2 \tag{33}$$

The two SST constant sets(inner=1, outer=2):

$$\begin{aligned} \gamma_1 &= 0.5532, \quad \beta_{\omega 1} = 0.0750, \ \sigma_{\omega 1} = 0.500, \quad \text{and } \sigma_1^* = 0.85 \\ \gamma_2 &= 0.4404, \quad \beta_{\omega 2} = 0.0828, \ \sigma_{\omega 2} = 0.856, \quad \text{and } \sigma_2^* = 1.00 \end{aligned}$$

The blending function, F_1, varies from 1.0 for the 'inner' boundary layer, to 0.0 for the 'outer' boundary layer, freestream and free shear layer regions and is constructed by:

$$\begin{aligned} F_1 &= \tanh(arg_1^4), \quad \text{where} \\ CD_{K\omega} &= \max((2\rho\sigma_{\omega 2}[(\partial K/\partial x_j)(\partial\omega/\partial x_j)]/\omega), 10^{-10}) \\ arg_1 &= \min[\max(\sqrt{k}/\beta^*\omega d, 500\mu/\rho\omega d^2), 4\rho\sigma_{\omega 2} K/CD_{K\omega} d^2] \end{aligned} \tag{34}$$

Note, d is the wall normal distance of the cell to the nearest wall. And, the constitutive blending function, F_2 is constructed by:

$$\begin{aligned} F_2 &= \tanh(arg_2^2), \quad \text{where} \\ arg_2 &= \max(2\sqrt{K}/\beta^*\omega d, 500\mu/\rho\omega d^2) \end{aligned} \tag{35}$$

Variations on the SST boundary condition and other treatments are given in Appendix B.

Wilcox-2006 $K-\omega$ 2-equation Turbulence Model

The $K-\omega$ turbulence model has undergone a long and considerable sequence of development, proving to be particularly well-suited for compressible flows. The model as developed by Wilcox,[8–10] built on the earlier work of the $K-\omega^2$ model of Saffman[75,76] and with Rubesin,[77] and is by design, better suited for compressible flows, due to its better replication of the compressible log-law-of-the-wall behaviour than the $K-\epsilon$ model. The competing $K-\epsilon$ model requires considerable correction for compressible turbulent boundary layers and also for the viscous sublayer. The latest formulation[10] incorporates the 'cross-diffusion' term, $(\partial k/\partial x_j)(\partial\omega/\partial x_j)$, of Menter, but without resorting to use of blending functions or to use of the distance to the nearest wall. Wilcox's aversion to the wall-normal distance can be traced to the fact that it is often perceived to be awkward and costly to compute accurately, but it is often used in well-established turbulence correlations. Similar to Cebeci and Smith's development of their algebraic model,[78] Wilcox has spent considerable effort to best incorporate various physics into this model, including roughness, blowing, compressibility corrections, etc.

The 'standard' form for the Wilcox-2006 $K-\omega$ equation set is:

$$(\partial\rho K/\partial t) + (\partial\rho u_j K/\partial x_j) = \hat{P}_K - \beta_K \rho\omega K + \partial/\partial x_j[(\mu + \sigma_K \rho K/\omega)(\partial K/\partial x_j)] \tag{36}$$

$$\begin{aligned} (\partial\rho\omega/\partial t) + (\partial\rho u_j\omega/\partial x_j) &= P_\omega - \beta\rho\omega^2 + \partial/\partial x_j[(\mu + \sigma_\omega\rho K/\omega)(\partial\omega/\partial x_j)] \\ &\quad + (\rho\sigma_d/\omega)[(\partial K/\partial x_j)(\rho\omega/\partial x_j)] \end{aligned} \tag{37}$$

With the production terms given by:

$$P_K = \tau_{ij}\partial u_i/\partial x_j = \mu_t \hat{S}^2 - (2/3)\rho K(\partial u_i/\partial x_j)\delta_{ij} \tag{38}$$

$$P_\omega = \alpha\omega P_K/K \tag{39}$$

A production limiter is applied to P_K, for the TKE equation only, such that $\hat{P}_K \leftarrow \min(P_K, 10\beta_K\rho\omega K)$.

The constitutive relation relies on an eddy viscosity defined by:

$$\mu_t = \rho K / \max(\omega, C_{lim} S/\sqrt{\beta_K}) \tag{40}$$

The $K-\omega$ 2006 constant set is:

$$\begin{aligned} \alpha = &\quad 0.52, &\quad C_{lim} = 7/8 \\ \beta_K = &\quad 0.09, &\quad \sigma_K = 0.60 \\ \beta_\omega = &\quad \beta_0 \cdot f_\beta, &\quad \sigma_\omega = 0.50 \\ \beta_0 = &\quad 0.0708 \end{aligned}$$

Where,

$$f_\beta = \quad (1 + 85\chi_\omega)/(1 + 100\chi_\omega) \tag{41}$$

$$\chi_\omega = \quad \mid \Omega_{ij}\Omega_{jk}\breve{\breve{S}}_{ki} \mid /(\beta_K \omega)^3 \tag{42}$$

$$\breve{\breve{S}}_{ki} = \quad S_{ki} - (\partial u_l/\partial x_l)\delta_{ki}/2 \tag{43}$$

$$\Omega_{ij} = \quad (\partial u_i/\partial x_j - \partial u_j/\partial u_i)/2 \tag{44}$$

And, finally:

$$\begin{aligned} \sigma_d = &\quad 1/8, \quad \text{for } (\partial K/\partial x_j)(\partial \omega/\partial x_j) < 0 \\ = &\quad\quad 0, \text{ otherwise} \end{aligned} \tag{45}$$

Optional variations on the boundary condition and other treatments are similar to that as for the SST model as given in Appendix B.

Appendix B. SST Turbulence Model Implementation Option-Grid Sensitivity Study

To facilitate examining turbulence model 'error' associated with the wide variety of possible implementation choices, we started with the DPLR v4.01.1 and incorporated many of the implementation options of which we were aware, allowing them to be selected by command line option. We verified the results from the modified code without command line options (or with options set equal to zero which would select the DPLR default) and compared with the unmodified DPLR v4.01.1 results to ensure that new code errors had not been introduced. We intend to apply these implementation options first to hypersonic flat plate flows (e.g., the upstream boundary layer development of the impinging SWTBLI experiments selected for this study, and for a constructed Mach 10 hypersonic cold-wall case) and then examine to determine which of these modeling choices might introduce avoidable modeling 'errors' , prior to applying the models to the impinging SWTBLI cases. If an implementation option cannot calculate the upstream boundary layer accurately, there would not seem to be much point in concerning ourselves with how that option will do with the SWTBLI itself.

Implementation Option Discussion and Definitions

The turbulence model implementation options specifically incorporated for this study, then, were:

A. Turbulent Production Terms. Many hypersonic applications involve blunt bodies with curved bow shocks. The 'exact' or 'strain-based' turbulence production term has a proven tendency to overpredict turbulent production for flow streamtubes passing through a strong curved bow shock, and further there is a tendency to overpredict turbulent production along stagnating streamlines. The preference for 'vorticity-based' production formulation arose out of those concerns, since within an attached 2D boundary layer, at least, there will be little difference between a 'vorticity-based' and a 'strain-based' formulation. Note that what is used in the 'strain-based' formulation is actually the traceless-strain magnitude, and for all production formulations the divergence term is subtracted for compressible flows, see equation above. To correct for the stagnation overproduction, Kato and Launder[79] suggested their mixed vorticity/strain based form, whereas, herein, we suggest a hybrid Vorticity/Strain form where a logical switch, F_p is defined so as

to identify viscous regions so that the 'Vorticity' formulation is used in freestream and laminar regions (to allow for sufficient production to facilitate numerical transition) and the 'strain' based formulation is used within turbulent viscous regions, whether wall-bounded or free shear. These Turbulent Production options (for the 1st term of Eq. (28)) are then given by:

iProdK = 0; 'Vorticity-based' production, where $P_{K,0} \approx \mu_t \Omega^2$
iProdK = 1; 'Strain-based' production, $P_{K,1} \approx \mu_t \hat{S}^2$
iProdK = 2; 'Kato-Launder' mixed Vorticity-Stress, $P_{K,2} \approx \mu_t \Omega \hat{S}$
iProdK = 3; Hybrid Vorticity/Stress production form, where $P_{K,3} \approx \mu_t((1-F_p)\Omega^2 + F_p \hat{S}^2)$,

In the Hybrid Vorticity/Stress production form, a logic switch is introduced designed to distinguish turbulent viscous regions whether wall-bounded or free shear (where $F_p \approx 1$) from the free-stream region (i.e. through a bow shock, etc, where $F_p \approx 0$): $F_p \equiv [F_1 + (1-F_1)/(1+\exp(12-(K/K_\infty)-(\omega/\omega_\infty)))]$.

Depending on which option (0-3) is chosen, the Turbulent Production term (Eq. (28) becomes:

$$P_K \quad = \quad P_{K,0-3} - (2/3)\rho K(\partial u_i/\partial x_j)\delta_{ij} \tag{46}$$

B. Compressibility Correction Terms. For supersonic and hypersonic free shear layers, such as compressible mixing layers, the growth rate is reduced due to high levels of turbulent Mach number, $M_t \equiv \sqrt{2K/a^2}$, . Wilcox reports on corrections to the $K-\omega$ constants for β_K and β_ω so as to suppress the eddy viscosity in compressible free shear layers as derived by several similar theories. Details are given in Wilcox,[10] but here the free shear layer compressibility correction options are given as:

iCompC =-1; do not apply
iCompC = 0; default model behaviour
iCompC = 1; Sarkar Correction
iCompC = 2: Zeeman Correction
iCompC = 3; Wilcox Correction

Experience with these free shear layer compressibility corrections are, however, that they are not necessary for attached wall boundary layers. If they are applied due to the presence in a supersonic/hypersonic application of both wall and free shear layers, it is found that the resulting suppression of eddy viscosity from these corrections lead to low eddy viscosity within the wall boundary layer, resulting in invalid solutions. Brown, however, found that by applying a simple correction to the turbulent Mach number where now $\hat{M}_t^2 = (1-F_1)\cdot M_t^2$, with F_1 being the SST blending function(which is ≈ 1 within an attached wall boundary layer, but ≈ 0 outside the wall boundary layer, is used in the compressibility correction in place of M_t, the correct behaviour for *both* free shear layers and wall boundary layer would result. The corresponding options with $\hat{M}_t$ applied become:

iCompC = 4; Sarkar/Brown
iCompC = 5; Zeeman/Brown
iCompC = 6; Wilcox/Brown

What remains to be determined -in this current study- is which form is best applied to a separated wall boundary layer, if at all.

C. Convective Term Order:

iKOrder = 2, use 2nd Order Convective term in Turb model PDE
iKOrder = otherwise: use 1st Order Convective term in Turb model PDE

D. Wall viscous sub-layer and log-layer analytical equations. In the near-wall and viscous sub-layer regions of a turbulent boundary layer, the convective and stream-wise diffusion terms of the $K-\omega$ equations become negligible, which lead to analytical solutions for both K and ω. Additionally, an analytical form for the ω term can also be derived for the equilibrium log-wall-layer, traceable to Vuong and Coakley.[30] The use of these analytical relations can be made to assure that the ω term does not drop too low due to numerical integration, or grid-related errors. Two ways to implement this analytical 'assistance' can be employed. The first is 'explicit' in that after solving the model equations, then simply overwrite ω should it drop below the analytical-derived value. The second approach is used by this author which employs the analytical expressions in the implicit setup of the diffusion terms, where, if a neighbor point ω is below the

analytical value, then the analytical value is substituted. This cures a problem observed with finely spaced grids within the viscous sublayer, where inasmuchas the ω value is dropping from 'near' infinity at the wall, an undershoot develops with increasing normal wall distance, leading to the eddy viscosity rising too rapidly for the near wall, with attendant high heating for fine grids. By accomplishing this implicitly, the near-wall development of ω is forced to nearly the analytical expression without oscillation associated with an explicit approach. Note that near-wall errors in eddy viscosity can have a disproportionate effect on wall heating, as heating is dominated by the near-wall processes. The options become:

iOmegaAn =-1: do not apply
iOmegaAn = 0: default model behaviour
iOmegaAn = 1: $\omega = 6\mu/(\beta_\omega \rho y^2)$
iOmegaAn = 2: $\omega = (6\mu/(\beta_\omega \rho y^2)) + (\sqrt{K}/((\beta^*)^{0.25}\kappa y))$

The wall values for β_ω and β^* are used.

E. Turbulence model Wall Boundary Condition Terms. The analytical value for ω tends to ∞ as the wall is approached, so a large value is often suggested for use in wall boundary conditions-if needed. Several ω-equation wall boundary condition options appear in the literature. Realizing they may not have had comparison in the open literature, we include them here as:

iWallBC0 = 0; $\omega_w = 40000\mu/(\rho y_1^2)$, DPLR default
iWallBC0 = 1; $\omega_w = 3200\mu/(\rho y_1^2)$, from Menter
iWallBC0 = 2; $\omega_w = 40000.\Omega_w$, based on Wilcox for smooth wall

Where y_1 is the "cell thickness" of the first finite-volume cell off the wall. If Wall Boundary conditions are used, then, for the K-equation, the choice is simply $K = 0$.

Note these iWallBC0 option choices will only be relevant if iWallBC1=-1.

We shall see that little difference appears in these iWallBC0 'wall boundary condition' choices, whereas certain substitute iWallBC1 'wall treatment' choices seem advantageous.

F. Wall viscous layer 'treatment' terms. In place of applying a Wall Boundary Condition term, analytical relations or near-wall correlations can be applied for the near-wall points directly within the implicit process. Note that rather than solve the turbulence model PDE equations within these innermost cells, the matrix term diagonal is set equal to one, and any off-diagonal term set to zero. Such an approach precludes the need for setting an actual Wall Boundary Condition. This option can be activated for the K and ω equations separately. The options are:

iWallBC1 = -1; do not apply, MUST choose iWallBC0 >1
iWallBC1 = 0; use default behaviour for DPLR and turbulent model
iWallBC1 = 1; use analytical expression for ω equation at 1st point off wall
iWallBC1 = 2; use analytical expression for both the K and ω equation at 1st point off wall
iWallBC1 > 2; use analytical expressions for up to $y+ = 6$, and up to $npts = 7$ off the wall, according relations described.

Note that the K equation can be analyzed for its viscous sub-layer behaviour similar to the analytical analysis of the near-wall behaviour of the ω equation, with a result of $K \approx a_k y^n$, where n lies between 3 and 4 depending on whether it is the SST or Wilcox $K-\omega$ model. The constant a_k is not determined by the near-wall analysis, however, since the value of K and its 1st-through-$(n-1)$ derivatives are zero at the wall, and we interpret this indeterminate result to mean the near-wall behaviour of K may be ill-conditioned. It would appear that this may be the source of observed grid-dependency of the $K-\omega$ models, a complication which proves repairable as will be demonstrated later in the paper. The actual physical variation of K in the viscous sub-layer is believed to be $K \approx y^2$, but it is the model equations that establish grid-dependency.

G Catris and Aupoix modification. Analysis of the several PDE based turbulence model equations for behaviour for the compressible log-law-wall region revealed that certain viscous diffusion modification resulted in better performance, particularly for the $K-\epsilon$ and Spalart-Allmaras forms. A minor correction was suggested for the $K-\omega$ form, however it is not commonly used since the $K-\omega$ form should be nearly correct:

iCatris <= -1: do not use Catris Correction
iCatris = 0: default model behaviour
iCatris >= 1: use Catris Correction

H. Eddy-Viscosity "CLIM" term. A limiter is introduced on the eddy-viscosity term, in both the Menter SST and Wilcox forms of the $K-\omega$ equation. Wilcox has fixed the value at 7/8, whereas Menter's form implies a value of one. Some authors have modified this for SWTBLI to get better agreement with separation length. Here the option is:

iCLIM = 0: use default model behaviour
iCLIM = 2, use clim=0.9 in eddy viscosity expression
iCLIM = otherwise, use clim=1.0

Note that none of these options alter how the mean Navier-Stokes equations are solved, and affect only the de-coupled $K-\omega$ PDE equations.

SST Implementation Options - Mach 10 Flat Plate Sensitivity Study:

'Nominal' $M_\infty = 10$, Cold-Wall, 2D Flat Plate Boundary Layer

The Mach 10 case Cold-Wall Flat Plate boundary layer case is used as an opportunity to examine the impact of the several turbulence models as well as specific SST model implementation options on simulations of a turbulent hypersonic cold-wall flat plate boundary layer. By doing so, the intent is not to determine which model or which is option is the *best* to implement, since here we examine only one flow, and a general purpose turbulence model needs evaluated against a wide range of flows. Rather it is a process of elimination, to determine whether any of these options should not be used.

The Mach 10 case is computed with 10 meter long 2D Flat Plate grids, of both a medium 128x3x128 and a fine 256x3x256 grid resolution. Most of the solutions were obtained on the medium grid, as little change occurred in going to fine resolution, and the purpose was implementation sensitivity studies, rather than validation. The freestream conditions were $Mach = 10$, $U = 3472.47$m/sec, $2.6587 \cdot 10^{-2} Kg/m^3$, $T_\infty = 1900$K, $T_0 = 6000$K, $T_w = 300K$ giving $ReU = 5 \cdot 10^6$. All computations were with *DPLR3D*, running in full 3D mode even for this 2D case, as this is the mode most used for NASA's mission study and support functions.

Turbulence Model y_1^+ Grid Sensitivity

Figures A.1 through A.4 show grid sensitivity studies for the four turbulence models; the Baldwin-Lomax, the Spalart-Allmaras, the SST and the $K-\omega$ model respectively. Four similar grids are used, the difference being the the spacing of the 1st grid point varies from $y_1^+ = 0.05$ to $y_1^+ = 1.5$. The grids were single-block having 128x3x128 cells each. Only the Spalart-Allmaras exhibits no y_1^+ grid sensitivity, but the heating result is considerably higher than the Baldwin-Lomax result, which is usually considered the most accurate for 'acreage' heating. The Baldwin-Lomax model has a slight y_1^+ grid sensitivity, being within $1-2\%$ over this range. Both the SST and the $K-\omega$ models exhibit considerably greater y_1^+ grid sensitivity requiring that the initial $y_1^+ < 0.3$ for the solution to be within $1-2\%$ of the final converged solution. It is for the $y_1^+ \approx 0.5$ grid that the SST model gives similar wall heating as the Baldwin-Lomax, however, with the SST model tending to be about 5% higher in wall heating than Baldwin-Lomax at the tightest y_1^+ grid spacing.

SST Turbulent Production term sensitivity

In Figure A.5, the different forms of evaluating the turbulent production are compared. The vorticity-based 'Prodk.0' option was preferentially implemented into DPLR originally, not because it is slightly easier, but rather because in going through a bow-shock of reentry vehicles, this form tends to avoid false production of turbulent kinetic energy due to numerical noise. Under certain circumstances, the stress-based 'Prodk.1' which is considered by many to be the 'exact' term, when used for streamlines passing through a strong bow-shock will induce non-physical levels of turbulence. However, for scramjet application, such a strong bow-shock will likely not be encountered, therefore may be a viable option for such applications. The other turbulent production options are designed as intermediate between these two choices. In particular, the 'Prodk.2' option is by Launder, intended to improve solutions in the vicinity of a stagnation point for the $K-\epsilon$ model. The 'Prodk.3' option is controlled by a logical switch, F_p designed to activate the stress-based option for turbulent viscous regions, regardless of whether free-shear layer or viscous wall, while retaining the vorticity-based production option for low turbulence region such as the free-stream or streamlines passing through a bow-shock. For the present hypersonic, cold-wall turbulent boundary layer all of the turbulent production options give virtually the same solution, which should be the case if all are implemented correctly.

SST Free-Shear Compressibility Correction sensitivity

It is widely accepted that free-shear layer flows grow at a slower rate for the supersonic and hypersonic regimes than for incompressible. It becomes necessary to incorporate one of three common forms of free-shear layer compressibility corrections to SST and $K-\omega$ 2-equation models. These are the Sarkar, Zeeman and Wilcox compressibility corrections which seek to account for the same effect. Unfortunately these act by reducing the turbulence levels and associated eddy viscosity, an effect which should not be applied to viscous wall layers. The option of turning the compressibility correction on or off depending on whether the flow being simulated is a free-shear layer or a viscous wall-layer is not available to more complex simulations which involve both types of flows. So it is desirable to have the ability for the free-shear layer to be controlled by a computed logical switch that would automatically turn on or off whichever of these free-shear layer correction is chosen depending on whether the region of flow is a free-shear layer or viscous wall. Note that the Wilcox compressibility correction will 'turn off' for a supersonic boundary layer up to about Mach 5, but above that all of these corrections tend to erroneously lower eddy viscosity in hypersonic turbulent boundary layers. This leads to significantly low values of computed wall heat transfer and significantly low levels of computed wall shear stress. Brown[13] showed that using the F_1 blending function already available in the SST model could act as such a computed logical switch to control as to which type of region the free-shear layer compressibility correction is applied.

In Figures A.6 and A.7 are shown the effect on a Mach 10 hypersonic cold wall boundary layer of these several versions of the free-shear layer compressibility correction when implemented into the SST turbulence model. Figure A.6 compares the wall heating for the three free-shear layer compressibility correction against the 'standard' SST demonstrating the large drop-off in wall heat transfer associated with the use of these corrections for a hypersonic viscous wall layer. In contrast, Figure A.7 shows that by incorporating the simple modification suggested by Brown, the use of any of these three free-shear layer compressibility correction, if modified, will cease to have the negative effect of incorrectly reducing hypersonic turbulent boundary layer heat transfer. Naturally, what is not addressed here is the effectiveness of the free-shear layer compressibility corrections for supersonic and hypersonic free-shear layers, as that is not a topic of this paper. Rather, as the modified compressibility corrections become for a free-shear layer as effective as the original form, the discussion of Wilcox[10] regarding the unmodified forms should be referred to. The modification, given by Brown,[13] is simply to use in the correction the F_1 modified form for the turbulent Mach number, e.g. $\hat{M}_t^2 = (1.-F_1)2\cdot(K/a^2)$. The term $(1-F_1)$ will be zero for the inner portion of a wall boundary layer, where the free-shear layer compressibility corrections should not be applied, and will equal one for free-shear layer flows, where the free-shear layer compressibility correction should be applied. We will examine in a later section, the use of these corrections, however, for separated SWTBLI since the F_1 term will be reduced for such flows.

SST Wall Boundary Condition/Treatment-grid sensitivity

Examined also were variations in wall boundary condition treatment for the SST model, as applied to the Mach 10 boundary layer case. A problem that can be experienced with the SST model has been sensitivity of wall heating results to the initial grid spacing. Typically fairly tight grid spacing with $y_1^+ < 0.3$ is recommended by most code implementors. Compared in Figure A.8 are the results for 4 different grids which differ in the initial grid spacing, $y_1^+ = 0.15$ to $y_1^+ = 1.5$, for the implementation where we have chosen the 'WallBC0=1' option, which is the standard Menter SST boundary condition acting by itself, with none of the WallBC1 options turned on. Considerable grid sensitivity is seen in these figures. The other WallBC0 options, with the WallBC1 options turned off, behave similarly.

Shown in Figure A.9 is a similar grid sensitivity study, but where the 'WallBC1=1' option is chosen. For this option, the value of ω is set for the 1st cell off the wall based on the near-wall analytical equation for ω rather than using a 'wall' value and solving the PDE for the 1st cell. The results, including the grid sensitivity is similar as for the various 'WallBC0' options where the 'wall' value is set.

Shown in Figure A.10 and A.11 are much improved grid sensitivity results, where the 'WallBC1' option is chosen such that ω for as many as 7 cells off the wall are set according to the analytical equation, up to $y^+ = 6$. Figure A.11 is for the WallBC1 option where K is set in a similar fashion according to an analytical expression. Cells located further from the wall are solved for using the $K-\omega$ PDE set. Only for initial grid points larger than 1 is grid sensitivity of heat transfer to grid spacing seen. Some further improvement could be obtained at larger y_1^+ by detailed changes in the analytical form of the ω sublayer-buffer equation, which is being actively pursued.

Additional SST implementation option sensitivity

Finally, Figure A.12 shows a comparison of wall heating for this Mach 10 case for additional SST implementation options. It is seen from this figure that where the compressibility corrections of Catris and Aupoix are applied to the SST equations (CatrisA.1) then there is minimal effect relative to the 'standard' (CompC.0 option) SST solutions as is expected. Typically, we do not run solutions with the Catris option, as the Catris modification is intended to improve compressible turbulent boundary layer solutions for the Spalart-Allmaras and $K-\epsilon$ models. Additionally, the use of a second order convective term in the $K-\omega$ equation as opposed to our usual use of 1st-order seems to raise heat transfer levels slightly, an effect not needed. Note, only the convective term is treated 1st order in our current SST implementation, all other terms are 2-order. As can be seen also, the grid-insensitive 'WallBC1.6' option gives essentially identical solution as the 'standard' or 'CompC.0' solution. The difference is the lack of grid sensitivity in the WallBC1.6 approach compared to the 'standard' treatment. The agreement is because the grid used has the tightest $y_1^+ = 0.05$ grid spacing.

References

[1]Billig, F., "Research on Supersonic Combustion," *Journal of Propulsion and Power*, Vol. 9, No. 4, 1993.

[2]Bose, D., Brown, J. L., Prabhu, D. K., Gnoffo, P. A., Johnston C. O., and Hollis, B., "Uncertainty Assessment of Hypersonic Aerothermodynamics Prediction Capability," AIAA Paper to be presented, June 27-30, Honolulu, HI, 2011.

[3]Gnoffo, P. A., Berry, S. A., and Van Norman, J. W., "Uncertainty Assessments in Simulations of 2D and Axisymmetric Hypersonic Shock Wave-Turbulent Boundary Layer Interactions at Compression Corners," AIAA Paper to be presented, June 27-30, Honolulu, HI, 2011.

[4]Wright, M. J., Candler, G. V., and Bose, D., "Data-Parallel Line Relaxation Method for the Navier-Stokes Equations," *AIAA Journal*, Vol. 36, No. 9, 1998, pp. 1603-1609.

[5]Menter, F. R., "Improved Two-Equation K-ω Turbulence Models for Aerodynamic Flows," NASA TM 103975, Oct. 1992.

[6]Menter, F. R., "Two-Equation Eddy Viscosity Turbulence Models for Engineering Applications," *AIAA Journal*, Vol. 32, No. 8, Aug 1994, pp. 1598-1605.

[7]Menter, F. R., Kuntz, M., and Langtry, R., "Ten Years of Industrial Experience with the SST Turbulence Model," *in Turbulence, Heat & Mass Transfer*, Vol 4, Ed. by Hanjalic, K., Nagano, Y., and Tummers, M., 2003, pp. 625-632.

[8]Wilcox, D. C., "Reassessment of the Scale-Determining Equation for Advanced Turbulence Models," *AIAA Journal*, Vol. 26, No. 11, Nov 1988, pp. 1299-1310.

[9]Wilcox, D. C., "*Turbulence Modeling for CFD, 2nd Ed.*," DCW Industries, Inc, 5354 Palm Drive, La Canada, CA, 1998.

[10]Wilcox, D. C., "*Turbulence Modeling for CFD, 3rd Ed.*," DCW Industries, Inc, 5354 Palm Drive, La Canada, CA, 2006.

[11]Spalart, P. R., and Allmaras, S. R., "A One-Equation Turbulence Model for Aerodynamic Flows," *Recherche Aerospatiale*, No. 1, 1994, pp. 5-21.

[12]Catris, S., and Aupoix, B., "Density Corrections for Turbulence Models," *Aerospace Science and Technology*, Vol. 4, 2000, pp. 1-11.

[13]Brown, J. L., "Turbulence Model Validation for Hypersonic Flows," AIAA Paper 2002-3308, 8th AIAA/ASME Joint Thermophysics and Heat Transfer Conference, St. Louis, Missouri, 24-26 June 2002.

[14]Ames Research Staff, "Equations, Tables, and Charts for Compressible Flow," NACA Report 1135, 1953.

[15]Chapman, D. R., Kuehn, D. M., and Larson, H. K., "Investigation of Separated Flows in Supersonic and Subsonic Streams with Emphasis on the Effect of Transition," NACA Report 1356, 1958.

[16]Kuehn, D. M., "Turbulent Boundary-Layer Separation induced by Flares on Cylinders at Zero Angle of Attack," NASA Technical Report R-117, 1961

[17]Erdos, J., and Pallone, A., "Shock-boundary layer interaction and flow separation," in: Proc. Heat Transfer and Fluid Mechanics Inst., Stanford Univ Press, 1962.

[18]Kussoy, M. I., Brown, J. D., Brown, J. L., Lockman, W. K., and Horstman, C. C., "Fluctuations and Massive Separation in Three-Dimensional Shock-Wave/Boundary Layer Interactions," Proceedings of the International Symposium on Transport Phenomena in Turbulent Flows, 2nd Ed., Univ. of Tokyo, Japan, 1988, pp. 875-887.

[19]Brown, J. L., Kussoy, M. I., and Coakley, T. J., "Turbulent Properties of Axisymmetric Shock-Wave/Boundary-Layer Interaction Flows," Turbulent Shear-Layer/Shock-Wave Interactions, Ed. by Delery, J., Springer-Verlag, Berlin, 1986, pp. 137-148.

[20]Thompson, M.J., "A Note on the Calculation of Oblique Shock-Wave Characteristics," *J. Aeron. Sci.*, V17, p774, 1950

[21]Mascitti, Vincent R., "A Closed-Form Solution to Oblique Shock-Wave Properties," *J Aircraft*, V6, N1, p 66, 1960

[22]Wolf, T., "Comment on 'Approximate Formulation of Weak Oblique Shock Wave Angle,"' *AIAA J.*, V31, pp1363, 1993

[23]Reda, D. C., Wilder, M. C., Bogdanoff, D. W., and Prabhu, D. K. "Transition Experiments on Blunt Bodies with Distributed Roughness in Hypersonic Free Flight," *Journ. Spacecraft and Rockets,* Vol 45, No. 2, March-April, 2008, pp. 210-215.

[24]Hopkins, E. J., and Inouye, M., "An Evaluation of theories for Predicting Turbulent Skin Friction and Heat Transfer on Flat Plates at Supersonic and Hypersonic Mach Numbers," *AIAA Journal,* Vol. 9, No. 6, June 1971, pp. 993-1003.

[25]Shoenherr, K. E., "Resistance of Flat Surfaces Moving Through a Fluid," *Transactions Society Naval Architects Marine Eng.,* Vol 40., pp. 279-313, 1932.

[26]Rubesin, M. W., and Inouye, M., "Forced Convection, External Flows," *Handbook of Heat Transfer,* Edited by W. M. Rohsenow and J. P.Hartnett, McGraw-Hill, New York, 1st ed., 1973, pp. 8-148.

[27]Van Driest, E. R., "The problem of aerodynamic heating," *Aeronautical Engineering Review*, Vol.15, No. 10, Oct. 1956, pp. 26-41.

[28]White, F., M., "Viscous Fluid Flow," McGraw-Hill, New York, 1st ed., 1974.

[29]Goyne, C. P., Stalker, R. J., and Paull, A., "Skin-friction measurements in high-enthalpy hypersonic boundary layers," *Journal Fluid Mechanics,* Vol 485, pp. 1-32.

[30]Vuong, S. T., and Coakley, T. J., "Modeling of Turbulence for Hypersonic Flows with and without Separation," AIAA Paper 87-0286, Reno, Nev., Jan, 1987.

[31]Coakley, T. J., "Data and Empirical Correlations for Simple Flows," GWP 18 Technology Exchange Meeting, NASA Ames, Oct 31-Nov 1, 1991.

[32]Delery, J., and Marvin, J. G., "Shock-Wave Boundary Layer Interactions," AGARDograph AG-280, NATO, Ed. by Reshotko, E., 1986.

[33]Reshotko, E., and Tucker, M., "Effect of a discontinuity on Turbulent Boundary-Layer-Thickness Parameters with Application to Shock-Induced Separation," NACA TN-3454, May 1955.

[34]Back, L. H., and Cuffel, R. F., "Changes in Heat Transfer from Turbulent Boundary Layers Interacting with Shock Waves and Expansion Waves," *AIAA Journal*, Vol. 8, No. 10, 1970, pp. 1871-1873.

[35]Holden, M. S., "Shock Wave-Turbulent Boundary Layer Interaction in High Speed Flow," ARL TR 75-0204, June 1975.

[36]Coleman, G. T, and Stollery, J. L., "Heat transfer from hypersonic turbulent flow at a wedge compression corner," *Journal of Fluid Mechanics,* Vol 56, Part 4, pp. 741-752, 1972.

[37]AIAA, "Guide for the Verification and Validation of Computational Fluid Dynamics Simulations," AIAA-G-077-19982002, AIAA, Reston, VA, May 6, 1998.

[38]Coleman, H. W., and Stern, F., "Uncertainties and CFD Code Validation," *J Fluids Eng.*, ASME, Vol. 119, Dec 1997,pp. 795-802.

[39]Roache, P. J., "Error Bars for CFD," AIAA Paper 2003-408, Jan 2003.

[40]Oberkampf, W. L., and Trucano, T. G., "Verification and Validation in computational fluid dynamics," AIAA Paper 2000-2549, June 2000.

[41]Oberkampf, W. L., and Barone, M. F., "Measures of agreement between computation and experiment: Validation metrics," *J. Comp. Physics*, Vol. 217, 2006, pp. 5-36.

[42]Oberkampf, W. L., and Roy, C. J., "Verification and Validation in Scientific Computing," Cambridge University Press, Cambridge, UK, 2010.

[43]CRC, "Handbook of Tables for Probability and Statistics, 2nd Ed.," ed. by Beyer, W. H., CRC Press, Cleveland, Ohio, 1968.

[44]StatSoft, Inc., "Electronic Statistics Textbook," Tulsa, OK: StatSoft. 2011, URL: http://www.statsoft.com/textbook/.

[45]Hill, T., and Lewicki, P., "Statistics Methods and Applications," StatSoft, Tulsa, OK. 2007.

[46]Wright, M. J., White, T., and Mangini, N., "Data Parallel Line Relaxation Code User Manual, Acadia-Version 4.01.1," NASA TM-2009-215388, Oct. 2009.

[47]Settles, G. S., and Dodson, L. J., "Hypersonic Shock/Boundary-Layer Interaction Database," NASA CR 177577, April 1991.

[48]Settles, G. S., and Dodson, L. J., "Hypersonic Turbulent Boundary-Layer and Free-Shear Layer Database," NASA CR 177610, April 1993.

[49]Settles, G. S., and Dodson, L. J., "Hypersonic Shock/Boundary-Layer Interaction Database: New and Corrected Data," NASA CR 177638, April 1994.

[50]Settles, G. S., and Dodson, L. J., "Supersonic and Hypersonic Shock/Boundary-Layer Interaction Database," *AIAA Journal*, Vol. 32, No. 7, July 1994, pp. 1377-1383.

[51]Roy, C. J. and Blottner, F. G., "Review and Assessment of Turbulence Models for Hypersonic Flows," AIAA Paper 2006-713, 2006.

[52]Knight, D., Yan, H. Y., Panaras, A. G., and Zheltovodov, A., "Advances in CFD Prediction of Shock Wave Turbulent Boundary Layer Interactions," *Progress in Aerospace Sciences,* Vol. 39, No. 2, 2003, pp. 121-184, also NATO Working Group 10, RTO-TR-AVT-007-V3

[53]Bradshaw, P., "Bibliography Of Turbulent Flows, 1980-2002," URL: http://navier.stanford.edu/bradshaw/pbref/intro.html., last updated 2007

[54]Schulein, E., Krogmann, P., and Stanewsky, E., "Documentation of Two-Dimensional Impinging Shock/Turbulent Boundary Layer Interaction Flow," DLR, German Aerospace Center, Rept. IB 223-96 A 49, Göttingen, Germany, Oct, 1996.

[55]Schulein, E., "Skin-Friction and Heat Flux Measurements in Shock/Boundary-Layer Interaction Flows," *AIAA Journal*, Vol. 44, No. 8, Aug 2006, pp. 1732-1741, also AIAA Paper 2004-2115, 2004.

[56]Tanner, L., and Blows, L., "A Study of the Motion of Oil Films on Surfaces in Air Flow, with Application to the Measurement of Skin Friction," *Journal of Physics, E: Scientific Instruments,* Vol. 8, No. 3, 1976, pp. 194-202

[57]Monson, D., "Dual-beam skin friction interferometer," U.S.Patent 4377343, Mar 22, 1983.

[58]Mateer, G. G., and Monson, D. J., and Menter, F. R., "Skin-Friction Measurements and Calculations on a Lifting Airfoil," *AIAA J.,* Vol. 34, No. 2, Feb, 1996. U.S.Patent 5963310

[59]Brown, J. L., and Naughton, J. W., The Thin Oil-Film Equation, NASA TM-1999-208767, March 1999.

[60]Brown, J. L., and Naughton, J. W., "Surface Imaging Skin Friction Instrument and Method," U.S. Patent 5,963,310, Oct. 5, 1999.

[61]Naughton, J. W., and Brown, J. L., "Uncertainty Analysis for Oil-Film Interferometry Skin-Friction Measurement Techniques," in *Fluids Engineering Division FED Fluid Measurements and Instrumentation Proceedings of the 1997 ASME Fluids Engineering Division Summer Meeting, FEDSM'97.* Part 5 (of 24), Vancouver, BC, Canada, June 1997.

[62]Naughton, J. W., and Sheplak, M. "Modern Developments in Shear Stress Measurement," *Progress in Aerospace Sciences,* Vol. 38, Issue 6-7, pp. 515-570, 2002.

[63]Fedorova, N. N., Fedorchenko, I. A., and Schülein, E., "Experimental and Numerical Study of Oblique Shock Wave/Turbulent Boundary Layer Interaction at $M = 5$," *Computational Fluid Dynamics Journal,* Vol. 10, No. 3, Special Issue, 2001, pp. 376-381.

[64]Steelant, J., "Effect of a Compressibility Correction on Different Turbulence Models," *Engineering Turbulence Modelling and Experiments* 5, ed. by Rodi, W., and Fueyo, N., Elsevier, 2002, pp. 207-216.

[65]Murray, N., "Three-Dimensional Turbulent Shock-Wave/Boundary-Layer Interactions in Hypersonic Flows," PhD. Dissertation, Imperial College, University of London, 2007.

[66]Murray, N., and Hillier, R., "Separated Shock Wave/Turbulent Boundary Layer Interactions at Hypersonic Speeds," AIAA Paper 2006-3038, June 2006.

[67]Boyce, R. R., and Hillier, R., "Shock-Induced Three-Dimensional Separation of an Axisymmetric Hypersonic Turbulent Boundary Layer," AIAA Paper 2000-2226, June 2000

[68]Elfstrom, G. M., "Turbulent hypersonic flow at a wedge-compression corner," *Journal of Fluid Mechanics,* Vol 53, Part 1, pp. 113-127, 1972.

[69]Franz, J., http://www.frantz.fi/software/g3data.php

[70]Mallinson, S. G., Gai, S. L., and Mudford, N. R., "Laminar Flows of High Enthalpy Air in a Compression Corner," 11th Australian Fluid Mechanics Conference, University of Tasmania, Hobart, Australia, 14-18 Dec, 1992.

[71]Mallinson, S. G., Hillier, R., Jackson, A. P., Kirk, D. C., Soltani, S., and Zanchetta, M., "Gun tunnel flow calibration: defining input condition for hypersonic flow computations," *Shock Waves,* Vol 10, pp. 313-322, 2000.

[72]Kussoy, M. I., and Horstman, C. C., "Documentation of Two- and Three-Dimensional Hypersonic Shock-Wave/Turbulent Boundary-Layer Interaction Flows," NASA TM 101075, Jan 1989.

[73]Kussoy, M. I., and Horstman, K. C., "Documentation of Two- and Three-Dimensional Shock-Wave/Turbulent Boundary-Layer Interaction Flows at Mach 8.2," NASA TM 103838, May 1991.

[74]Park, C., "*Nonequilibrium Hypersonic Aerothermodynamics*," John Wiley & Sons, Inc., New York, 1990.

[75]Saffman, P. G., "A Model for Inhomogeneous Turbulent Flow," *Proceedings of the Royal Society, London,* Vol. A317, 1970, pp. 417-433.

[76]Saffman, P. G., and Wilcox, D. C., "Turbulence-Model Predictions for the Turbulent Boundary Layers," *AIAA Journal,* Vol. 12, April 1974, pp. 541-546.

[77]Wilcox, D. C., and Rubesin, M. W., "Progress in Turbulence Modeling for Complex Flow Fields Including Effects of Compressibility," NASA TP-1517, April, 1980.

[78]Cebeci, T., and Smith, A. M. O., "*Analysis of Turbulent Boundary Layers*," Series in Applied Mathematics and Mechanics, Vol. XV, Academic Press, Orlando, FL, 1974.

[79]Kato, M., and Launder, B. E., "The Modeling of Turbulent Flow Around Stationary and Vibrating Square Cylinders," Proc. 9th Symposium on Turbulent Shear Flows, Kyoto, August 1993, pp. 10.4.1-10.4.6.

[80]Baldwin, B., and Lomax, H., "Thin Layer Approximation and Algebraic Model for Separated Turbulent Flows," *AIAA Paper 78-257,* 1978.

[81]Sarkar, S., Erlebacher, G., Hussain, M. Y., and Kreiss, H. O., "The Analysis and Modelling of Dilatational Terms in Compressible Turbulence," *J. Fluid Mech.* Vol. 227, pp473-493, 1991.

[82]Zeman, O., "Dilatation Dissipation: The Concept and Application in Modeling Compressible Mixing Layers," *Phys. Fluids A,* 2:2, pp 178-188, 1990.

Tables

Model	$\Delta_{InitialBL,j}$	$\Delta_{LSep,j}$	$\Delta_{PSep,j}$	$\Delta_{QSep,j}$	$\Delta_{PPeak,j}$	$\Delta_{QPeak,j}$
Expt	10%	NA	NA	NA	NA	NA
SST	10%	NA	NA	NA	−1.43%	30.20%
K-ω	10%	NA	NA	NA	−1.59%	27.54%
SA	10%	NA	NA	NA	−0.56%	34.56%

Table 1. Uncertainty Discrepancy Values for Schulein Mach 5, G6, Attached Case.

Model	$\Delta_{InitialBL,j}$	$\Delta_{LSep,j}$	$\Delta_{PSep,j}$	$\Delta_{QSep,j}$	$\Delta_{PPeak,j}$	$\Delta_{QPeak,j}$
Expt	10%	NA	NA	NA	NA	NA
SST	10%	18.42%	−7.61%	−27.17%	−0.06%	37.69%
K-ω	10%	14.47%	−20.14%	−46.39%	0.37%	41.61%
SA	10%	−100.%	−55.32%	−43.98%	−0.07%	24.56%

Table 2. Uncertainty Discrepancy Values for Schulein Mach 5, G10, Incipient Separation Case.

Model	$\Delta_{InitialBL,j}$	$\Delta_{LSep,j}$	$\Delta_{PSep,j}$	$\Delta_{QSep,j}$	$\Delta_{PPeak,j}$	$\Delta_{QPeak,j}$
Expt	10%	NA	NA	NA	NA	NA
SST	10%	−14.29%	−29.46%	−27.66%	−0.27%	44.62%
K-ω	10%	5.71%	−35.31%	−38.17%	−1.19%	28.31%
SA	10%	−28.57%	−19.11%	−6.52%	0.36%	16.05%

Table 3. Uncertainty Discrepancy Values for Schulein Mach 5, G14, Full Separation Case.

Model	$\Delta_{InitialBL,j}$	$\Delta_{LSep,j}$	$\Delta_{PSep,j}$	$\Delta_{QSep,j}$	$\Delta_{PPeak,j}$	$\Delta_{QPeak,j}$
Expt	10%	NA	NA	NA	NA	NA
SST	10%	−32.26%	−21.44%	−53.47%	−3.76%	31.01%
K-ω	10%	−53.23%	−27.01%	−19.44%	−2.21%	19.58%
SA	10%	−100.00%	−63.31%	−14.87%	−4.70%	8.74%

Table 4. Uncertainty Discrepancy Values for Kussoy Mach 8.18, G10, Full Separation Case.

Model	$\Delta_{InitialBL,j}$	$\Delta_{LSep,j}$	$\Delta_{PSep,j}$	$\Delta_{QSep,j}$	$\Delta_{PPeak,j}$	$\Delta_{QPeak,j}$
Expt	10%	NA	NA	NA	NA	NA
SST	10%	NA	NA	NA	−2.21%	−0.03%
K-ω	10%	NA	NA	NA	−2.87%	6.98%
SA	10%	NA	NA	NA	−1.26%	6.15%

Table 5. Uncertainty Discrepancy Values for Murray Mach 8.9, G4.7, Attached Case.

Model	$\Delta_{InitialBL,j}$	$\Delta_{LSep,j}$	$\Delta_{PSep,j}$	$\Delta_{QSep,j}$	$\Delta_{PPeak,j}$	$\Delta_{QPeak,j}$
Expt	10%	NA	NA	NA	NA	NA
SST	10%	−3.32%	−39.31%	−39.26%	21.52%	20.56%
K-ω	10%	13.38%	−33.95%	−44.83%	16.59%	18.54%
SA	10%	−88.86%	−79.26%	−53.43%	32.90%	39.66%

Table 6. Uncertainty Discrepancy Values for Murray Mach 8.9, G10, Full Separation Case.

Model	$\hat{\mathcal{D}}_{Pp}$	$\hat{\mathcal{D}}'_{Pp}$	90% Conf Interval $\hat{\mathcal{D}}_{Pp}$	95% Conf Interval $\hat{\mathcal{D}}_{Pp}$
SST	−1.6%	1.5%	$-3.0\% < \mu_{CFD-Exp} < -0.1\%$	$-3.4\% < \mu_{CFD-Exp} < \mathbf{0.3}\%$
KW	−1.5%	1.2%	$-2.7\% < \mu_{CFD-Exp} < -0.3\%$	$-3.0\% < \mu_{CFD-Exp} < 0.0\%$
SA	−1.3%	2.0%	$-3.2\% < \mu_{CFD-Exp} < 0.7\%$	$-3.8\% < \mu_{CFD-Exp} < 1.3\%$

Table 7. Uncertainty Analysis by Physics Parameter of Interest: Peak Pressure-All Cases.

Model	$\hat{\mathcal{D}}_{Pp}$	$\hat{\mathcal{D}}'_{Pp}$	90% Conf Interval $\hat{\mathcal{D}}_{Pp}$	95% Conf Interval $\hat{\mathcal{D}}_{Pp}$
SST	-0.50%	0.81%	$-1.86\% < \mu_{CFD-Exp} < 0.87\%$	$-2.51\% < \mu_{CFD-Exp} < \mathbf{1.51}\%$
KW	-0.41%	1.04%	$-2.16\% < \mu_{CFD-Exp} < 1.35\%$	$-2.99\% < \mu_{CFD-Exp} < 2.18\%$
SA	-0.21%	0.31%	$-0.72\% < \mu_{CFD-Exp} < 0.30\%$	$-0.97\% < \mu_{CFD-Exp} < 0.55\%$
Model	$\hat{\mathcal{D}}_{Qp}$	$\hat{\mathcal{D}}'_{Qp}$	90% Conf Interval $\hat{\mathcal{D}}_{Qp}$	95% Conf Interval $\hat{\mathcal{D}}_{Qp}$
SST	22.6%	20.0%	$-11.1\% < \mu_{CFD-Exp} < 56.3\%$	$-27.0\% < \mu_{CFD-Exp} < \mathbf{72.2}\%$
KW	25.4%	17.4%	$-4.0\% < \mu_{CFD-Exp} < 54.7\%$	$-17.9\% < \mu_{CFD-Exp} < 68.6\%$
SA	21.8%	14.4%	$-2.5\% < \mu_{CFD-Exp} < 46.1\%$	$-14.0\% < \mu_{CFD-Exp} < 57.6\%$

Table 8. Uncertainty Analysis by Physics Parameter of Interest: Attached Cases.

Model	$\hat{\mathcal{D}}_{Pp}$	$\hat{\mathcal{D}}'_{Pp}$	90% Conf Interval $\hat{\mathcal{D}}_{Pp}$	95% Conf Interval $\hat{\mathcal{D}}_{Pp}$
SST	-1.36%	2.08%	$-4.87\% < \mu_{CFD-Exp} < 2.14\%$	$-6.53\% < \mu_{CFD-Exp} < \mathbf{3.80}\%$
KW	-1.01%	1.30%	$-3.20\% < \mu_{CFD-Exp} < 1.18\%$	$-4.24\% < \mu_{CFD-Exp} < 2.22\%$
SA	-1.47%	2.81%	$-6.20\% < \mu_{CFD-Exp} < 3.26\%$	$-8.44\% < \mu_{CFD-Exp} < 5.50\%$
Model	$\hat{\mathcal{D}}_{Qp}$	$\hat{\mathcal{D}}'_{Qp}$	90% Conf Interval $\hat{\mathcal{D}}_{Qp}$	95% Conf Interval $\hat{\mathcal{D}}_{Qp}$
SST	33.5%	10.2%	$21.4\% < \mu_{CFD-Exp} < 45.5\%$	$17.2\% < \mu_{CFD-Exp} < \mathbf{49.8}\%$
KW	27.0%	10.7%	$14.5\% < \mu_{CFD-Exp} < 39.6\%$	$10.0\% < \mu_{CFD-Exp} < 44.0\%$
SA	22.3%	13.3%	$6.6\% < \mu_{CFD-Exp} < 37.9\%$	$1.1\% < \mu_{CFD-Exp} < 43.4\%$
Model	$\hat{\mathcal{D}}_{Pb}$	$\hat{\mathcal{D}}'_{Pb}$	90% Conf Interval $\hat{\mathcal{D}}_{Pb}$	95% Conf Interval $\hat{\mathcal{D}}_{Pb}$
SST	-24.5%	13.4%	$-40.2\% < \mu_{CFD-Exp} < 8.7\%$	$\mathbf{-45.8}\% < \mu_{CFD-Exp} < -3.1\%$
KW	-29.1%	7.0%	$-37.3\% < \mu_{CFD-Exp} < -20.9\%$	$-40.2\% < \mu_{CFD-Exp} < -18.0\%$
SA	-54.3%	25.5%	$-84.2\% < \mu_{CFD-Exp} < -24.3\%$	$-94.7\% < \mu_{CFD-Exp} < -13.8\%$
Model	$\hat{\mathcal{D}}_{Qb}$	$\hat{\mathcal{D}}'_{Qb}$	90% Conf Interval $\hat{\mathcal{D}}_{Qb}$	95% Conf Interval $\hat{\mathcal{D}}_{Qb}$
SST	-36.9%	12.4%	$-51.5\% < \mu_{CFD-Exp} < -22.3\%$	$\mathbf{-56.6}\% < \mu_{CFD-Exp} < -17.2\%$
KW	-37.2%	12.4%	$-51.8\% < \mu_{CFD-Exp} < -22.7\%$	$-56.9\% < \mu_{CFD-Exp} < -17.5\%$
SA	-29.7%	22.5%	$-56.2\% < \mu_{CFD-Exp} < -3.2\%$	$-65.6\% < \mu_{CFD-Exp} < 6.2\%$
Model	$\hat{\mathcal{D}}_{Ls}$	$\hat{\mathcal{D}}'_{Ls}$	90% Conf Interval $\hat{\mathcal{D}}_{Ls}$	95% Conf Interval $\hat{\mathcal{D}}_{Ls}$
SST	-7.9%	21.2%	$-32.8\% < \mu_{CFD-Exp} < 17.1\%$	$\mathbf{-41.6}\% < \mu_{CFD-Exp} < 25.9\%$
KW	-4.7%	31.9%	$-42.3\% < \mu_{CFD-Exp} < 32.9\%$	$-55.5\% < \mu_{CFD-Exp} < 46.2\%$
SA	-79.4%	34.3%	$-120.0\% < \mu_{CFD-Exp} < -39.9\%$	$-134.0\% < \mu_{CFD-Exp} < -24.8\%$

Table 9. Uncertainty Analysis by Physics Parameter of Interest: Separation Cases.

Case	Mach m/sec	β deg	$P_w : P_T$	$T_\infty : T_0$ K	ρ_∞ Kg/m^3	ReU $/m$	H_0 MJ/Kg
Schulein Att Air	5.0	6 deg	$P_T = 2.12$MPa	$T_0 = 410$	$2.0674 \cdot 10^{-2}$	$37 \cdot 10^6$	0.41
Schulein IncSep	5.0	10 deg	$P_T = 2.12$MPa	$T_0 = 410$	$2.0674 \cdot 10^{-2}$	$37 \cdot 10^6$	0.41
Schulein FullSep	5.0	14 deg	$P_T = 2.12$MPa	$T_0 = 410$	$2.0674 \cdot 10^{-2}$	$37 \cdot 10^6$	0.41
Murray Att N_2	8.9	4.7 deg	$P_T = 60$MPa	$T_0 = 1150$	-	$47.4 \cdot 10^6$	1.1
Murray Sep N_2	8.9	10 deg	$P_T = 60$MPa	$T_0 = 1150$	-	$47.4 \cdot 10^6$	1.1
Kussoy Sep Air	8.18	10 deg	$P_\infty = 430$Pa	$T_0 = 1166$	$1.87 \cdot 10^{-2}$	$7.94 \cdot 10^6$	1.17
Flight M7-Att	7.0	5.5 deg	-	$T_\infty = 220.94$	$4.401 \cdot 10^{-2}$	$23 \cdot 10^6$	2.4
Flight M7-Sep	7.0	10 deg	-	$T_\infty = 220.94$	$4.401 \cdot 10^{-2}$	$23 \cdot 10^6$	2.4
Flight M14-Att	14.0	5.5 deg	-	$T_\infty = 246.93$	$9.811 \cdot 10^{-3}$	$10 \cdot 10^6$	9.97
Flight M14-Sep	14.0	10 deg	-	$T_\infty = 246.93$	$9.811 \cdot 10^{-3}$	$10 \cdot 10^6$	9.97

Table 10. Experimental Case Nominal Condition

Figures

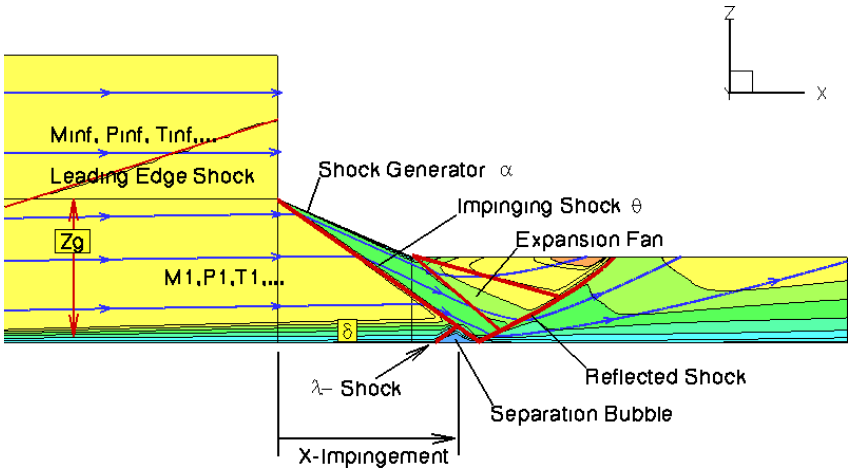

Figure 1. Impinging Shock-Wave/Boundary-Layer Flow Topology.

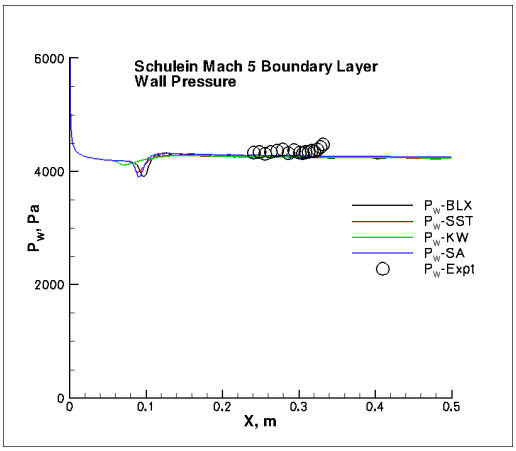

Figure 2. Schulein $M_\infty = 5$ 2D Flat Plate, Wall Pressure vs X.

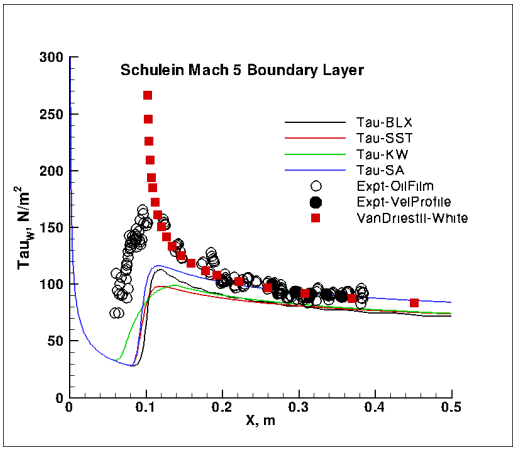

Figure 3. Schulein $M_\infty = 5$ 2D Flat Plate, Wall Shear Stress vs X.

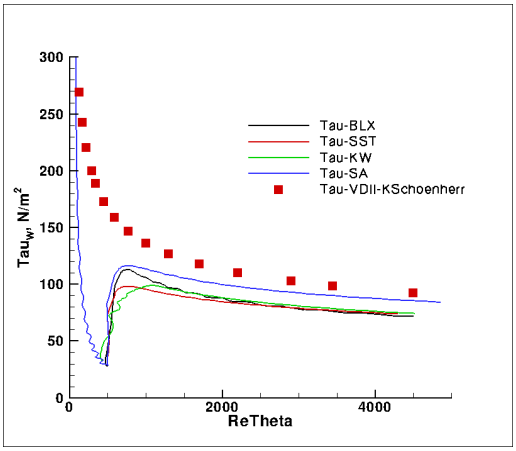

Figure 4. Schulein $M_\infty = 5$ 2D Flat Plate, Wall Shear Stress vs ReTheta.

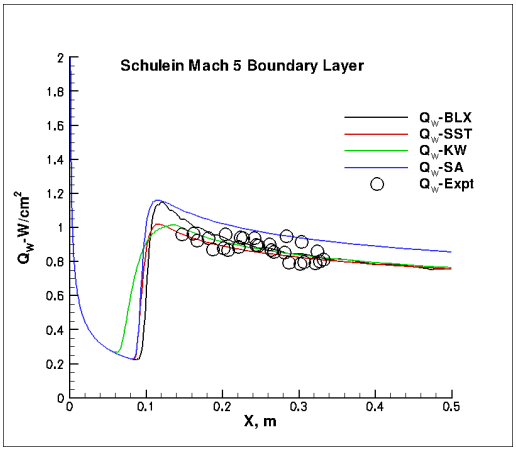

Figure 5. Schulein $M_\infty = 5$ 2D Flat Plate, Wall Heat Transfer vs X.

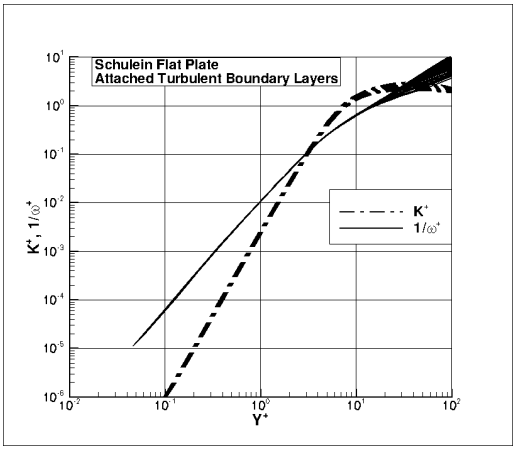

Figure 6. Schulein $M_\infty = 5$ 2D Flat Plate, SST Model-Attached Turbulent Boundary Layer Normalized $K - \omega$ Profiles.

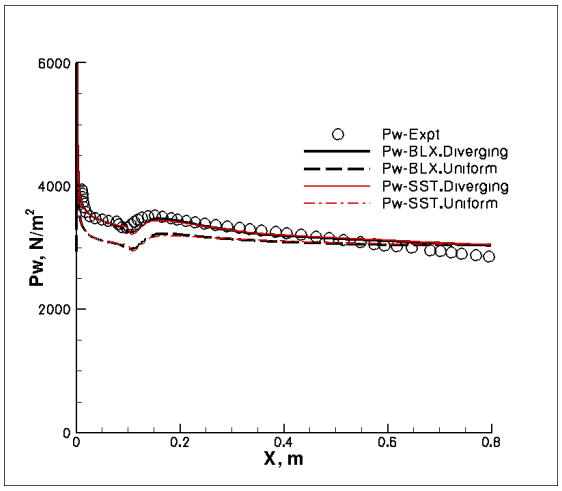

Figure 7. Murray (Mallinson) $M_\infty = 8.9$ Axisymmetric Cylinder, Wall Pressure vs X.

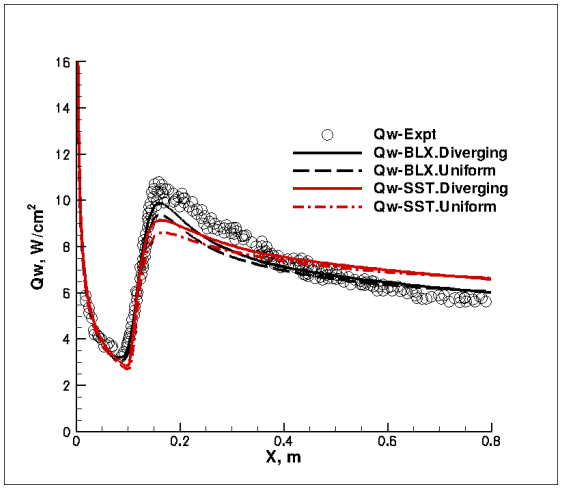

Figure 8. Murray (Mallinson) $M_\infty = 8.9$ Axisymmetric Cylinder, Wall Heat Transfer vs X.

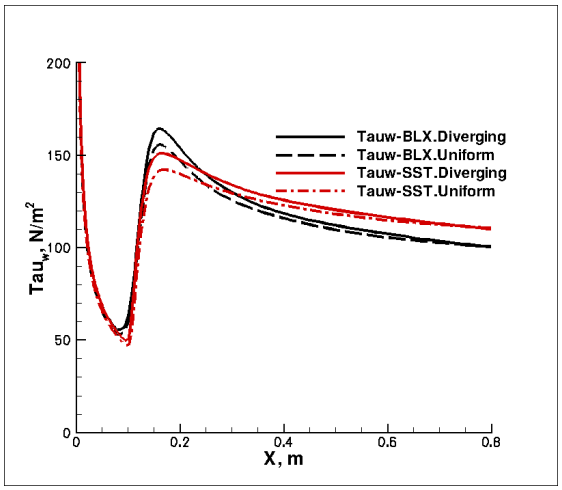

Figure 9. Murray (Mallinson) $M_\infty = 8.9$ Axisymmetric Cylinder, Wall Shear Stress vs X.

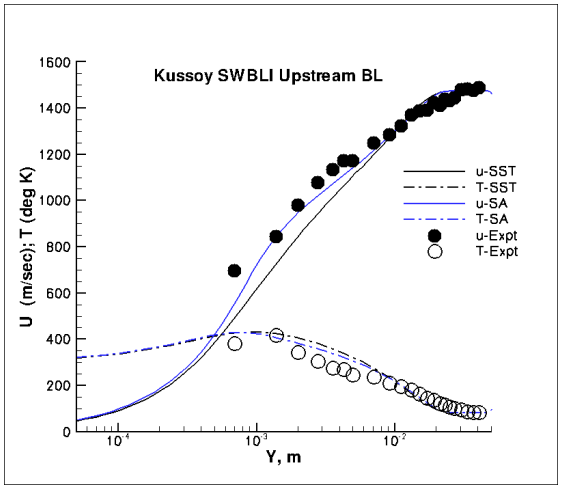

Figure 10. Kussoy-Horstman $M_\infty = 8.18$ Upstream Boundary Layer Profile.

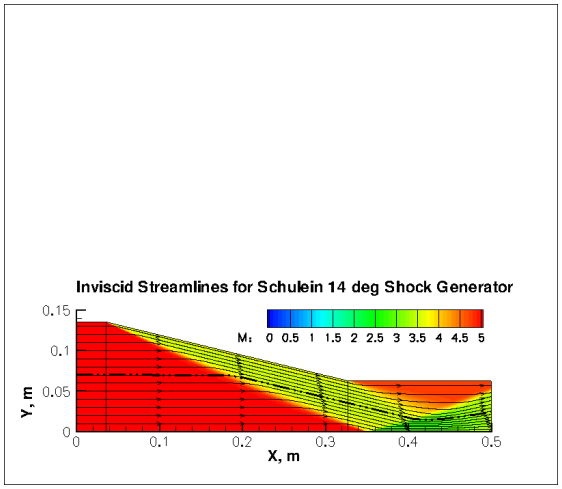

Figure 11. Schulein G14 Shock Generator, Inviscid Flow-Streamlines, Grid sensitivity study.

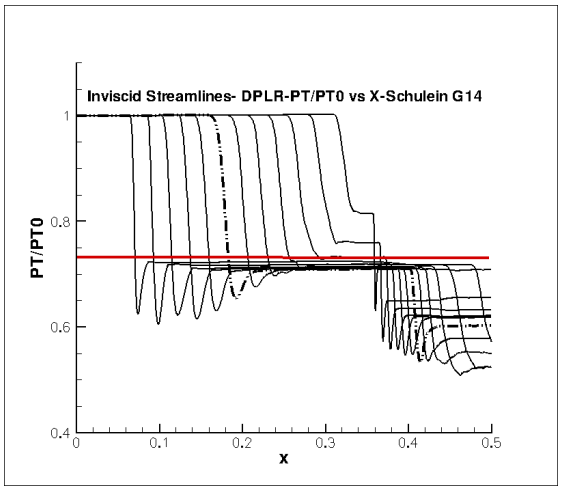

Figure 12. Schulein G14 Shock Generator, Inviscid Flow-PTotal/Grid sensitivity study. 'Coarse' Grid.

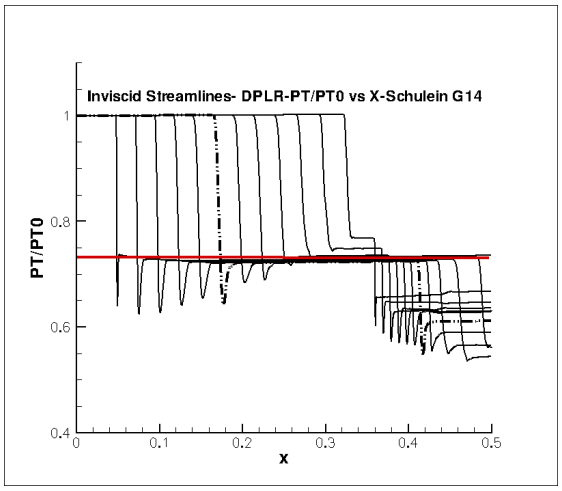

Figure 13. Schulein G14 Shock Generator, Inviscid Flow-PTotal/Grid sensitivity study. 'Medium' Grid.

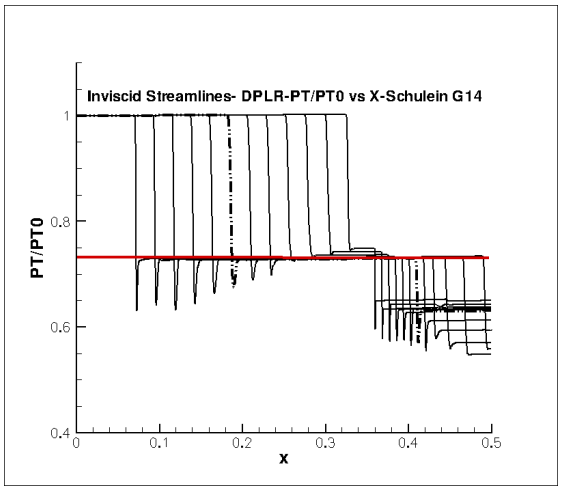

Figure 14. Schulein G14 Shock Generator, Inviscid Flow-PTotal/Grid sensitivity study. 'Fine' Grid.

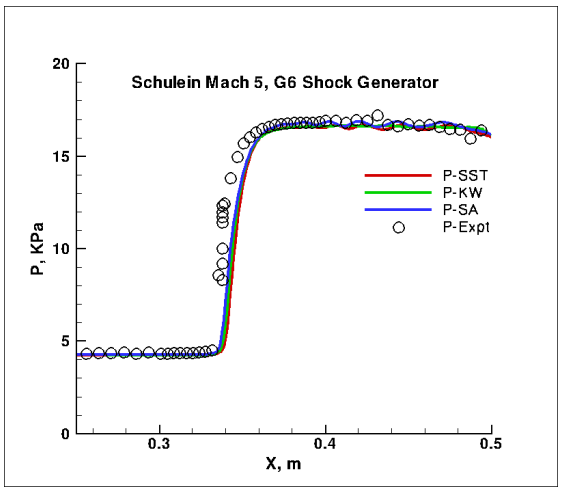

Figure 15. Schulein Mach 5, 6 deg Shock Generator, Attached Case, Pwall vs X surface distribution.

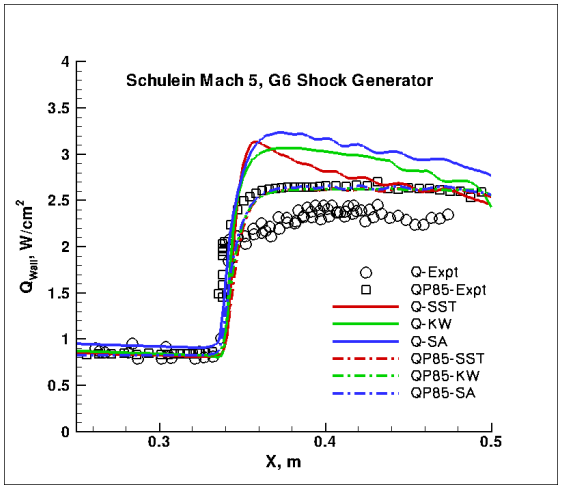

Figure 16. Schulein Mach 5, 6 deg Shock Generator, Attached Case, Qwall vs X surface distribution.

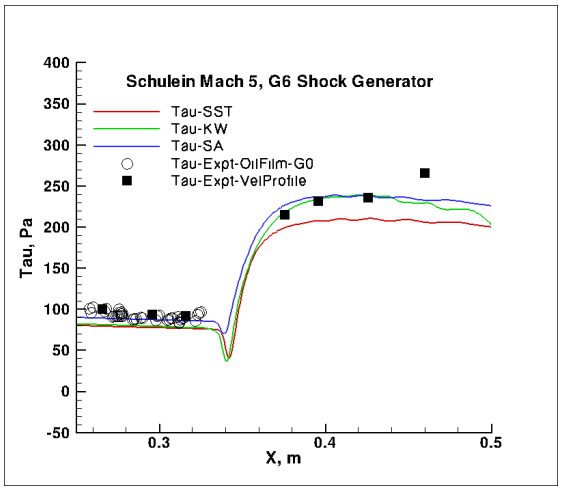

Figure 17. Schulein Mach 5, 6 deg Shock Generator, Attached Case, Wall Shear Stress vs X surface distribution.

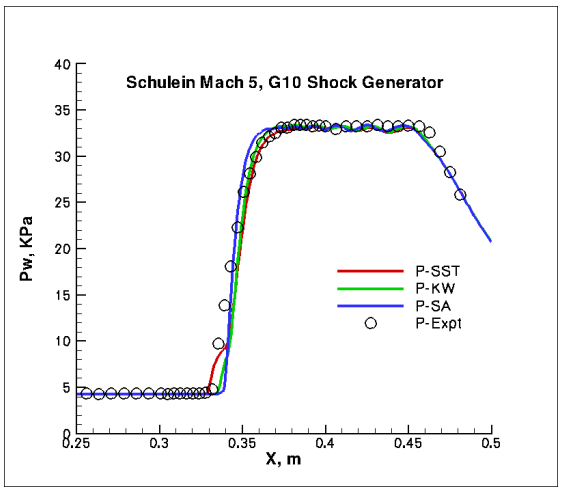

Figure 18. Schulein Mach 5, 10 deg Shock Generator, Incipient Separation Case, Pwall vs X surface distribution.

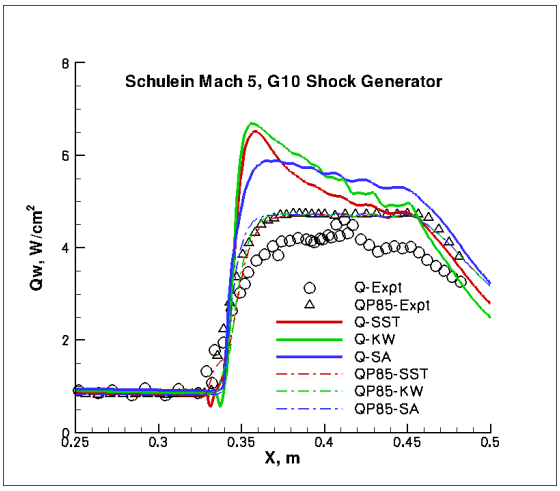

Figure 19. Schulein Mach 5, 10 deg Shock Generator, Incipient Separation Case, Qwall vs X surface distribution.

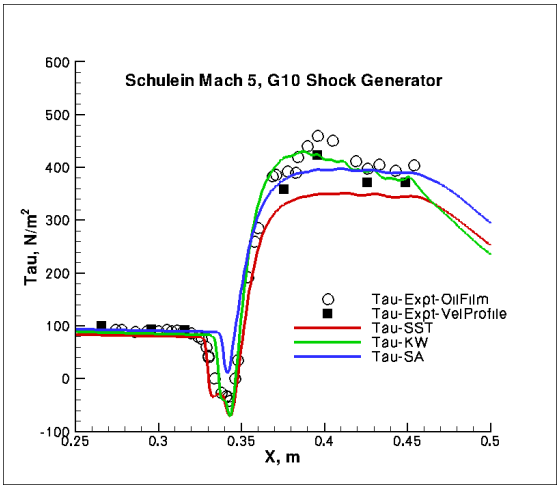

Figure 20. Schulein Mach 5, 10 deg Shock Generator, Incipient Separation Case, Wall Shear Stress vs X surface distribution.

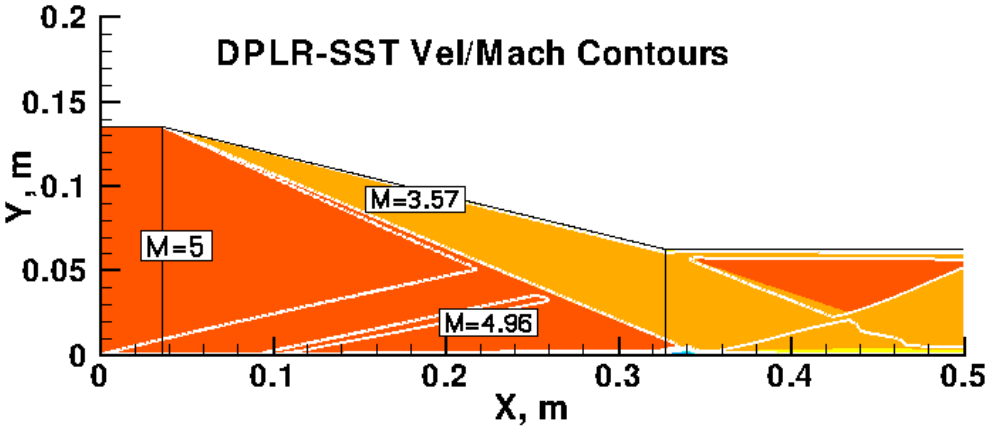

Figure 21. Schulein Mach 5, 14 deg Shock Generator, Full Separation Case, Velocity Color Contours, Pressure Line Contours, Full Computational Domain.

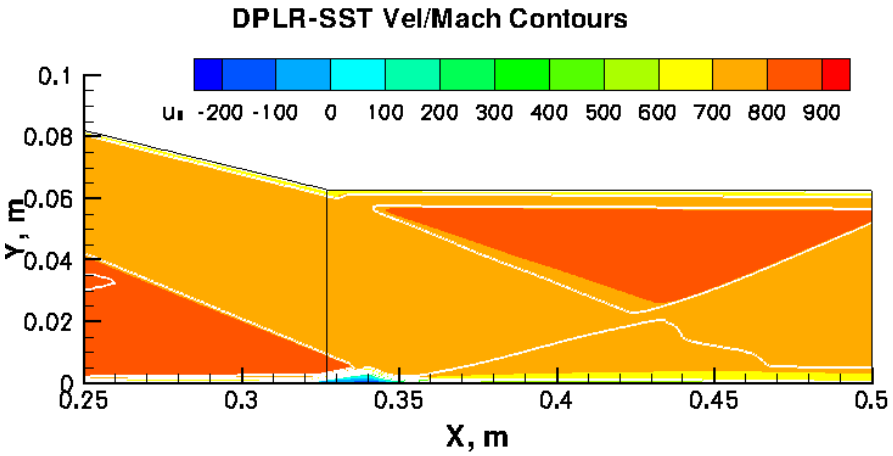

Figure 22. Schulein Mach 5, 14 deg Shock Generator, Full Separation Case, Velocity Color Contours, Pressure Line Contours, Separation Region.

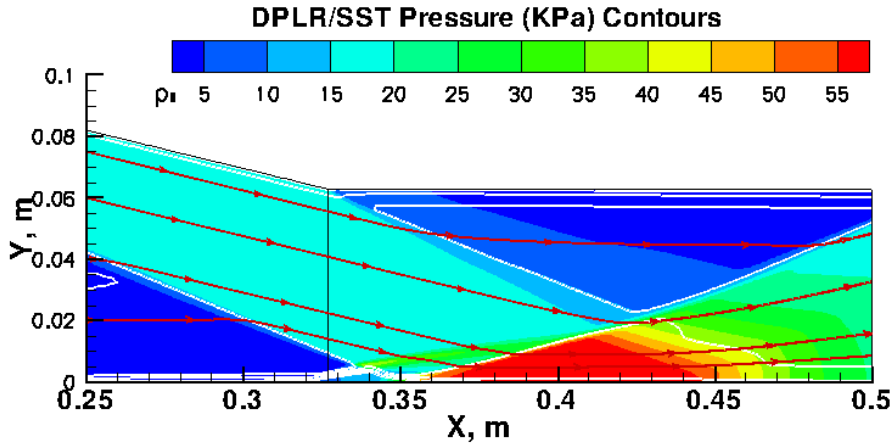

Figure 23. Schulein Mach 5, 14 deg Shock Generator, Full Separation Case, Pressure Contours, Separation Region.

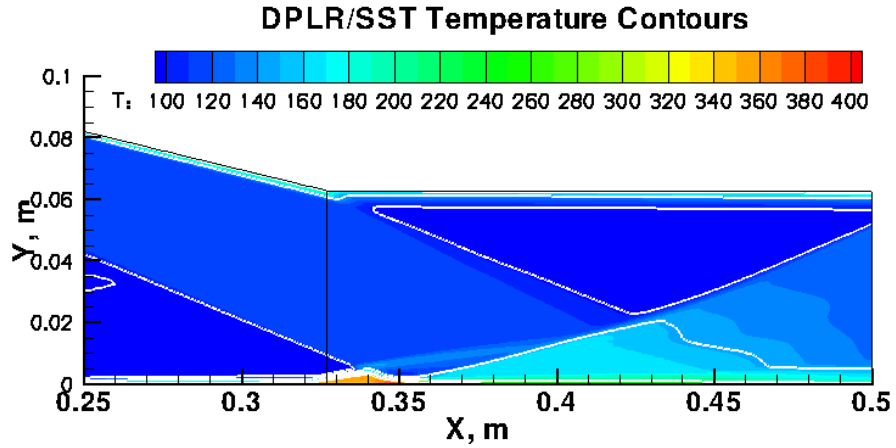

Figure 24. Schulein Mach 5, 14 deg Shock Generator, Full Separation Case, Temperature Color Contours, Pressure Line Contours, Separation Region.

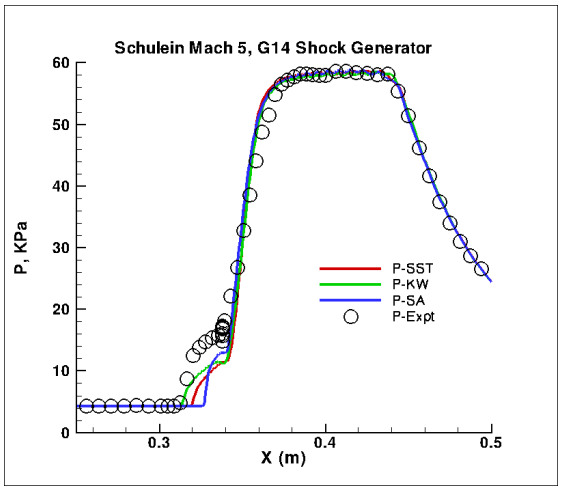

Figure 25. Schulein Mach 5, 14 deg Shock Generator, Full Separation Case, Pwall vs X surface distribution.

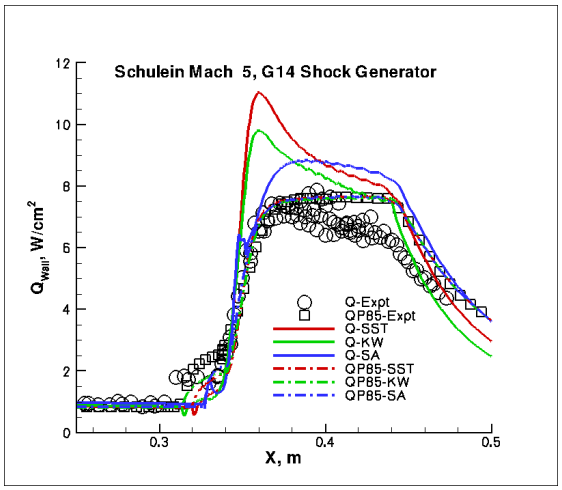

Figure 26. Schulein Mach 5, 14 deg Shock Generator, Full Separation Case, Qwall vs X surface distribution.

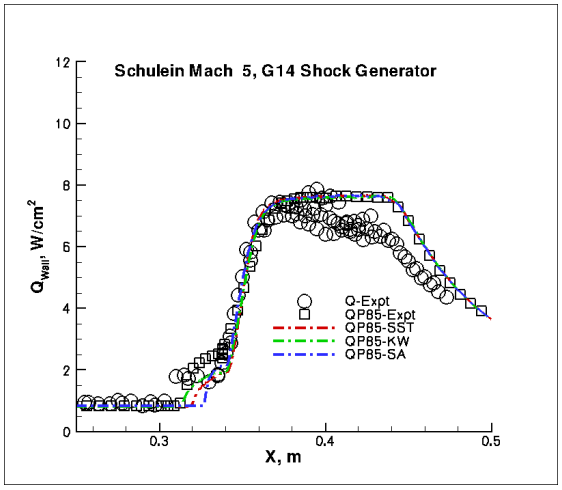

Figure 27. Schulein Mach 5, 14 deg Shock Generator, Full Separation Case, Qwall $\approx P^{0.85}$ Correlation vs X surface distribution.

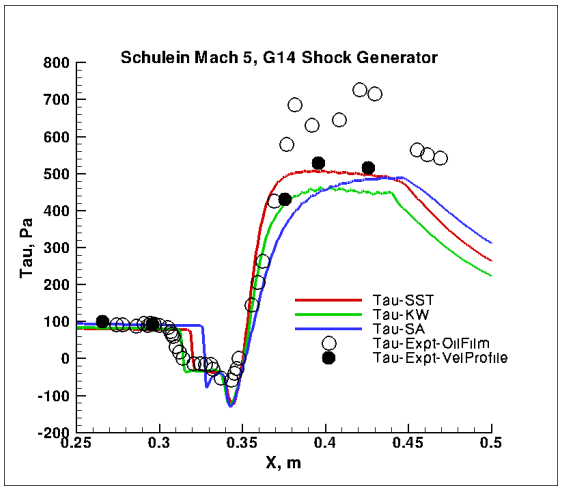

Figure 28. Schulein Mach 5, 14 deg Shock Generator, Full Separation Case, Wall Shear Stress vs X surface distribution.

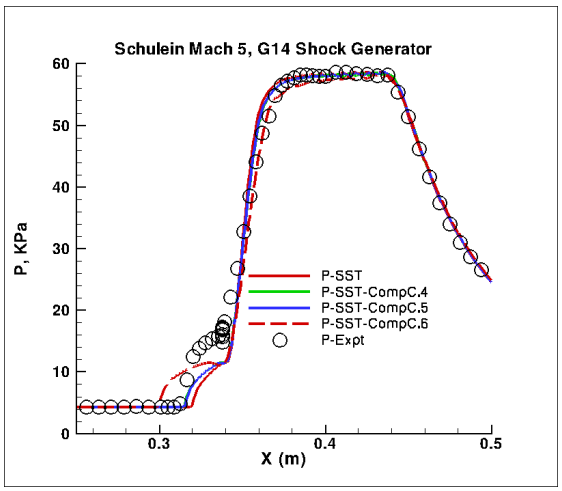

Figure 29. Schulein Mach 5, 14 deg Shock Generator, Full Separation Case, Compressibility Correction Study, Pwall vs X surface distribution.

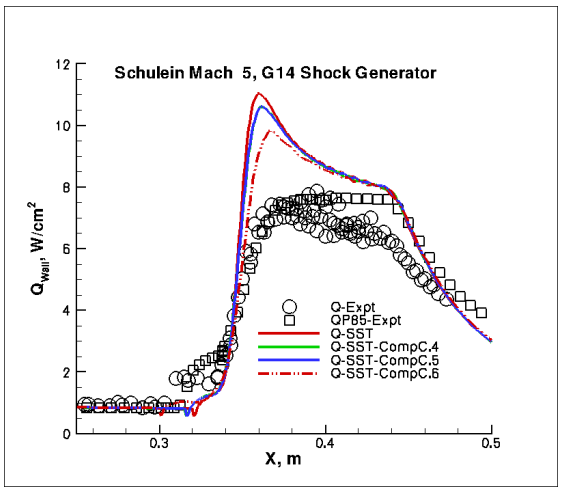

Figure 30. Schulein Mach 5, 14 deg Shock Generator, Full Separation Case, Compressibility Correction Study, Qwall vs X surface distribution.

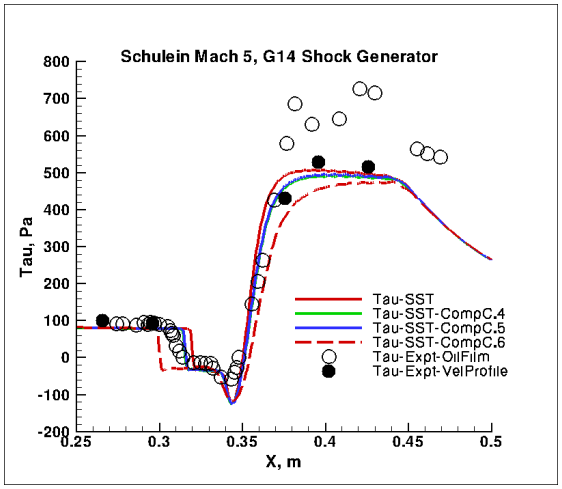

Figure 31. Schulein Mach 5, 14 deg Shock Generator, Full Separation Case, Compressibility Correction Study, wall Shear Stress vs X surface distribution.

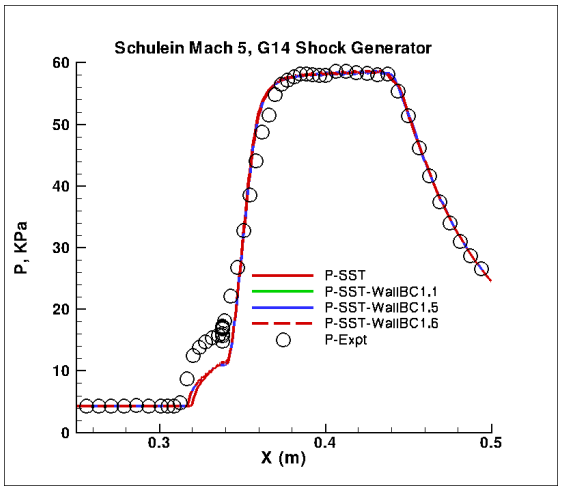

Figure 32. Schulein Mach 5, 14 deg Shock Generator, Full Separation Case, Wall Boundary Condition Study, Pwall vs X surface distribution.

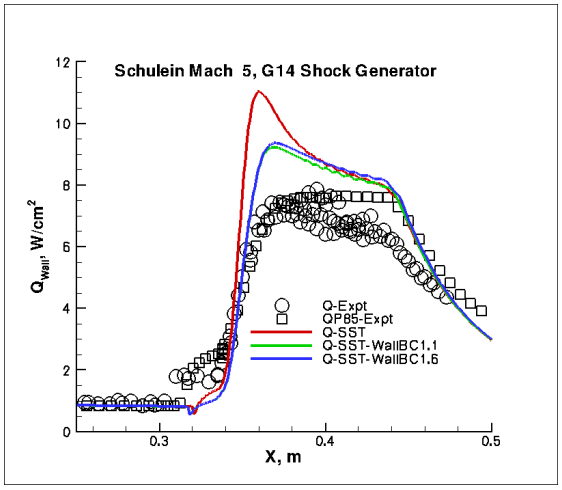

Figure 33. Schulein Mach 5, 14 deg Shock Generator, Full Separation Case, Wall Boundary Condition Study, Qwall vs X surface distribution.

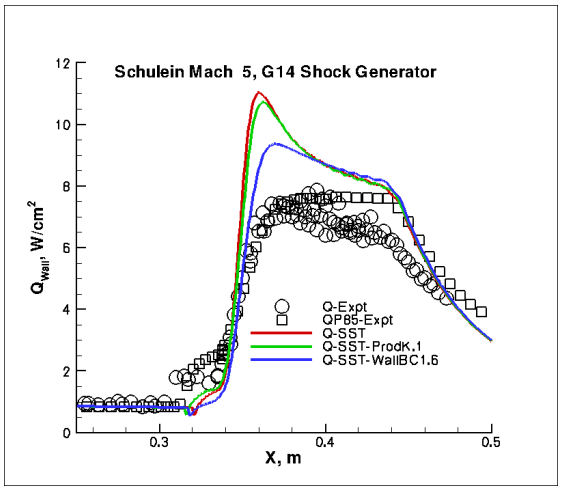

Figure 34. Schulein Mach 5, 14 deg Shock Generator, Full Separation Case, Implementation Study, Qwall vs X surface distribution.

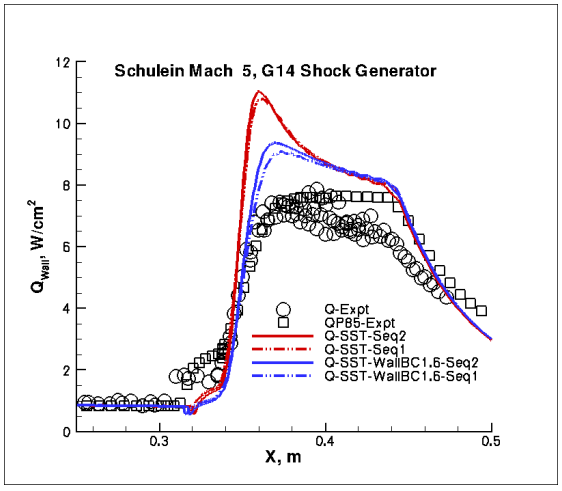

Figure 35. Schulein Mach 5, 14 deg Shock Generator, Full Separation Case, Qwall vs X surface distribution.

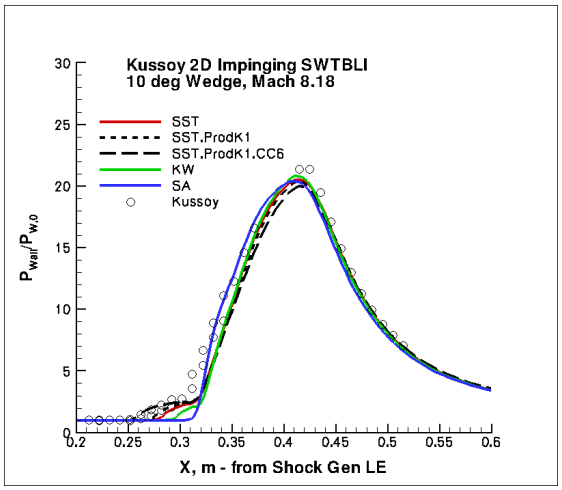

Figure 36. Kussoy 10 deg 2D Shock Generator, Separated Case, Pwall vs X surface distribution.

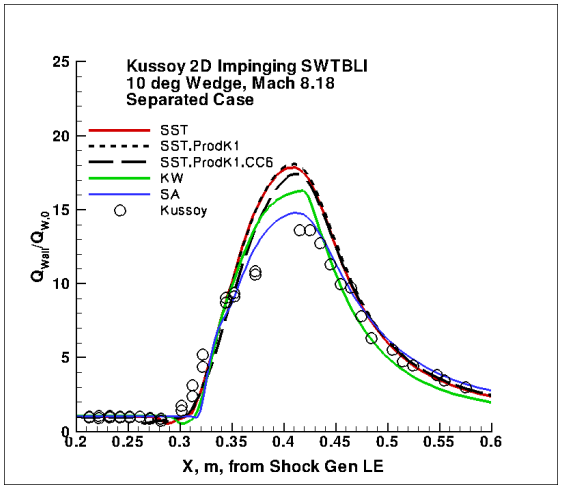

Figure 37. Kussoy 10 deg 2D Shock Generator, Separated Case, Qwall vs X surface distribution.

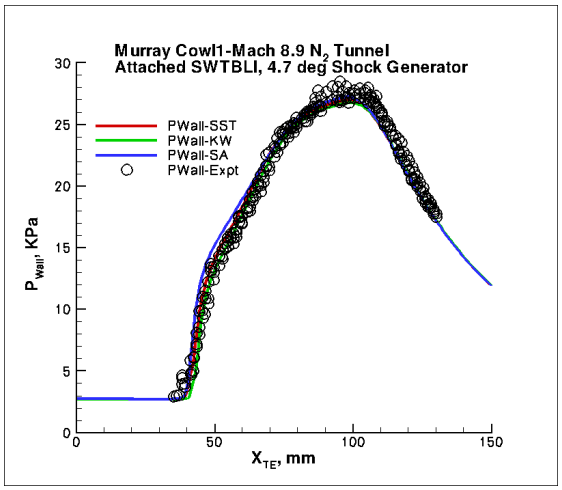

Figure 38. Murray 4.7 deg Cowl1 Shock Generator, Attached Case, Pwall vs X surface distribution.

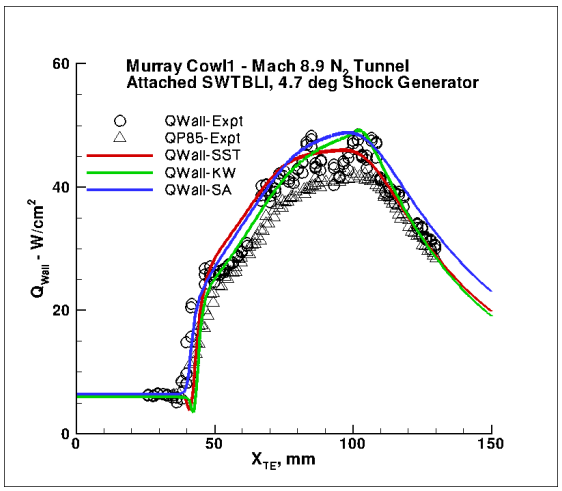

Figure 39. Murray 4.7 deg Cowl1 Shock Generator, Attached Case, Qwall vs X surface distribution.

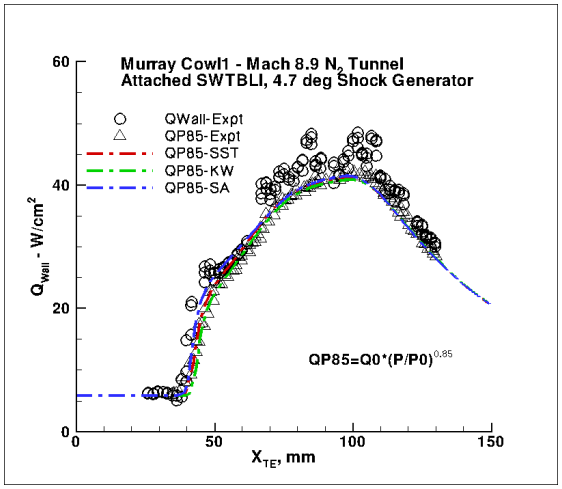

Figure 40. Murray 4.7 deg Cowl1 Shock Generator, Attached Case, Qwall-$P^{0.85}$ Correlation vs X surface distribution.

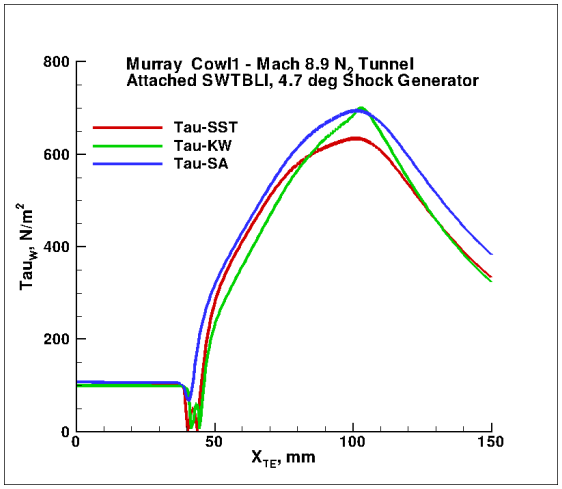

Figure 41. Murray 4.7 deg Cowl1 Shock Generator, Attached Case, Wall Shear Stress vs X surface distribution.

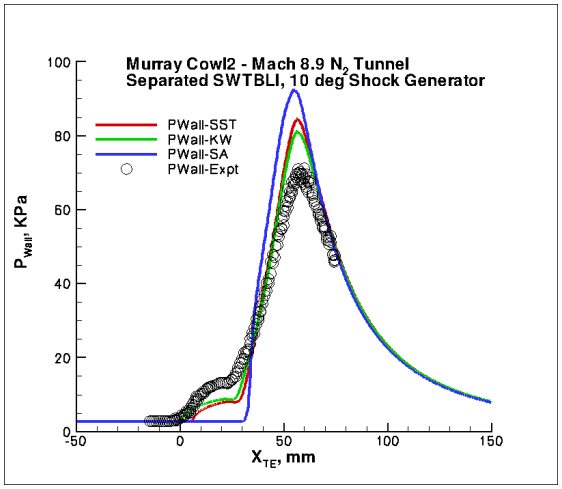

Figure 42. Murray 10 deg Cowl2 Shock Generator, Separated Case, Pwall vs X surface distribution.

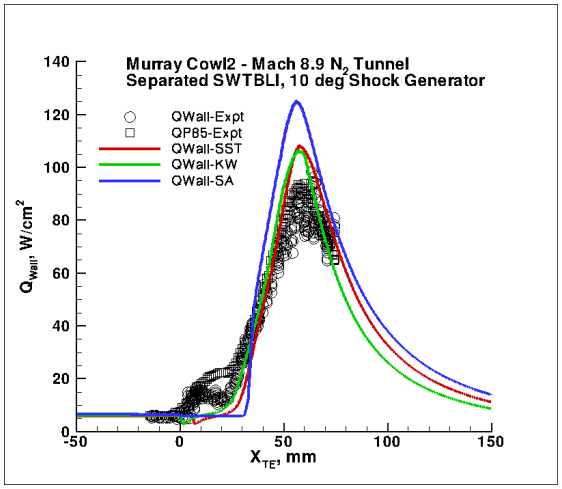

Figure 43. Murray 10 deg Cowl2 Shock Generator, Separated Case, Qwall vs X surface distribution.

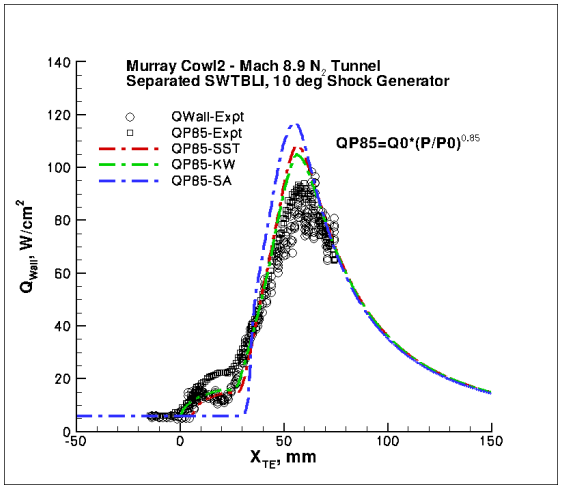

Figure 44. Murray 10 deg Cowl2 Shock Generator, Separated Case, Qwall-$P^{0.85}$ Correlation vs X surface distribution.

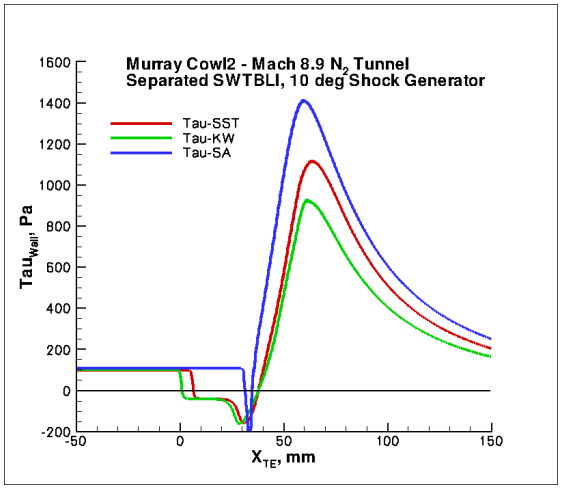

Figure 45. Murray 10 deg Cowl2 Shock Generator, Separated Case, Wall Shear Stress vs X surface distribution.

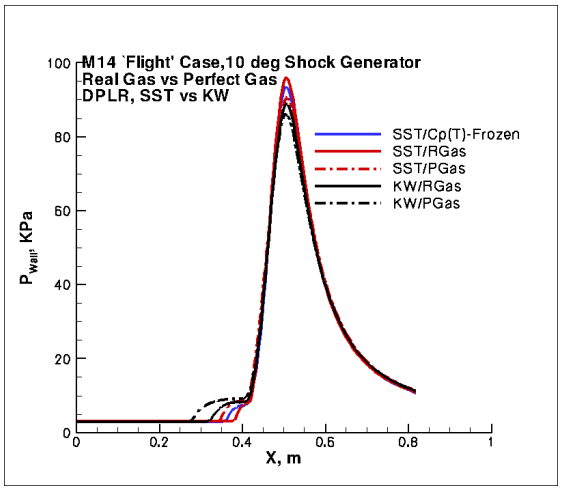

Figure 46. Flight Case Mach 14, 10 deg Shock Generator, Separated Case, Pressure distribution comparison for SST vs $K-\omega$, Real-Gas vs Perfect-Gas.

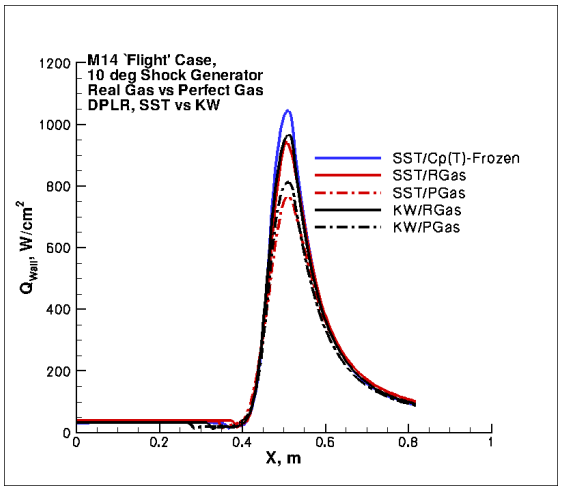

Figure 47. Flight Case Mach 14, 10 deg Shock Generator, Separated Case, Wall Heat Transfer distribution comparison for SST vs $K-\omega$, Real-Gas vs Perfect-Gas.

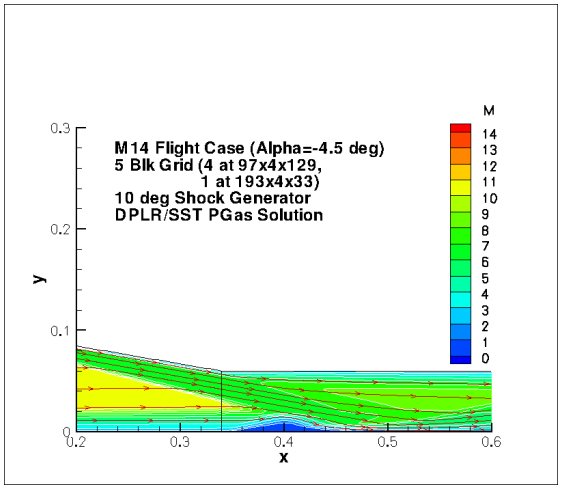

Figure 48. Flight Case Mach 14, 10 deg Shock Generator, SST Perfect Gas Separated Case, Mach color contours w/ Pressure line contours.

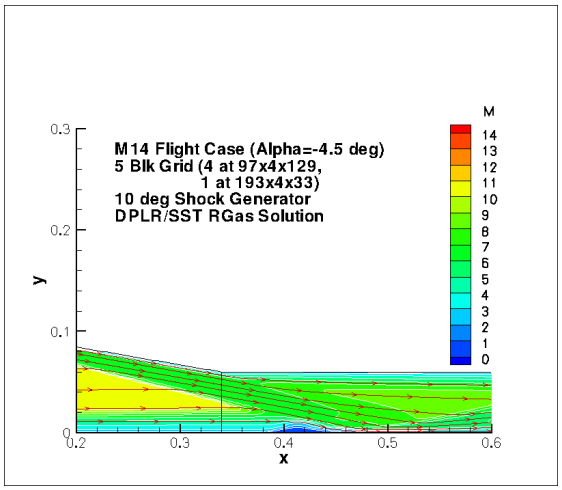

Figure 49. Flight Case Mach 14, 10 deg Shock Generator, SST Real Gas Separated Case, Mach color contours w/ Pressure line contours.

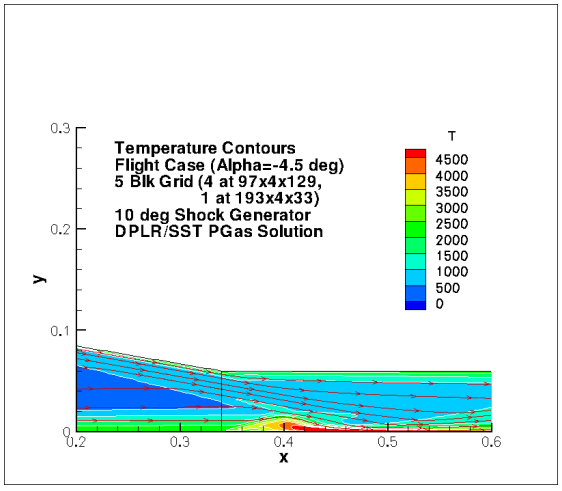

Figure 50. Flight Case Mach 14, 10 deg Shock Generator, SST Perfect Gas Separated Case, Temperature color contours w/ Pressure line contours.

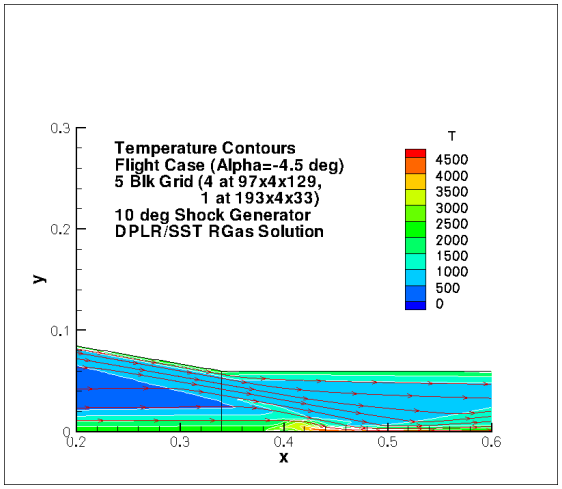

Figure 51. Flight Case Mach 14, 10 deg Shock Generator, SST Real Gas Separated Case, Temperature color contours w/ Pressure line contours.

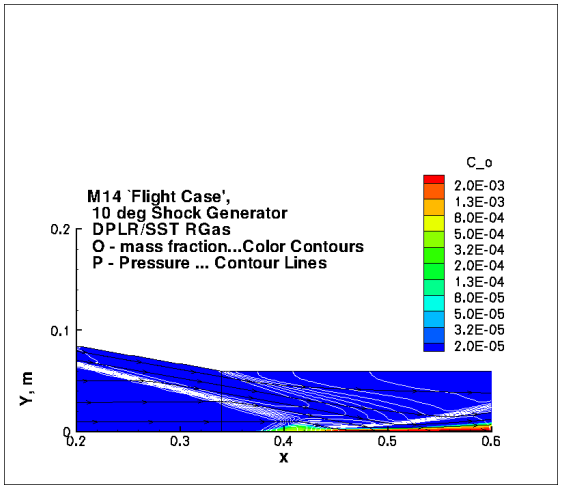

Figure 52. Flight Case Mach 14, 10 deg Shock Generator, SST Real Gas Separated Case, Dissociated Oxygen-color contours w/ Pressure line contours.

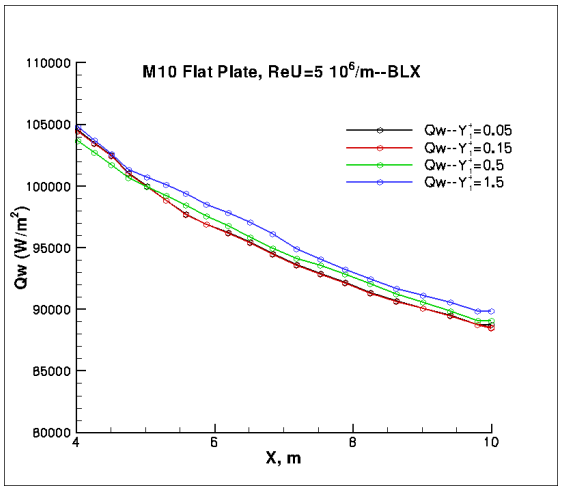

Figure 53. Mach 10 Flat Plate Grid Sensitivity Study, Baldwin-LomaxTurbulence model. Cold-Wall, $T_w/T_0 = 1/3$.

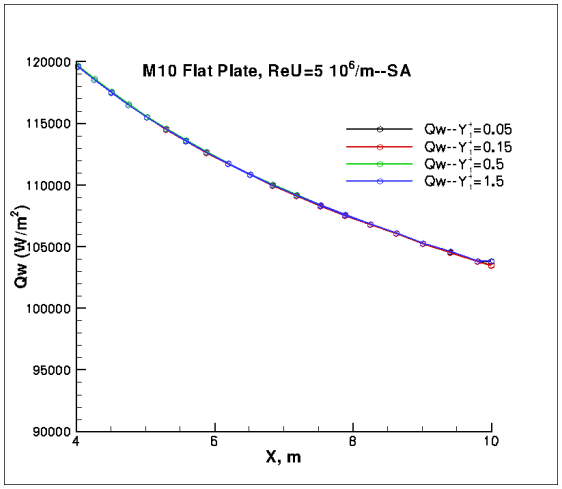

Figure 54. Mach 10 Flat Plate Grid Sensitivity Study, Spalart-Allmaras Turbulence model. Cold-Wall, $T_w/T_0 = 1/3$.

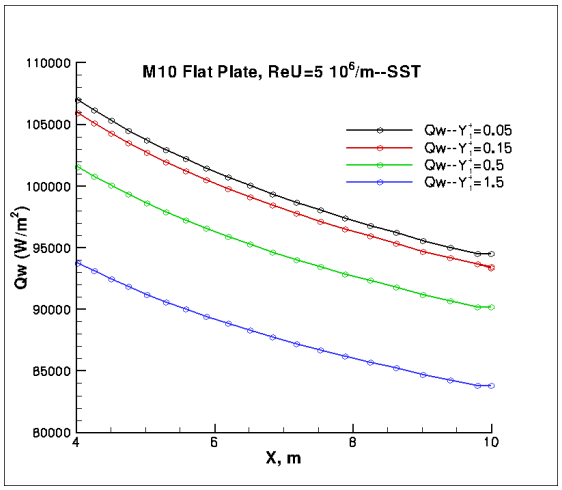

Figure 55. Mach 10 Flat Plate Grid Sensitivity Study, SST Turbulence model. Cold-Wall, $T_w/T_0 = 1/3$.

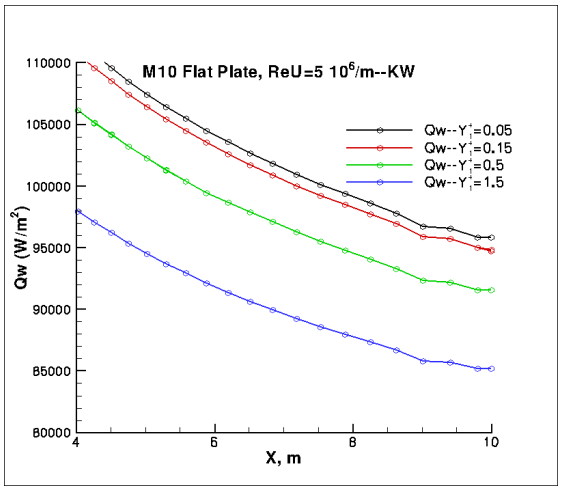

Figure 56. Mach 10 Flat Plate Grid Sensitivity Study, $K-\omega$ Turbulence model. Cold-Wall, $T_w/T_0 = 1/3$.

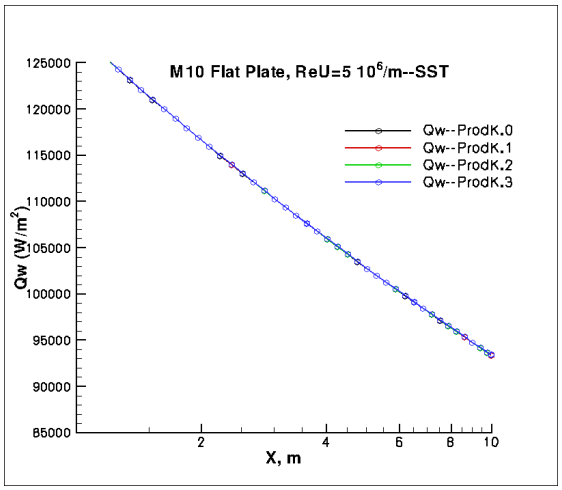

Figure 57. Mach 10 Flat Plate, SST model implementation, TKE Production Term Variants. Cold-Wall, $T_w/T_0 = 1/3$.

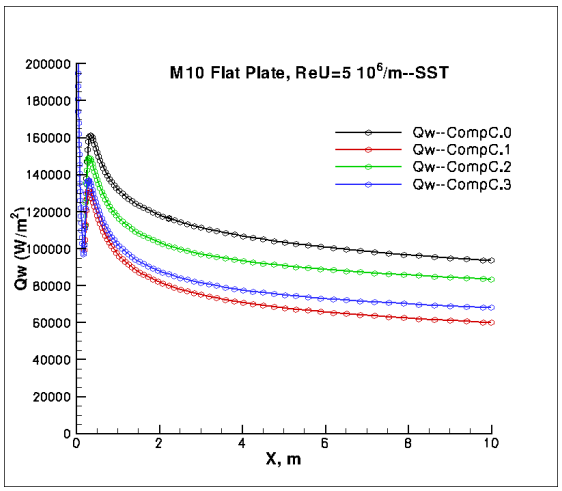

Figure 58. Mach 10 Flat Plate, SST model implementation, Free-shear Compressibility Corrections. Cold-Wall, $T_w/T_0 = 1/3$.

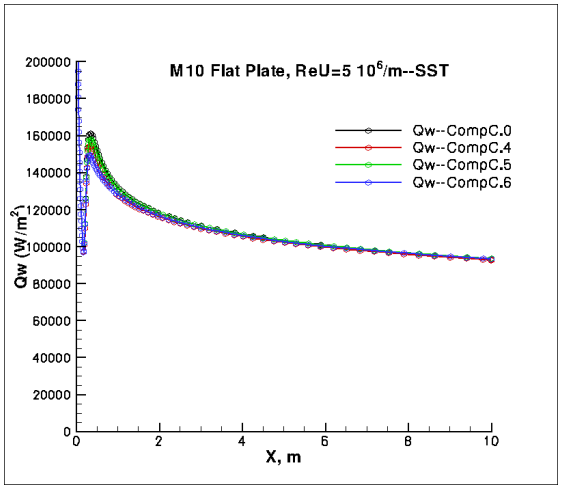

Figure 59. Mach 10 Flat Plate, SST model implementation study, Free-shear Compressibility Corrections, F_1-modified Sarkar, Zeeman, and Wilcox. Cold-Wall, $T_w/T_0 = 1/3$.

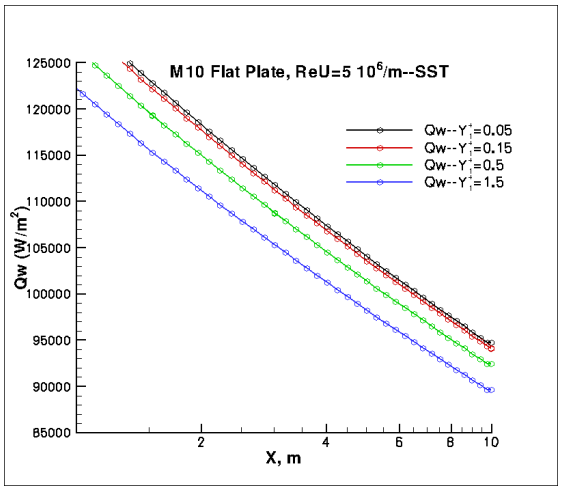

Figure 60. Mach 10 Flat Plate, Grid Sensitivity-SST model implementation study, Wall Boundary Condition WallBC0.1. Cold-Wall, $T_w/T_0 = 1/3$.

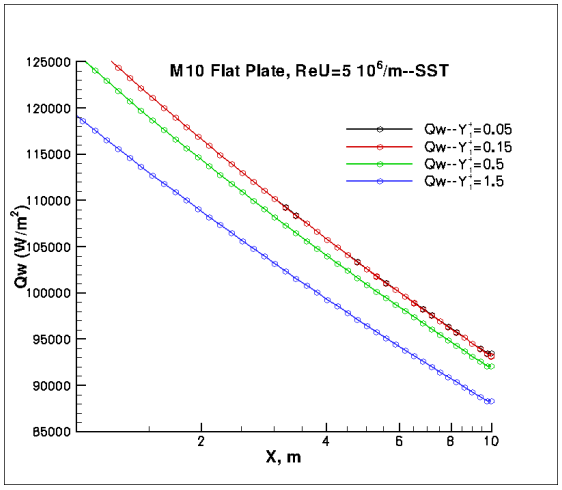

Figure 61. Mach 10 Flat Plate, Grid Sensitivity-SST model implementation study, Wall Boundary Condition WallBC1.1. Cold-Wall, $T_w/T_0 = 1/3$.

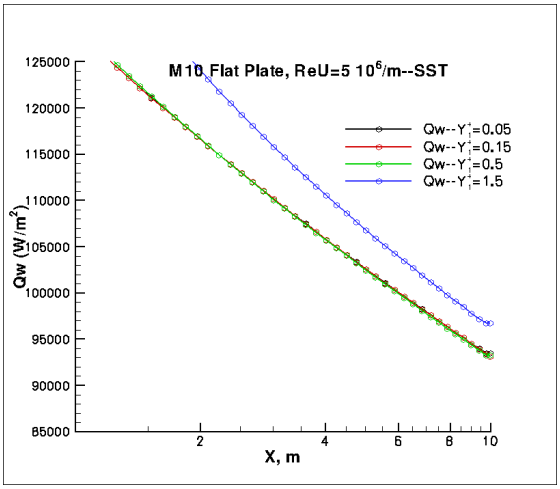

Figure 62. Mach 10 Flat Plate, Grid Sensitivity-SST model implementation study, Wall Boundary Condition WallBC1.6. Cold-Wall, $T_w/T_0 = 1/3$.

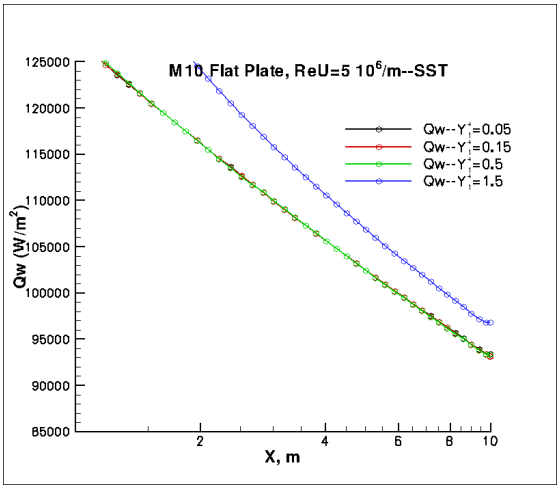

Figure 63. Mach 10 Flat Plate, Grid Sensitivity-SST model implementation study, Wall Boundary Condition WallBC1.10. Cold-Wall, $T_w/T_0 = 1/3$.

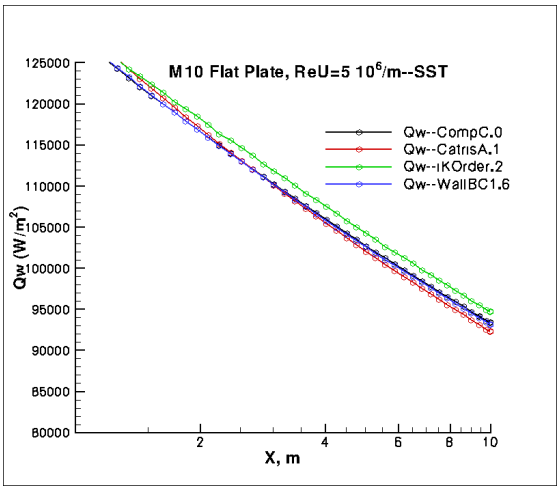

Figure 64. Mach 10 Flat Plate, SST model implementation study, Catris. Cold-Wall, $T_w/T_0 = 1/3$.